THE UNIVERSITY *of* EDINBURGH

Spatially distributed microelectrode arrays in smart contact lenses: novel sensing designs, theory and methods

THE UNIVERSITY *of* EDINBURGH

Matthew Donora
s1538909

A thesis submitted for the degree of Doctor of Philosophy

The University of Edinburgh

2019

Abstract

Smart contact lenses (SCLs) are a new class of wearable medical device set to revolutionise the way we approach healthcare. SCLs have been designed for functions such as active vision correction, drug delivery, display technology and chemical sensing. By integrating electrochemical sensors into SCLs, continuous, unobtrusive and non-invasive monitoring of chemical markers in the tear film may be carried out. However, despite significant advances in the past few years, an electrochemical smart contact lens (ESCL) suitable for clinical use has not yet been demonstrated. There are still design challenges which need to be addressed before this technology matures into real medical utility.

The primary issues facing ESCLs today are the construction of a safe, comfortable device, and the fidelity of the measurements made in the tear film when compared to an equivalent measurement in the blood. Recent advances in SCL platforms may be used to inform a new ESCL design, and address the issues of discomfort or safe use. A clinically approved SCL for glaucoma treatment is already used in hospitals around the world, offering hope of a clear path to an approved ESCL. However, the question of measurement fidelity may represent a greater challenge.

In this thesis, a next-generation ESCL is designed, built and characterised. The physical design follows previous work towards soft SCL platforms, and represents a significant improvement on the current ESCL state-of-the-art. To improve the quality of the measurements taken in this device, advanced electrochemical sensors are first investigated and developed on flexible substrates suitable for SCL integration. In the final design, a set of spatially distributed, individually addressable microelectrode arrays are integrated into a soft ESCL. A new electrochemical method is also developed to perform video-rate spatiotemporal electrochemical sensing, with very low power requirements and a minimum of driving logic complexity. In addition, a neural network method is developed to correct for the measurement distortion inherent to taking measurements in the tear film and attempting to make conclusions about the equivalent measurement in the blood. In combination, this new design and methodology greatly improves both safety and comfort of the ESCL, and makes progress towards an ESCL capable of taking measurements continuously and unobtrusively with real clinical utility.

Lay Summary

Smart contact lenses are a new type of device used in medicine and healthcare. Usually consisting of contact lenses with electronics embedded inside, they can perform functions such as active vision correction (like refocussing and zoom), delivering drugs into the eye, or measuring substances in the tears. This thesis focusses on electrochemical measurements in the tear film, which is a common way to measure the concentration of certain chemicals. Measuring in tears can be a less invasive, more comfortable way to get information about health or to monitor a disease than doing blood tests. It also means you can measure continuously, and without requiring the patient to go to a hospital. This can reduce the burden on patients and on healthcare professionals.

Although some smart contact lens prototypes have been made which can measure the concentration of chemicals such as glucose, they are not yet safe to use in the eye, and the measurements they make are not necessarily accurate enough to be useful to clinicians. The purpose of this thesis is to improve the design of the lens, the electrodes (i.e. the sensors themselves), and the way we make measurements, to be safer, more accurate, and to provide more information about what exactly is being measured.

In this thesis, recent advances in smart contact lens design are adapted and improved upon to make a safer, more comfortable lens. Multiple sensors, with improved sensing performance, are built into the lens, and a new technique is developed which can not only measure the concentrations at different places in the eye, but at video-speed as well. With this, it will be possible to see when new tear fluid has entered the eye, and what the concentration is in the new fluid. This gives much more information about the concentration in the rest of the body than simply measuring the entire tear fluid at once.

With these advances, safer, more accurate and more informative measurements can be made in the eye, leading to a smart contact lens with real use for healthcare professionals.

Acknowledgements

First, I would like to thank my supervisors, Prof. Ian Underwood and Prof. Baljean Dhillon, for the opportunity to work on this project, their support, and their enthusiasm for the work. I would particularly like to thank Ian for his trust and willingness to encourage me in whatever direction I decided to work on.

My thanks also to EPSRC and the CDT ISM for funding this project, without which it could not have taken place; and for financial support during two research placements abroad, without which the results would have been far less exciting. Thanks also to IMEC and to everyone at the CMST at Ghent University, for hosting me, sharing their expertise, and making me feel welcome during my placements. Particular thanks to Prof. Herbert de Smet for helping to arrange the collaboration, and Prof. Andrés Vásquez Quintero for lending me so much of his time, knowledge and experience.

Many people in Edinburgh deserve recognition for the help they have given during the last four years: the technical staff in the SMC, particularly Stuart Ramsey, Richard Blair and Dr. Andrew Bunting, for countless hours in the cleanroom (and lending bike tools); Dr. Eva Gonzalez-Fernandez and Dr. Ilka Schmüser for always taking the time to introduce me to the labs, how things get done, and how chemistry works and why it has to be like it is; and friends and colleagues in Ian's group, the CDT, the SMC and beyond, for (among other things) some incredibly long lunch breaks discussing the semantics of (usually) food; there are far too many to name here, but thank you all.

I would also like to thank my housemates through the years, three out of four landlords, two from a possible eight cats, everyone who came to visit, and of course my family, who deserve far more than a thesis dedication but will have to make do with it for now.

Table of Contents

List of Publications in Peer-Reviewed Journals

M. Donora, I. Underwood, 70-4: Late-News Paper: Electronic Contact Lens for Senses beyond Sight, SID Symp. Dig. Tech. Pap. 50 (2019) 996–999. doi:10.1002/sdtp.13094.

M. Donora, E. Gonzalez-Fernandez, A. Vásquez Quintero, H. De Smet, I. Underwood, Spatiotemporal electrochemistry on flexible microelectrode arrays: Progress towards smart contact lens integration, Sensors Actuators B Chem. 296 (2019) 126671. doi:10.1016/j.snb.2019.126671.

M. Donora, A.V. Quintero, H. De Smet, I. Underwood, Spatiotemporal Electrochemical Sensing in a Smart Contact Lens, Sensors Actuators B Chem. 303 (2019) 127203. doi:10.1016/j.snb.2019.127203.

List of Figures

Chapter 1

Chapter 2

Chapter 3

Chapter 4

Chapter 5

Chapter 6

Chapter 7

List of Tables

Chapter 1

Chapter 4

Chapter 5

Glossary

SCL – smart contact lens

ESCL – electrochemical smart contact lens

(R)GP – (rigid) gas permeable

NMR – nuclear magnetic resonance

FcMeOH – ferrocenemethanol

CGM – continuous glucose monitor

ISF – interstitial fluid

GOx – glucose oxidase

LOx – lactate oxidase

FDA – food and drug administration (USA)

LCD – liquid crystal display

LED – light emitting diode

AgNW – silver nanowire

PET - polyethylene terephthalate

TPU – thermoplastic polyurethane

ZIF – zero insertion force

W1 – working electrode 1

RT – room temperature

UV – ultraviolet

DI – deionised water

RIE – reactive ion etching

GPES – general purpose electrochemical system

LOD – limit of detection

IUPAC - international union of pure and applied chemistry

MARD – mean absolute relative difference

MAND – mean absolute normalised difference

CV – cross validation

ANOVA – analysis of variance

ISO - international organization for standardization

SNR – signal-to-noise ratio

1 Introduction

1.1 Wearable Devices and Non-Invasive Sensing

The way we approach healthcare is undergoing a fundamental shift, driven by a new class of medical technology. Non-invasive systems such as smart contact lenses (SCLs) are designed to continuously and unobtrusively gather medical data while the wearer goes about their day, in order to monitor their health status or help make diagnostic assessments [1–4]. This approach represents a move from hospital-based to distributed care, and has the potential to reduce the burden on hospitals and healthcare professionals, improve the quality of life of patients, and improve the quality and accuracy of the diagnostic conclusions we can make.

The ability to make continuous measurements without interrupting a patient's lifestyle has a number of significant advantages over individual tests, or even in comparison to continuous assessment in a hospital. When measuring the concentration of chemical biomarkers in the body, such as hormones or glucose, there is often a natural diurnal variation which is not accurately accounted for when individual 'snapshot' measurements are performed [5]. In fact, in many conditions the diagnosis rests on (or is aided by) tracking the time-series trend of an analyte, rather than the instantaneous concentration [6,7]. Diagnosing a disrupted cortisol response, for example, requires assessment of the elevation and return of the cortisol levels during the hours following an acute stressor [8]. Unobtrusive, multiple-sensor measurement can also improve the quality of the data. Many analytes which may be used to make medical assessments are affected by lifestyle and mood; therefore something which may be stressful or unusual, such as a trip to the hospital, may significantly reduce the utility of a hospital-based measurement [9].

As the technology required to unobtrusively monitor and analyse a suite of analytes matures, the focus of healthcare may begin to shift from treatment to prevention. Diagnoses or warnings of declining health may be made earlier, potentially autonomously. In many diseases or conditions, early diagnosis can reduce treatment time and improve patient outcome, particularly in degenerative conditions, while active management of a healthy lifestyle can help a person avoid ill-heath in the first place.

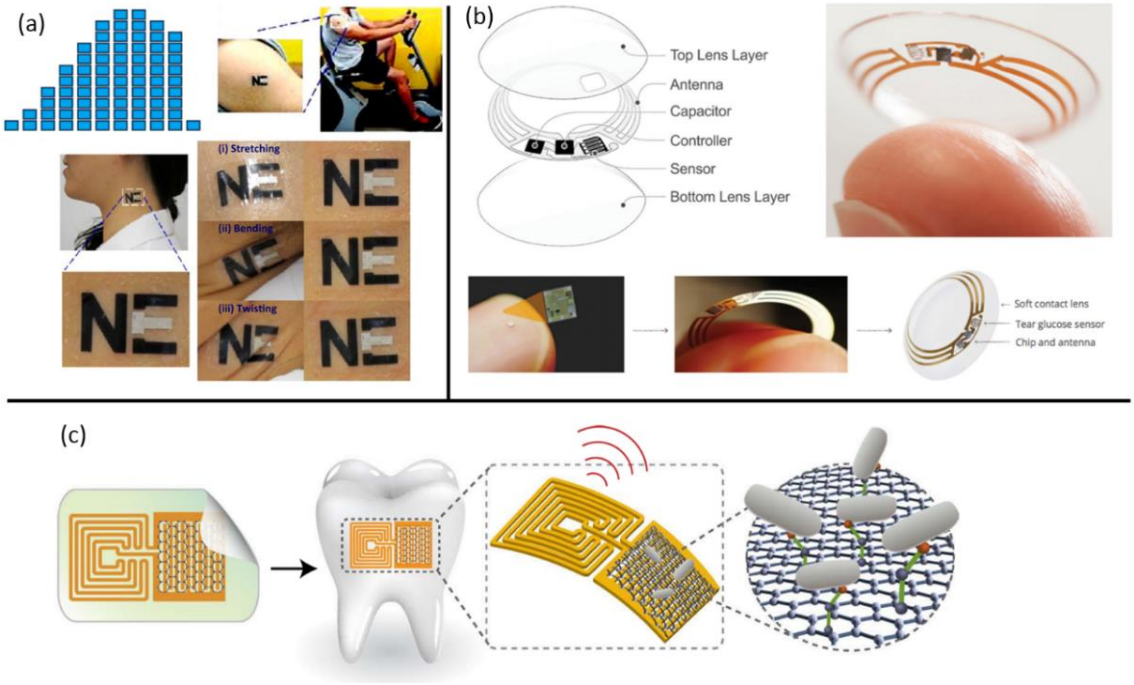

Figure 1.1: Non-invasive sensing devices. (a) Electronic tattoo for monitoring lactate in human perspiration. Adapted from [10]. (b) Smart contact lens designed for glucose monitoring in the tear film. Adapted from [11,12]*. (c) Device designed for bacteria detection on tooth enamel. Adapted from [13].*

A major class of non-invasive medical devices are those designed to continuously measure chemical biomarkers in one of several non-invasive media: usually sweat (Figure 1.1 a), tear fluid (Figure 1.1 b) or saliva (Figure 1.1 c) [4]. Chemical concentrations are most commonly measured electrochemically, although other methods (such as chromatography or colour-indicator devices) have been explored. The devices typically take the form of electronic ‘tattoos’ (sweat) [10,14], smart contact lenses (tear fluid) [2,3,15,16], and mouthguard or on-tooth sensors (saliva) [13,17]. While there is a degree of similarity among the function of these devices, each class of non-invasive media presents its own design challenges.

Of these media, tear fluid may offer the widest range of potential applications and benefits. Saliva, although a useful sensing medium, faces the challenge of unpredictable chemical interference from food and drink, as well as issues of patient compliance. And, while sweat-based sensing is similar in method to tear-based sensing, and skin-mounted electronics cause minimal discomfort, the skin is a highly effective barrier to chemical markers from the blood and the sweat does not provide a faithful representation of concentration in the blood in many cases; in general, sweat sensing is well-suited to specific cases such as sodium, lactate, ammonium

and calcium sensing [4]. Conversely, the tear film contains a suite of biomarkers which show good correlation to the concentration found in the blood (Section 1.1.5). Contact lenses can also be worn by most users with little or no discomfort, and are largely protected from damage within the eye, while saliva or on-skin ‘tattoo’ sensors may easily be damaged during normal use.

For these reasons, SCLs have been the subject of significant research in recent years, and represent a promising class of device for continuous, non-invasive sensing. Electrochemical smart contact lenses (ESCLs) have been developed alongside SCLs designed for active vision correction [18,19], intra-ocular pressure monitoring [20,21], visual or indicator displays, drug delivery [22], and more [23]. An additional benefit of the SCL platform is that multimodal devices may be created which incorporate a number of these functionalities into one device [15]. Finally, there exists an established contact lens industry, which provides two significant benefits: the physical parameters and fabrication of the supporting structure is already well characterised; and the idea of (and infrastructure catering to) wearing a contact lens is already normalised in the public consciousness.

1.2 Design Criteria of Smart Contact Lenses

A smart contact lens inherits the design parameters of a passive contact lens; that is, it must satisfactorily fulfil the safety and comfort requirements of a clinically approved lens before additional function is considered. There are two main types of contact lenses: rigid gas permeable (RGP, or gas permeable, GP), and soft lenses. Soft contact lenses are the most commonly used class of contact lens, and account for approximately 90% of wearers in the USA [24].

Soft contact lenses are usually made from hydrogel, with modern designs frequently incorporating silicone, while GP lenses are made from porous polymer, usually also incorporating silicone in order to improve flexibility and comfort [25]. They are typically around 14 mm in diameter, with a hemispherical inner (corneal) curvature of 8 - 10 mm [26]. Lens thickness usually varies from 60 - 240 µm, depending on the type of lens and correction power [27], although thicker contact lenses do exist [26].

Table 1.1: Design criteria of a smart contact lens

Design Criteria	**Specification**	**Ref**
Thickness	*60-240 µm (ideal); <600 µm (upper range)*	[26,27]
Diameter	*14 mm*	[26]
Radius of curvature	*8-10 mm*	[26]
Transparency	*Central 8 mm ⌀*	[112]
Flexibility	-	
O_2 permeability	*Daily: 24.1 x 10^{-9} cm s^{-1} [mm Hg]$^{-1}$* *Extended wear:* *34.3 x 10^{-9} cm s^{-1} [mm Hg]$^{-1}$*	[113]
Power consumption	*Approx. 100 µW*	[23]
Data transfer	*Low bitrate*	[3]
Biocompatibility	*Biocompatible materials or safe encapsulation*	[82]
Waterproofing	*Electronic components protected from ingress of water*	-
Robustness	*Must be functional after repeated 180° folds*	[16,19]

When adding functionality to a contact lens, additional design constraints must be followed. The mechanical properties of the contact lens platform must be matched as closely as possible by all integrated components; therefore flexible substrates must be used during fabrication. Ideally all materials, but at least any non-encapsulated materials, should be biocompatible to prevent a foreign body response and protect the eye from damage.

If on-board circuitry is required, this must ideally remain within the thickness constraint above, although a lens of central thickness 600 µm has been used with no reported irritation [28]. In most prototypes a thinned silicon chip has been incorporated, which can be reduced to a thickness of some tens of microns [29]. Thinned silicon is somewhat flexible, but with an elastic modulus of greater than 160 GPa in the <110> crystalline direction [30] it is much stiffer than the materials used in soft smart contact lenses (e.g. polyimide, with an elastic modulus of 2.5 GPa [31]); hence, to avoid irritation or damage in the eye, the footprint of this chip must remain small (approx. 1 mm^2).

The pupillary region (a central portion of the lens of maximum diameter 8 – 9 mm) must be (predominantly) transparent to avoid impeding the wearer's vision. Oxygen permeability is also crucial for ensuring sufficient oxygenation of the eye. Modern contact lens materials are highly oxygen permeable [32], but most flexible, transparent substrates used in sensor fabrication or flexible electronics in general are not. If the lens is to be worn for extended periods, oxygen flow must be ensured, either by reducing the total area utilised by non-oxygen-permeable materials, or by developing new substrates which allow oxygen transmission.

In addition to user comfort and safety, there are some environmental factors which must be considered to ensure reliable function of the device. The eye is an aqueous environment, and the system within the lens must be protected from ingress of water by suitable encapsulation. It must be robust to repeated mechanical deformation, in particular folding of the lens, as this is a common mode of use when inserting or removing a contact lens. Most SCL prototypes aim to function wirelessly, and since battery technology is not quite yet advanced sufficiently to produce a safe, flexible battery of sufficient capacity for extended use (although advances in this field have recently been reported [33]), other power sources are usually utilised. Supercapacitors and fuel cells have been suggested [34], but currently the most promising method is to use an antenna in the SCL to harvest power inductively from a radio frequency source (delivered from an eye-patch or glasses frames) [3]. A benefit of this method is that an antenna can also be used for data transfer, which, due to the extremely limited storage space in a SCL, is necessary for harvesting continuous data. Due to limits placed on the safe level of RF radiation into the eye, power transfer is limited [35]; power transfer on the order of 100 μW has been demonstrated [23], and the entire system must function on this power allowance. Data transfer is also limited, and therefore in designing the system as a whole it is important to be discerning about the quantity of data both produced and harvested.

1.3 Measurement of Chemical Markers

A common method of chemical sensing in point-of-care devices is electrochemical sensing [36]. There are a number of benefits to this technique over other methods such as NMR, mass spectrometry, and chromatographic or electrophoretic separation. First, the infrastructure is easily miniaturised by microfabrication methods. The system can be solid-state, and in many cases requires no prior preparation of the analyte medium. It requires only basic signal processing (usually

amplification and a linear operation to produce concentration values from measured current), and can operate on a low-power basis (drawing approx. 10^{-8} W, or less if required [16]). Chemical or biochemical functionalisation methods can make the sensors selective for a large variety of different chemical species [37]. Finally, the methodology is well characterised, and, particularly as a result of developments in glucose monitoring technology, significant effort has already been directed towards optimised production of small, point-of-care electrochemical systems which require no expertise for use [38].

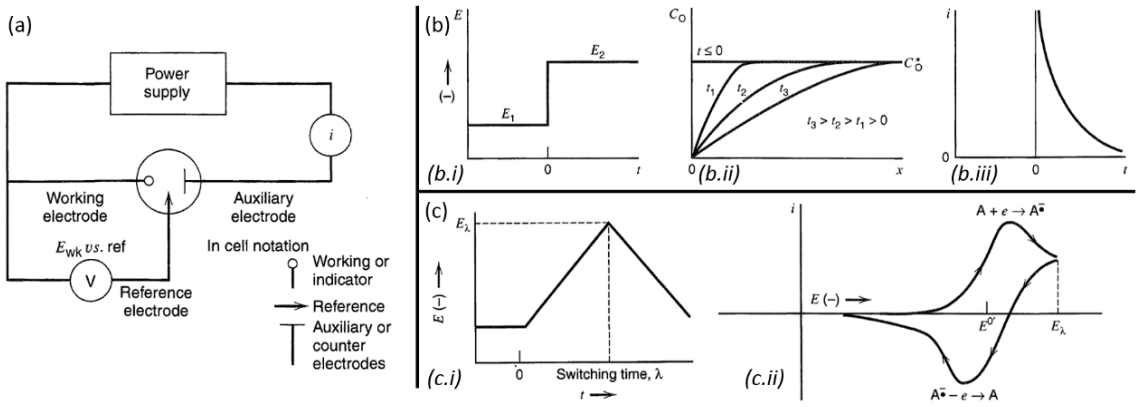

Figure 1.2: Electrochemical methods. (a) Schematic circuit of a three-electrode system, often used to carry out chronoamperometry and cyclic voltammetry. (b) Overview of the chronoamperometric method: (b.i) waveform of voltage step experiment in which species is electroinactive at E1, but reduced at E2; (b.ii) concentration profiles for various times during the experiement; (b.iii) Current flow versus time. (c) Overview of the cyclic voltammetric method: (c.i) cyclic potential sweep; (c.ii) current flow versus time, also known as a cyclic voltammogram. Figures sourced from [39].

Various electrochemical methods exist. Most utilise a three-electrode system, with a working electrode (which may be functionalised for selectivity of a particular analyte), a counter electrode (which supplies current) and a reference electrode (against which the voltage may be measured) (Figure 1.2 a) [39]. Common methods include chronoamperometry (Figure 1.2 b), in which voltage is stepped from one value to another and the current is measured against time, and cyclic voltammetry (Figure 1.2 c), in which the voltage is swept between two limits while current is measured against voltage.

Electrochemical sensing makes use of the fact that redox (reduction/oxidation) reactions occur spontaneously at a well-defined potential. Thus, by sweeping the voltage (such as in cyclic voltammetry) and measuring the current flowing between

the counter and working electrode, features of the current in the forward and backwards sweeps will correspond to the oxidation and reduction of target species in the medium. The magnitude of this current contains information about the concentration of the species within the medium.

Some target analytes, such as ferrocenemethanol (FcMeOH), naturally undergo a redox reaction at a bare gold or platinum electrode at well-characterized potentials. These are frequently used as 'redox reporters', for characterisation and testing of electrochemical systems [40–42]. Other target analytes require intermediate chemical reactions to interface with the working electrode, usually functionalizing the electrode surface to select for a specific chemical, though immobilization of active chemical modifiers in hydrogel or solution is also used [37]. For example, electrochemical sensing of glucose uses the glucose oxidase (GOx) enzyme, usually immobilised on the working electrode surface using thiol groups [43], which turns over glucose in the presence of oxygen to form hydrogen peroxide [38]. Hydrogen peroxide then oxidises at the working electrode under an anodic current, and the current resulting from this oxidation is measured by the electrochemical system:

$$\textit{glucose} + O_2 \xrightarrow{GO_x} \textit{gluconic acid} + H_2O_2 \tag{1.1}$$

$$H_2O_2 \rightarrow O_2 + 2H^+ + 2e^- . \tag{1.2}$$

The physical design of the working electrode has a significant effect on the sensing properties of the electrochemical system [44–47]. Working electrodes with at least one relevant dimension of less than 100 µm are generally classed as microelectrodes, while those with a relevant dimension less than 100 nm are classed as nanoelectrodes. Micro- and nanoelectrodes have enhanced sensing properties when compared to macroelectrodes, because at smaller length scales a radial diffusion field is formed around the microelectrode, while a predominantly linear diffusion field is formed around a planar macroelectrode (Figure 1.3) [47]. Radial diffusion is more spatially efficient in terms of current density and analyte flux, and, since noise scales with electrode area, leads to an improved limit of detection and higher signal to noise ratio.

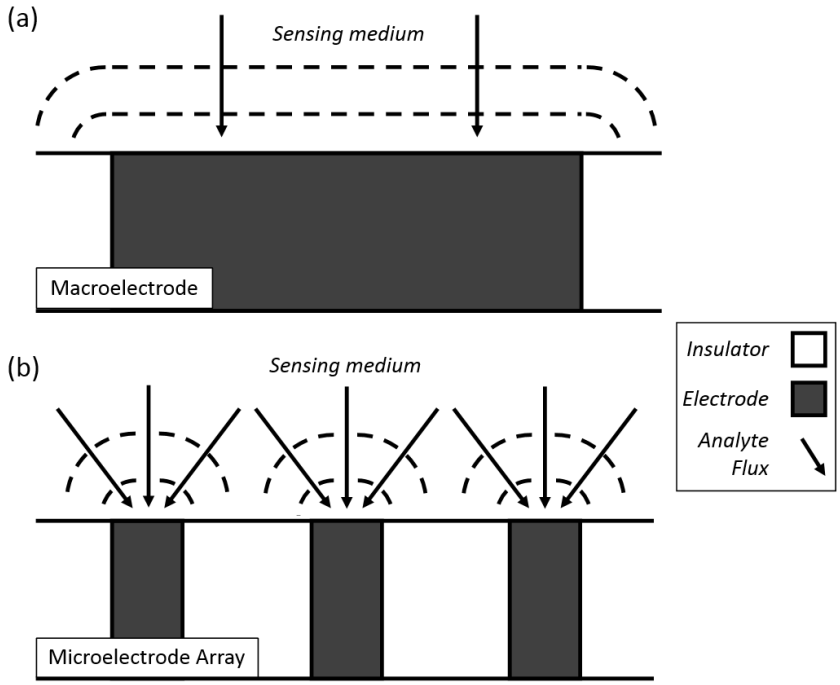

Figure 1.3: Diffusion characteristics of macro- and microelectrodes. (a) Predominantly linear diffusion field formed during operation of a macroelectrode. (b) Predominantly radial diffusion field formed during operation of a microelectrode array.

After a certain time, growth of the individual radial diffusion fields supplying each microelectrode in a microelectrode array will lead to overlap, and a predominantly linear diffusion field is formed form the combination of the sub-fields. After this time, the microelectrode array acts akin to a macroelectrode of equivalent areal size, and the advantageous sensing properties of microelectrodes are lost.

During electrochemical measurements a double layer capacitance is charged at the electrode surface [39,48]. This capacitance is proportional to electrode area, and hence charges faster for smaller electrodes. Thus, the speed at which measurements may be taken is also improved in micro and nanoelectrodes.

Miniaturisation of the working electrode reduces the magnitude of current drawn during measurement, which reduces power requirements of the system [49]. If the current is too low, specialised potentiostats or amplifiers may be needed to process the signal, but the advantageous sensing properties of miniaturised electrodes may be preserved while drawing a higher current by using multiple connected micro- or nanoelectrodes and operating them in summation [16,47]. These are often termed micro- or nanoelectrode arrays [50], and are distinct from arrays of individually addressable electrodes [49] (which are sometimes also called arrays).

1.4 Eyes and the Tear Film

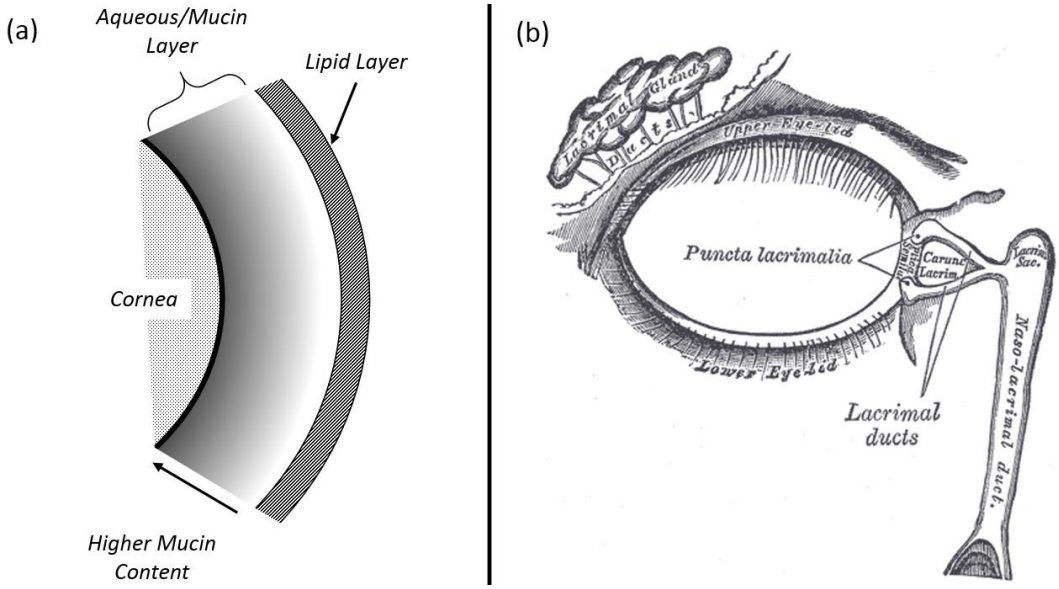

Figure 1.4: The tear film and lachrymal system. (a) Schematic representation of the bilayer model of the tear film. (b) Illustration of the anatomy of the lachrymal system surrounding the eye. Reproduced from Gray's Anatomy, Plate 896.

The tear film is a complex fluid environment. Current estimations of the thickness of the tear film range from 3 – 11 µm, and the leading model suggests a bi-layer structure, with a thin superficial lipid layer and an aqueous/mucin gel layer with decreasing mucin content from the corneal surface to the lipid layer (Figure 1.4 a) [51]. Lachrymal fluid enters the eye from the lachrymal gland at the upper lateral region, and flows across the cornea to the superior and inferior lachrymal puncta, through which it drains into the lachrymal sac and subsequently into the naso-lachrymal duct (Figure 1.4 b). While the flow of lachrymal fluid has been studied, the flow of the tear film over or underneath a contact lens is not as well characterised [51–54].

There is also a difference in chemical composition between ‘basal’ tears (with which the cornea is kept continually wet and nourished), ‘emotional’ tears (triggered by strong emotional responses), and ‘reflex’ tears (stimulated by irritation to the eye) [55,56]. Reflex tears generally contain different quantities of the chemical analytes found in the blood when compared to the other two categories. It is therefore crucial that an ESCL does not irritate the eye when performing measurement. Other methods of harvesting tear fluid for analysis [57] often require skilled application to avoid irritation of the eye, and this may be one reason why older investigations

found less of a correlation between analytes in the tear film and blood than more recent studies [58–60].

Performing electrochemical measurements in the eye is therefore not as simple as placing a single electrode in an ESCL and assuming a direct or lag/bias relationship between the measurements performed there and the concentration in the blood [7]. In fact, there is a series of effects which combine to create a complex measurement distortion, and this must be corrected for if we are to make accurate diagnostic conclusions from electrochemical measurements performed there. In addition, due to variations in physiology all of these effects are patient-specific (i.e. each patient will exhibit a unique measurement distortion). These effects are:

1. The metabolic pathway of the analyte from the blood plasma to the lachrymal fluid;
2. Filtration into the eye via the lachrymal gland at various rates depending on eye stimulation, hydration etc;
3. Mixing of fresh tear fluid with existing fluid in the tear film and lachrymal lake (an indeterminately mixed bulk of tear fluid situated at the lower eyelid);
4. Increased concentration of analyte due to evaporation, and;
5. Egress of analyte through the lachrymal puncta, crying, or other pathways.

In order to correct for the overall measurement distortion in electrochemical measurements performed in the tear film (or other non-invasive media), a multimodal approach is necessary. Design of an ESCL which provides data on the introduction, progress, mixing and drainage of tear fluid in the eye would provide more information about the nature of the sensing medium in which measurements are taking place [16,49]. With this information, more accurate conclusions about the concentration levels in the in-flowing lachrymal fluid may be made, which would both increase measurement accuracy and reduce the time delay in sensing concentration changes in the blood. A patient-specific method to perform a mathematical correction for the distortion between concentration in the lachrymal fluid and the blood would address the remaining source of measurement distortion, and account for the individuality of each patient’s physiology.

1.5 Analytes

A number of different analytes have been proposed as good candidates for non-invasive sensing in the tear film [11,61]. The most frequently suggested application

is glucose monitoring, due to the established industry around diabetes management [15,58,62]. There are already numerous methods for glucose monitoring, with point-of-care devices such as handheld fingerprick sensors and minimally-invasive continuous glucose monitors (CGMs), which monitor glucose in the interstitial fluid (ISF), being the most common [38]. Both of these methods require puncturing the skin, either to draw blood (in the fingerprick method) or to provide constant access to the ISF (for transdermal or subcutaneous CGMs). Monitoring glucose in the tear film with an ESCL would most likely represent an improvement in patient comfort when compared to these methods. However, the nature of diabetes management, in which an early-warning system is often essential, calls into question the suitability of SCL-based diabetes monitoring; there is a significant time delay between blood glucose concentration and its representation in the tear film [58]. CGM methods already provide many of the benefits which would be derived from an ESCL, and the drawbacks (the time delay) potentially outweigh the additional improvements (the improved comfort of a non-invasive device). It is currently unclear whether measurement distortion correction methods would be able to sufficiently reduce this delay in order to use an ESCL for diabetes management (Chapter 5). However, many other analytes exist with potential diagnostic utility; Table 1.2 details some of these analytes and their diagnostic application.

Lactate is a metabolite found in the tear film which may be used as a marker of ischemia, sepsis, liver disease and cancer [2]. It is frequently measured in diagnostic scenarios, and also in assessing athletic performance, but there is currently no satisfactory way to monitor it continuously. Lactate may therefore be a promising candidate for ESCL-based measurement. Like glucose, a functionalisation method for selectivity of the L-lactate molecule is well described, based on the action of the lactate oxidase (LOx) enzyme.

Table 1.2: Biomarkers found in the tear film and their diagnostic applications. Some parts adapted from [11].

Analyte	**Diagnostic Application**	**Ref**
Glucose	*Diabetes management*	[114]
Lactate	*Ischemia, sepsis, liver disease and cancer*	[2]
Na^+	*Hyper/hyponatremia*	[115]
K^+	*Hyper/hypokalemia and ocular disease*	[116]
Ca^{2+}	*Hyper/hypocalcemia*	[117]
Mg^{2+}	*Hyper/hypomagnesemia*	[118]
Cl^-	*Hyper/hypochloremia*	[119]
Urea	*Renal function*	[120]
Pyruvate	*Genetic disorders of mitochondrial energy metabolism*	[121]
Ascorbate	*Diabetes*	[122,123]
Total Protein	*Dry eye conditions, ocular insult and inflammation*	[124,125]
Alcohol	*Intoxication*	[126]
Vitamins (B2, C, B6)	*Nutrition*	[126]
Dopamine	*Glaucoma*	[72]
Cortisol	*Stress-related illnesses, Cushing's disease, Addison's disease*	[9,67]
Serotonin	*Alcoholism, mood and sleep disorders*	[67]
Cytokines	*Stress, depression*	[67]
Secretory Immunoglobulin A	*Stress*	[67]
Dehydroepiandrosterone	*Stress*	[67]

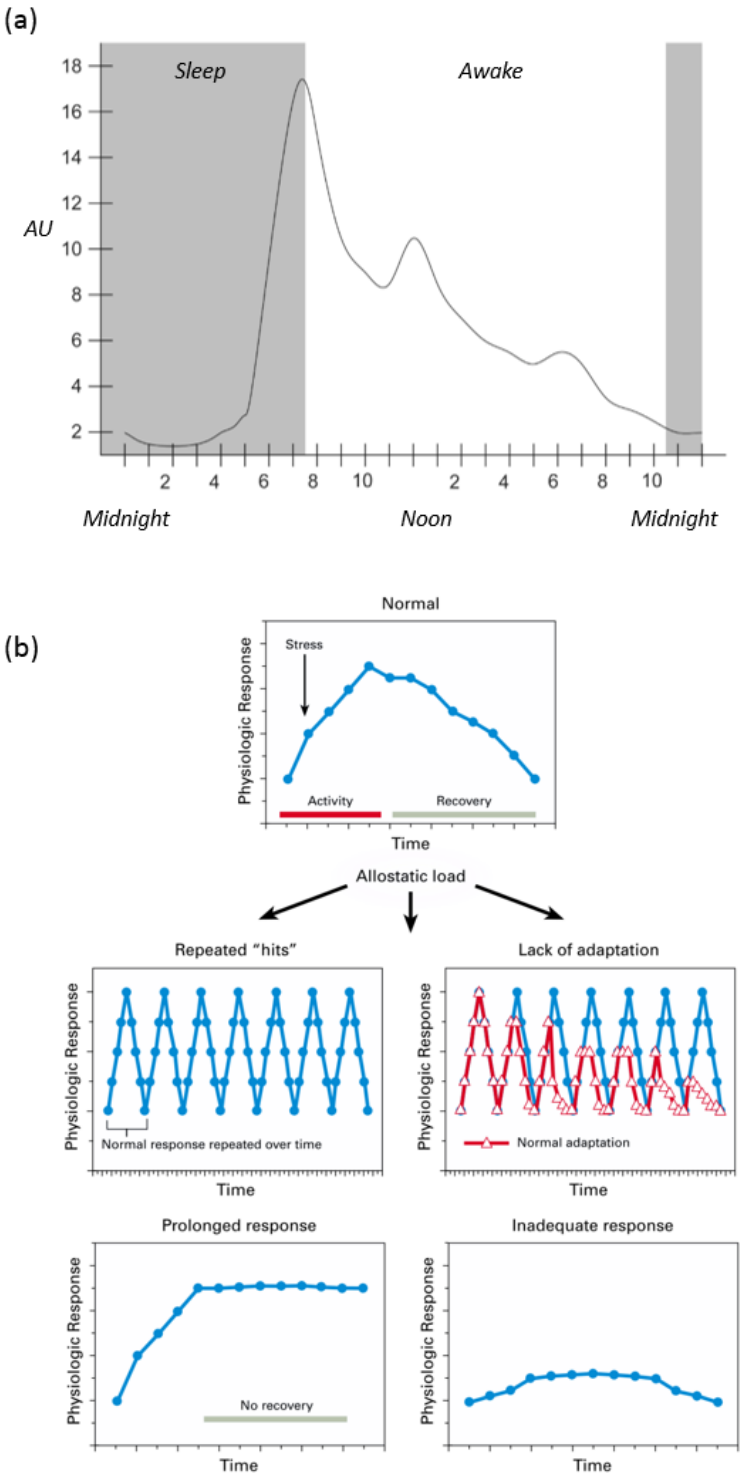

Figure 1.5: Cortisol variation throughout the day and after an acute stressor. (a) 24 hour plasma cortisol secretion curve in humans. Adapted from [5]. (b) The effect of repeated stressors on cortisol response. Physiological adaptation to repeated stressors (chronic stress) can lead to disrupted cortisol profiles such as a prolonged or inadequate response. Adapted from [8].

Other markers which may be of relevance in ESCL sensing include urea, which is an indicator in kidney health [63], metal ions such as Na^+, K^+, Ca^{2+}, Mg^{2+}, Cl^- and HCO_3^- for elevated or reduced levels outwith healthy ranges [11] and more. Electrochemical methods have also been developed to measure hormones such as cortisol, dopamine and serotonin [64–66], and studies have found good representation of blood levels in the tear film [67]. Continuous, unobtrusive sensing is of particular importance in assessing underlying physiological processes, such as the response of the endocrine system, in conditions which have a psychological element. For example, a disrupted cortisol response to an acute stressor (Figure 1.5) is a diagnostic indicator in conditions such as depression [68,69], chronic stress [8,9], addiction [5], PTSD [70] and more, and there is currently no satisfactory way to monitor cortisol continuously and unobtrusively, such that the measurement itself does not influence the result. Non-invasive technology such as ESCLs may provide valuable new insights into conditions in which we better understand the psychological effects than the physiological, and would be a vast improvement on the current practice (a twice-daily saliva swab) [16]. In addition, hormones can act as biomarkers for various ocular conditions, such as serotonin and dry-eye [71] or dopamine and glaucoma [72].

The tear film also contains a wide range of proteins, electrolytes and lipids, and the diagnostic potential of many of these is yet unexplored [73,74]. Additionally, ESCLs could be used to monitor drug or alcohol levels in the body, or to help quantify uptake of drugs delivered via the eye.

1.6 Outline of the Thesis

1.6.1 Key Objectives and Expected Outcomes

The aim of this PhD is to develop a next generation ESCL device, incorporating the following improvements on the current state-of-the-art:

1. Improved sensors: advanced micro- and nanoelectrodes will be fabricated on SCL-compatible substrates, and their physical and electrochemical properties characterised. Multiple individually-addressable microelectrode arrays will be integrated into a SCL, making use of the enhanced sensing characteristics of microelectrodes, and gathering more information about the flow of analytes across the eye than any current design.

2. Improved platform: the microelectrode system will be integrated into the polyimide/TPU platform developed at Ghent University, building upon established work and providing a route to clinical use. A new ESCL, incorporating microelectrode array technology, will be designed, fabricated and characterised.
3. Improved data processing: with a clearer understanding of the challenges faced in gathering meaningful electrochemical data in the eye, the physical design will be combined with new data processing methods to address the issue of measurement distortion in ESCLs and non-invasive devices in general.

1.6.2 Thesis Overview

Chapter 1: Introduction

An introduction, including an overview of research scope and context, key methods within the field of electrochemistry, relevant information on ocular and diagnostic physiology, and material and physical design of (smart) contact lenses.

Chapter 2: State of the Art

An overview of the state of the art in SCLs, ESCLs and other relevant technologies.

Chapter 3: Spatiotemporal Sensing on a Flexible Microelectrode Array

A study into integration of microelectrode arrays onto flexible polyimide substrates is made. Eight individually addressable microelectrodes, with an integrated counter electrode, are fabricated on polyimide. The flexible microdisc electrodes are characterised physically and electrochemically. A new spatiotemporal electrochemical method is introduced.

Chapter 4: Flexible Through-Flow Ultramicro and Nanoband Electrodes

A study into a new laser-based fabrication method for ultramicro and nanoband electrodes on flexible polyimide substrates is made. Electrode morphology and performance are characterised, and use cases are explored, including robustness of the device under extreme mechanical deformation and damage, and active electrochemical sensing of through-flowing liquids.

Chapter 5: Interpreting Measurements Made in the Tear Film

The issue of measurement fidelity in non-invasive sensing, and in particular in ESCLs, is formulated and placed in the wider context of medical diagnostics and measurement. A novel approach for measurement correction using neural networks is described, and a preliminary demonstration is made using two types of data. The neural network technique is compared quantitatively to the lag/bias correction method widely used in glucose sensing.

Chapter 6: Spatiotemporal Electrochemical Sensing in a Smart Contact Lens

An ESCL prototype comprising four individually addressable microelectrode array islands, and an integrated counter electrode, is designed, fabricated, and characterised, both physically and electrochemically. Various new design and fabrication solutions are presented. An updated version of the spatiotemporal electrochemical sensing technique is described, and the system is tested in various representative environments, including a model eye, generating a time- and space-varying concentration map across the surface of the model eye.

Chapter 7: Summary and Conclusions

The work is summarised, and achievements are placed in the context of the research field. Conclusions are made and future work is proposed, including further integration work to prepare a device for clinical trials, design improvements to the ESCL prototype, and functionalisation work to address specific biomarkers in an ocular environment.

2 State of the Art

2.1 Smart Contact Lenses in Research and Clinical Use

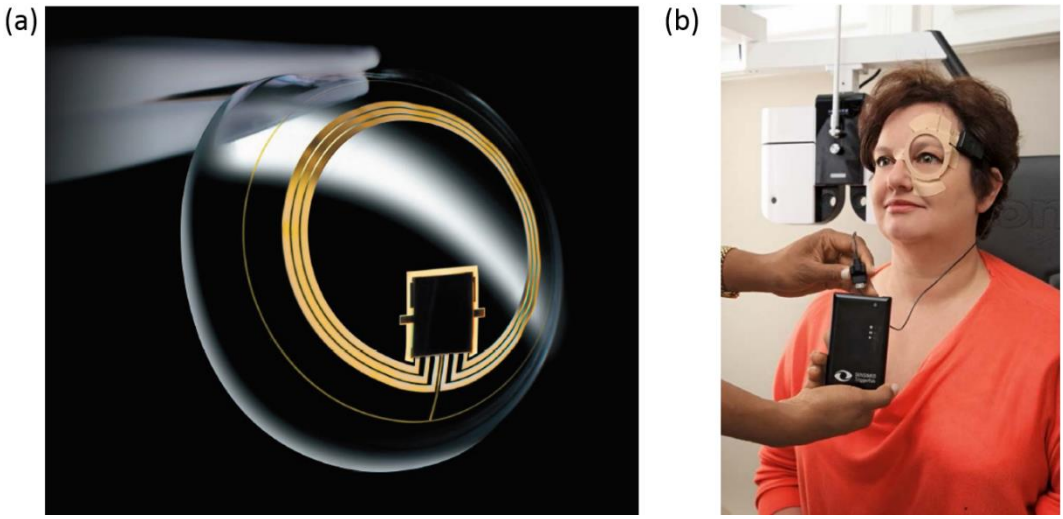

Figure 2.1: The Sensimed Triggerfish, a SCL in clinical use. (a) The Triggerfish lens. (b) The Triggerfish in use, with the eyepatch and power/data storage unit shown. Adapted from [75,76].

Smart contact lens concepts and prototypes have been found in a range of different research fields, in the media, and in clinical use. An FDA approved SCL designed for glaucoma treatment is currently used by clinicians (Figure 2.1 a) [21,75,76]. This device uses a strain gauge to monitor intra-ocular pressure, and contains a thinned silicon chip and a gold antenna to harvest power inductively from a patch worn around the eye (Figure 2.1 b).

In their representation by the media, many contact lens prototypes appear centred around augmented reality, virtual reality, and embedded camera technology. However, the research field does not reflect this distribution. Significant work has been focussed on integration of liquid crystal displays (LCDs) into contact lenses [18,19], usually for active vision correction such as electronic focussing or magnification, or to create an artificial iris. Single element LED indicators have also been integrated into SCLs, with the potential to warn the user or others in the case of (e.g.) a hypo- or hyperglycemic event [23]. Other SCL designs with drug delivery technology have been proposed [22].

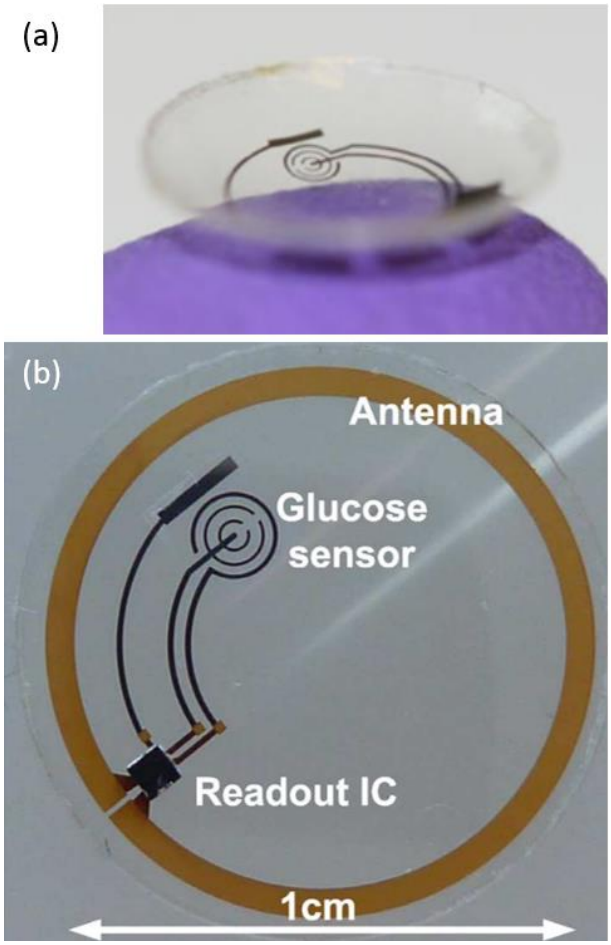

Figure 2.2: The first published wireless ESCL prototype. (a) Side view, adapted from [1]. (b) Top view, adapted from [62].

Electrochemical sensing in SCLs has been reported in a number of different studies. The first ESCL prototypes were developed at the University of Washington (Figure 2.2), culminating around 2012 in a series of wireless devices functionalised to measure glucose or lactate [2,3]. Platinum electrode sites were defined on a polyethylene terephthalate (PET) substrate, and then cut and moulded in a hemispherical lens shape. A silicon chip integrated into the SCL platform carried out power harvesting, electrochemical measurement, signal processing and data transfer. The concentration measured was encoded into a frequency shift in the reflected signal from the antenna.

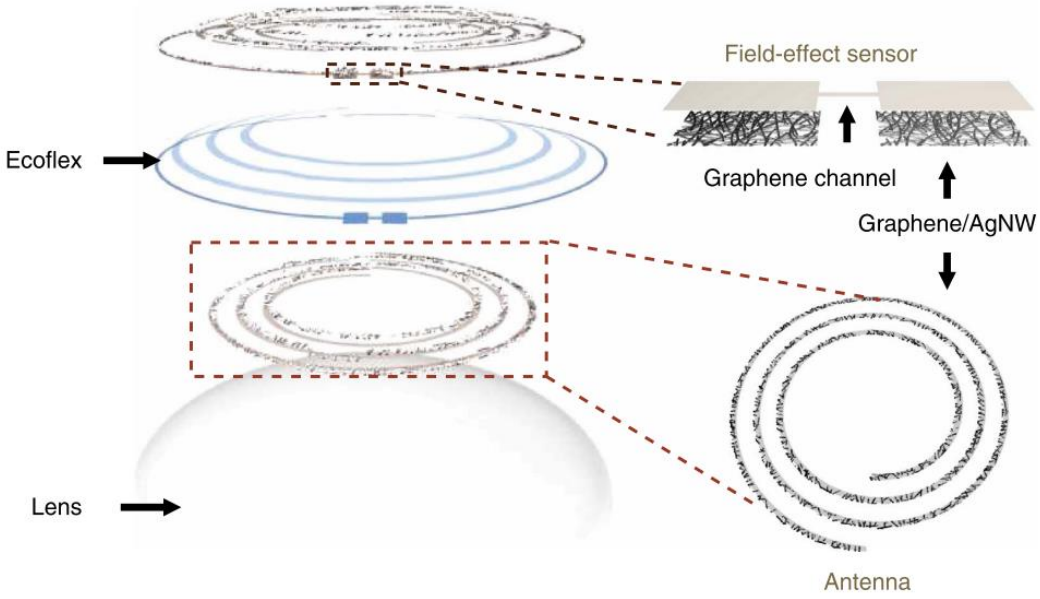

Figure 2.3: Schematic representation of a more recent ESCL design representing a departure from traditional metal deposition fabrication methods. Adapted from [77].

Since then, studies have explored other methods of fabricating glucose sensors in a SCL; for example, a graphene/AgNW (silver nanowire) hybrid was used to create transparent, stretchable components, and functionalised a section with GOx for glucose sensing (Figure 2.3) [77]. A similar functionalisation method was also used to create a graphene-based glucose sensor in a soft contact lens [15]. Both of these advances succeeded in developing unconventional fabrication methods which led to transparent and stretchable structures, although they did not necessarily aim to improve the quality of the electrochemical measurement itself.

2.2 Fabrication Methods and Material Design

At the intersection of the design constraints discussed in Section 1.1.2, and the fabrication processes necessary to create electrochemical sensors, there is a relatively narrow choice of well-studied substrates for SCL platform design. Many prototypes used a PET substrate [3], due to its biocompatibility, transparency, resistance to many of the chemicals used in cleanroom processing [78], and low glass transition temperature of around 60 - 65 °C [79], which allowed thermoforming after fabrication. However, PET substrates exhibit buckling behaviour after thermoforming [80], and are not sufficiently oxygen permeable to ensure safe extended use (with diffusivity on the order of 10^{-19} m^2 s^{-1} [81]). Their low glass transition temperature also leads to issues in higher temperature cleanroom

processes. Silicone or other elastomers and polymers [15,77] have been used to aid fabrication, though these reports do not always define a clear path to integration into a hydrogel-based soft contact lens.

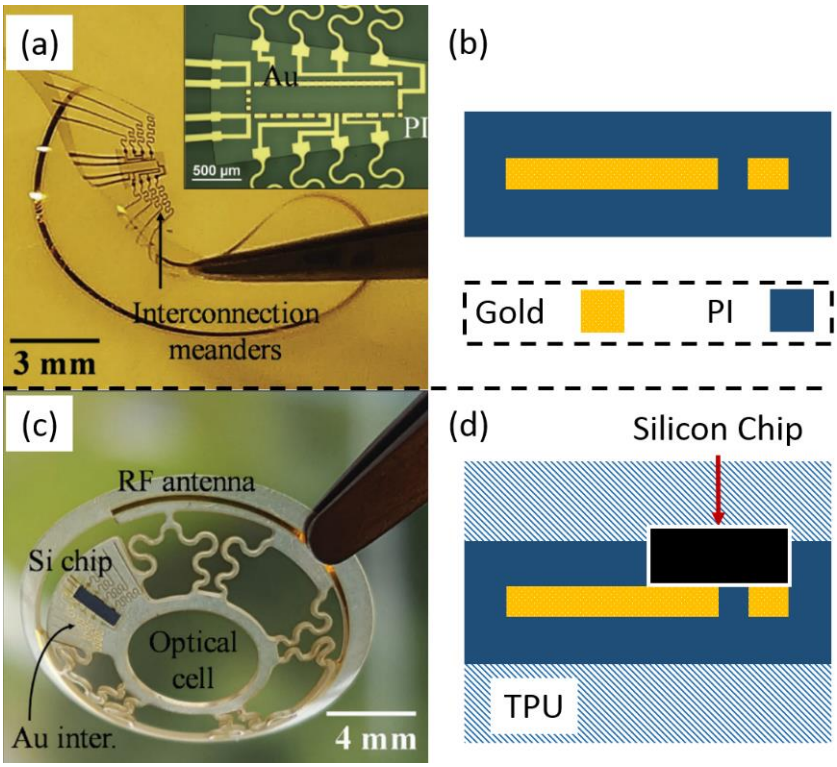

Figure 2.4: The SCL platform developed by Vásquez Quintero et al. at Ghent University [19]*. (a) Core polyimide device, before chip integration and encapsulation into thermoplastic polyurethane (TPU); (b) schematic cross section of the core polyimide platform. (c) Soft SCL platform, ready for integration into hydrogel lens; (d) schematic cross section of the soft SCL platform. Adapted from* [82].

A state-of-the-art SCL platform has been developed by Vásquez Quintero *et al*. at Ghent University for integration of LCDs, based on polyimide and thermoplastic polyurethane (TPU) (Figure 2.4) [19]. Polyimide is a biocompatible polymer [83,84] which is well-suited to cleanroom fabrication due to its resistance to chemicals, liquid-state processing, resistance to many chemicals used in cleanroom processing [78], and (after curing) its high glass transition temperature of 360 °C [85]. Layers of a few microns in thickness can be created, which leads to excellent flexibility. Due to these favourable properties, polyimide has been increasingly used in research towards flexible electronics intended for biomedical use [49,82,86–88]. The core of the platform creates metallization layers deposited between two layers of polyimide. This places the thin-film circuitry in the neutral mechanical plane of the device,

which protects it from stress during mechanical deformation. Integration into this platform of a thinned silicon chip (30 µm thickness, approx. 0.2 mm^2) has been demonstrated (Figure 2.4 c).

The core of the device is encapsulated in TPU, which can then be thermoformed into a hemispherical cap shape. TPU is also a biocompatible polymer [89], and can be moulded at temperatures below 150 °C [19]. A laser is used to define the physical structure of both the core device and the TPU encapsulation, ensuring the minimum footprint of non-oxygen-transmissible structures within the lens. The final device can be integrated into a hydrogel to create a soft SCL.

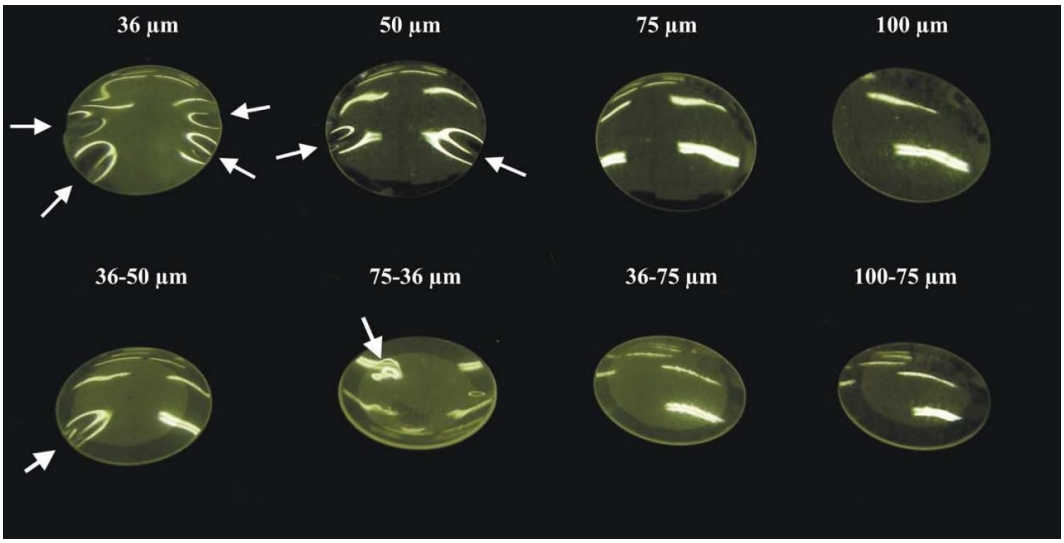

Figure 2.5: Wrinkling and buckling behaviour of PET substrates after thermoforming into a spherical cap shape. Reproduced from [80].

A recurring issue when integrating electronics into a contact lens platform has been buckling behaviour observed in the substrate after thermoforming [80]. SCL prototypes fabricated on PET and moulded to a hemispherical cap shape exhibit buckling (Figure 2.5) which could lead to discomfort and irritation in the eye, and accumulation of proteins and biofouling. The polyimide/TPU-based platform developed by Vásquez Quintero *et al*. [19] eliminates buckling behaviour by careful design of the polyimide/TPU regions (Figure 2.4 c); the polyimide regions are not stretchable, such that the metallization is protected within the neutral mechanical plane of the layer stack, while the TPU encapsulation is both stretchable and mouldable. Use of meanders in the radial direction and thin straight wires in the circumferential direction creates a flexible soft contact lens without buckling.

Power harvesting architecture, such as on-board antennas, and chip integration have both been demonstrated in various platforms [3,23,28]. Antenna fabrication utilises the same fabrication pathway as metal-layer interconnects, as does chip placement, in which a bump-bonding method is used [90]. A design has also been demonstrated which functions without on-board signal processing, relying on externally-driven resistance-varying sensors which passively transduce a signal into a modulation of the device's resonant frequency, as part of a RLC circuit [77]. Techniques such as this, in which some aspects of the measurement quality is sacrificed for the benefit of low-infrastructure operation, may represent crucial innovations for the shift towards unobtrusive sensing devices.

Micro- or nanoelectrodes are usually fabricated in a cleanroom using standard silicon processes (primarily photolithographic steps) [47]. Metallization layers, often gold or platinum, are deposited, patterned, and passivated with an insulating top layer. Vias are created through the insulating layer to expose the metal layer at the electrode sites. Methods have been developed to adapt this fabrication process to flexible substrates including polyimide [49,82,86–88], where a polyimide layer is often used as both the primary substrate and the insulating top layer. However (before this thesis), integration into an SCL platform, and in particular a platform with an established route to clinical use such as that demonstrated by Vásquez Quintero *et al*. [19] had not yet been demonstrated [16].

ESCLs face a particular challenge: the sensing sites must be in contact with the tear film in order to operate. Therefore, during each encapsulation step, consideration must be given to how the electrochemical sensor will remain in contact with the lachrymal fluid. Current designs are not encapsulated in hydrogel or silicone, and although rigid non-gas permeable lenses are workable in a research setting, safe extended use is not possible without suitable encapsulation. Possible methods to achieve sensor access include:

1. Windows may be created in each layer of the encapsulation to expose the sensing sites. A potential risk of this method is accumulation of proteins and lipids in the sensing sites, leading to biofouling and reduced sensing performance. This issue is of particular relevance to devices intended to be used for multiple days (as opposed to disposable 'daily' lenses). An overnight cleaning process may be able to alleviate some negative effects of biofouling. It is also possible that a window in the surface of the lens would

cause irritation at the cornea, depending on its size and shape, if the sensors are in- rather than out-facing.

2. Microfluidic channels may be created in the lens which draw tear film into the sensors and out after sensing. A blinking-mediated pumping method akin to muscolovenous pumping [91] could improve fluid flow. However, this would significantly increase the complexity of device fabrication, and biofouling of the channels could cause reduction in fluid transport.
3. Hydrogel materials which allow sufficient transport of the sensing species may be used, or hydrogels with active functionalisation may act as a part of the sensor itself [92].

Current ESCL designs use a single electrochemical sensor for a particular analyte (in one case including a second working electrode to act as a differential sensor [3]). The result of this is that they most likely make electrochemical measurements within the lachrymal lake, an indeterminately mixed fluid. Without considering the introduction, flow and drainage of tear fluid across the eye, the measurements these devices make contain a large degree of uncertainty about the nature of the fluid they are measuring. However, studies so far have only investigated sensor performance in the ocular environment in the broadest sense, demonstrating a qualitative response but with no benchmark of fidelity to the underlying concentration in the blood [15,77].

In addition, electrode designs in ESCLs have been of a somewhat undefined geometric form [1,2,15,77], generally following manufacturing constraints or tradition rather than innovating to suit the SCL environment. While these sensors are sufficient for qualitative analysis of bulk changes in concentration, the enhanced sensing properties of microelectrodes would lead to better accuracy and detection limit, more efficient use of power and space, and faster sensor response. A number of microelectrodes may be integrated into a single device, either to generate spatial information about the concentration distribution across the eye, to measure various different analytes in a single device, or both [16].

3 Spatiotemporal Sensing on a Flexible Microelectrode Array

Microelectrodes have a number of enhanced sensing properties when compared to macroelectrodes, which are of significant benefit to electrochemical measurement in the eye. They are also more spatially efficient, and draw less power, which makes them a promising class of electrode for SCL integration. Designing microelectrodes which can be integrated into the polyimide/TPU SCL platform developed by Vásquez Quintero *et al.* at Ghent University leverages state-of-the-art research in both microelectrode technology and material design in order to accelerate towards a clinically viable device.

The first step towards integration of microelectrodes into the polyimide/TPU SCL platform is to create a microelectrode device using the core polyimide substrate. In this way, the first stage of the fabrication process can be investigated, and the electrochemical methods developed and characterised, before further integration steps such as moulding and encapsulation are undertaken. In this chapter, the design, fabrication and characterisation of an 8 x 1 linear array of individually addressable microelectrodes built on a polyimide platform is described, and a new spatiotemporal electrochemical sensing method is demonstrated.

This chapter presents work some of which has been published in peer-reviewed articles [49,82].

3.1 Design

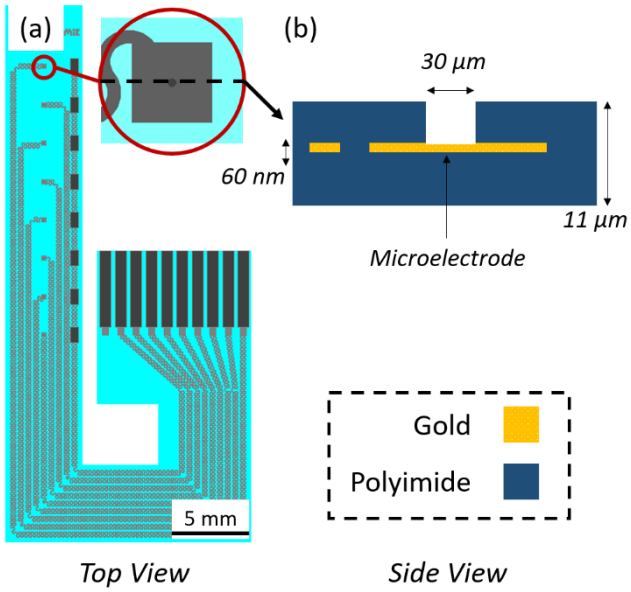

Figure 3.1: Design of the flexible microelectrode device. (a) Schematic top view of device, with inset showing a single microelectrode site. (b) Schematic cross-section of a microelectrode site. Dimensions not to scale.

An 8 x 1 linear array of individually addressable working electrodes was designed, with a set of common (shared) counter electrodes which are located such that each working electrode is proximal to a counter electrode site (Figure 3.1 a). The working electrodes are circular in shape (diameter 30 µm, located at the centre of a square pad, Figure 3.1 a inset. This form of electrode is termed a microdisc electrode), while each counter electrode site is rectangular (side lengths 450 µm, 950 µm). The device consists of a layer of gold (60 nm thickness, with an adhesion layer of titanium, 40 nm thickness) sandwiched between two layers of polyimide, both 5.5 µm in thickness (Figure 3.1 b). Previous work on a polyimide/TPU-based SCL platform by Vásquez Quintero *et al*. [19] determined that meandering connections for wires travelling in the radial direction of the lens helped eliminate buckling behaviour. Therefore, meandering connections were used in this device, following the optimal design characteristics described in Verplancke *et al*. [93], to investigate the effect of using meandering instead of straight wires. Connection pads were designed to fit in a zero insertion force (ZIF) connector with 1 mm pad spacing. As the finished device is only 11 µm in thickness, a paper spacer was necessary to avoid movement in the connector. The shape of the device was chosen to maximise connector to electrode path length (in order to enable easier separation of liquid

sensing media and connecting electronics), while also maximising number of devices fabricated on each 50 mm x 50 mm glass wafer (3 devices).

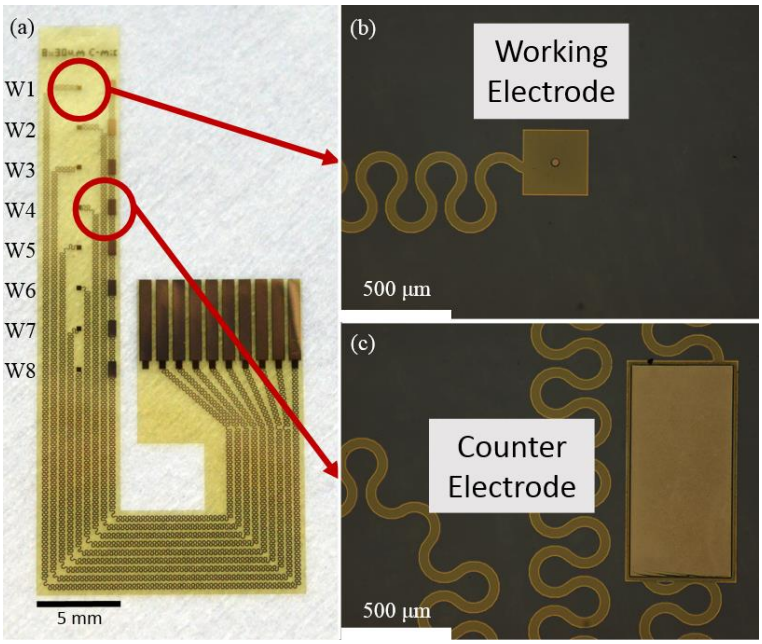

Figure 3.2: Images of the flexible microelectrode device. (a) Photograph of the flexible microelectrode array; the positions of working electrodes W1-8 are indicated. (b) Photomicrograph of one working electrode; the 30 µm diameter disc is situated in the centre of the square. The gold serpentine connections are visible through the transparent polyimide surface. (c) Photomicrograph of one part of the counter electrode; electrical connection is shared among all counter electrode sites.

Vias in the top polyimide layer expose the gold layer at the electrode sites and contact pads; therefore the fabrication method results in the working electrodes being recessed by a depth of 5.5 µm into the device (equal to the thickness of the upper layer of polyimide). Theoretical analyses suggest that recessing the microelectrode will result in a reduction of overall analyte flux by a factor of $\pi / (\pi + 4L)$, where L is the ratio between the recession depth and microdisc radius [94], which in this device results in a reduction in current of just over 30% compared to an inlaid microdisc. The device is flexible, and was proven to be robust during routine laboratory use. The position of the metal layer in the neutral mechanical plane protects the metal interconnects and electrode sites from damage during bending [90]. The working electrodes are denoted W1 to W8 (Figure 3.2 a, b); the on-board counter electrode (Figure 3.2 c) and an external reference electrode was used in this study.

3.2 Fabrication

Fabrication of microelectrodes on flexible substrates such as polyimide follows a similar process to that used on silicon [47], with the addition of polyimide deposition and final removal from the carrier wafer (square borosilicate glass wafers were used in this study). The fabrication steps are here described in chronological order, as follows.

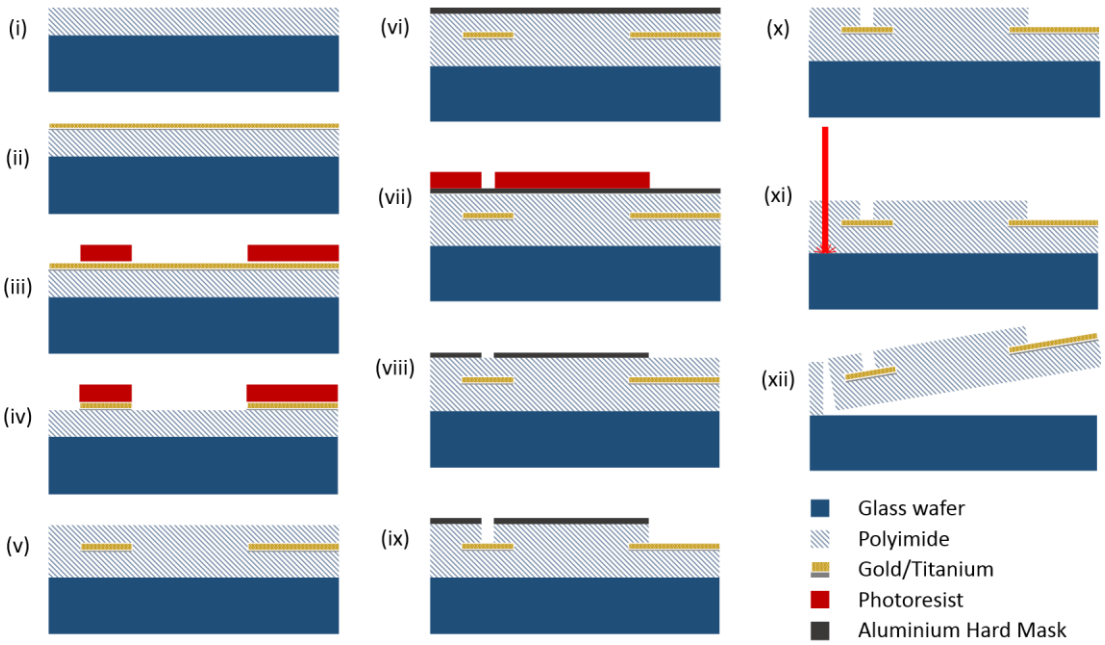

Figure 3.3: Schematic cross sectional images showing the process flow at significant stages. (i) Two layers of polyimide spin-coated onto glass wafer, (ii) Au/Ti deposited, (iii) Photoresist spin-coated then pattern defined, (iv) Au/Ti patterned by wet etch, (v) Polyimide spin-coated, (vi) Aluminium hard mask deposited, (vii) Photoresist spin-coated then pattern defined, (viii) Aluminium patterned by wet etch, (ix) Polyimide etched with reactive ion etching, (x) Aluminium hard mask removed by wet etch, (xi) edge of device cut by laser, (xii) Finished device lifted off glass wafer.

The glass wafer was cleaned and treated with a chemical adhesion promoter ((3-Aminopropyl)triethoxysilane, APTES), then a layer of polyimide (5.5 µm thickness, PI-2611, HD Microsystems) was spin-coated onto the wafer (3000 rpm, 30 s), dried on a hot plate (200 °C, 10 min) and cured in a nitrogen oven (RT to 200 °C at 4 °C min^{-1}; 20 min at 200 °C; ramp to 350 °C at 2.5 °C min^{-1}; 60 min at 350 °C). The polyimide is processed in a liquid state, and after dehydrating and curing becomes solid. Photolithography (S1818 photoresist, spin coating at 4000 rpm for 60 s, baking at 90 °C for 2 min, UV irradiance for 85 mJ cm^2, developing for 30 s with developer MF-319/deionized water (DI H_2O) at 1:1 ratio)

was used to cover the central working area of the mask, while reactive ion etching (RIE) (1 min, 150 W, 150 mTorr, 15 sccm O_2, 5 sccm CHF_3) was used to roughen the exposed perimeter area of the polyimide before removal of the photoresist (1 min in acetone, 1 min in acetone/isopropyl alcohol at 1:1 ratio, 1 min in DI H_2O). A second layer of polyimide was spin-coated (same parameters as before). The second layer of polyimide adhered strongly to the roughened perimeter area of the first layer of polyimide, but not strongly to the smooth central area. This ensured easier release of the devices (restricted to the central design area) after fabrication, while avoiding delamination of the second polyimide layer during processing.

RIE (same parameters as before) was used to roughen the second polyimide layer and promote adhesion before an adhesion layer of Ti was sputtered (40 nm), followed by a layer of Au (60 nm). The metal layer was patterned with photolithography (S1818 photoresist, same parameters as before) and wet etching (Au: solution of 1 g I_2, 4 g KI, and 73 mL H_2O for 2 min; Ti: H_2O_2 ->15'' (@50°C) + 10'' (@RT) + 1' DI H_2O). A third layer of polyimide (5.5 µm, same parameters as before) was spin-coated to cover the gold pattern. A sputtered thin film of Al (200 nm thickness) with adhesion layer (TiW) patterned by photolithography (S1818 photoresist, same parameters as before) and wet etching (Al: Solution CH_3COOH:H_3PO_4:HNO_3:DI at ratio (4(>90%):4(>89%):1(>65%):1(100%)) for 10 min; TiW: H_2O_2 ->15'' (@50°C) + 10'' (@RT) + 1' DI H_2O) functioned as a hard mask to define via holes in the top PI layer to expose the Au at the electrodes and the contact pads using RIE (55 min, 40 W, 150 mTorr, 15 sccm O_2, 5 sccm CHF_3). Al and TiW etchants removed the hard mask from the surface. The devices were then cut using a picosecond laser (355 nm, 12 ps, 50 kHz, 320 mW) to ablate the two layers of polyimide, with five passes at 20 mm s^{-1}, and delaminated from the wafer with tweezers.

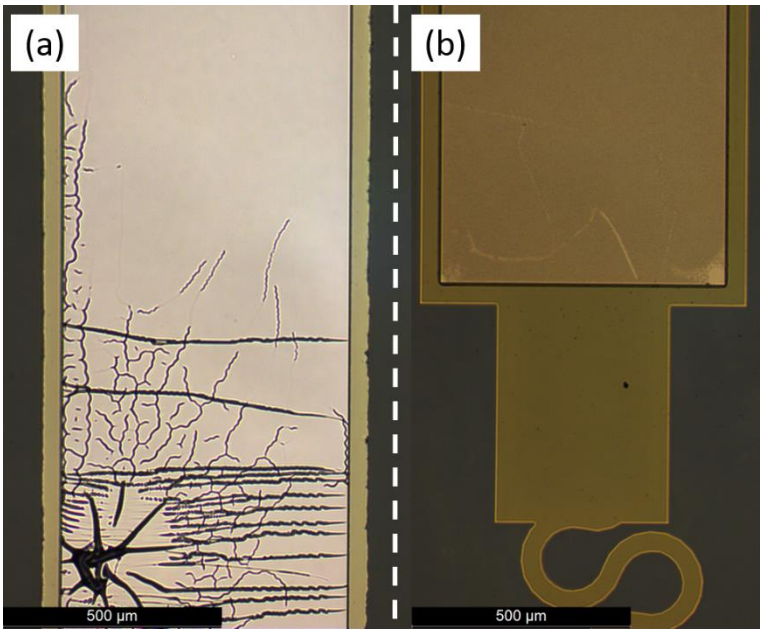

Figure 3.4: Platinum and gold metallization. (a) Photo micrograph of platinum metallization, showing significant damage at the exposed sites (a section of contact pad is shown in this image). No cracking damage is observed at the edges, where the stress shielding effect of the polyimide layers protects the platinum. (b) Photo micrograph of gold metallization, showing no damage at the contact pad.

An alternative design was trialled with platinum metallization instead of gold. Lift-off was used to pattern the platinum instead of wet etching, but roughness was observed at the edges of the platinum features (Figure 3.4 a). In addition, the platinum (a harder metal than gold) was significantly damaged at the larger exposed regions such as the contact pads and the counter electrodes, due to its stiffness relative to the substrate. (The platinum was undamaged in regions where the top layer of polyimide was present, due to the stress shielding effect of the polymer layers.) It was therefore determined that gold, which showed no evidence of damage after bending (Figure 3.4 b), was a better choice of metallization.

3.3 Electrochemical Characterisation

Ferrocenemethanol (Aldrich, 97% purity) was prepared at various concentrations in 0.1 M potassium chloride (Aldrich, 99% purity) with deionised water. Electrochemical experiments were carried out in a Faraday cage with a µAutolab potentiostat, using the on-device gold counter electrode and an external Ag/AgCl counter electrode (BASi, USA). Control and data acquisition were performed using General Purpose Electrochemical System (GPES, version 4.9).

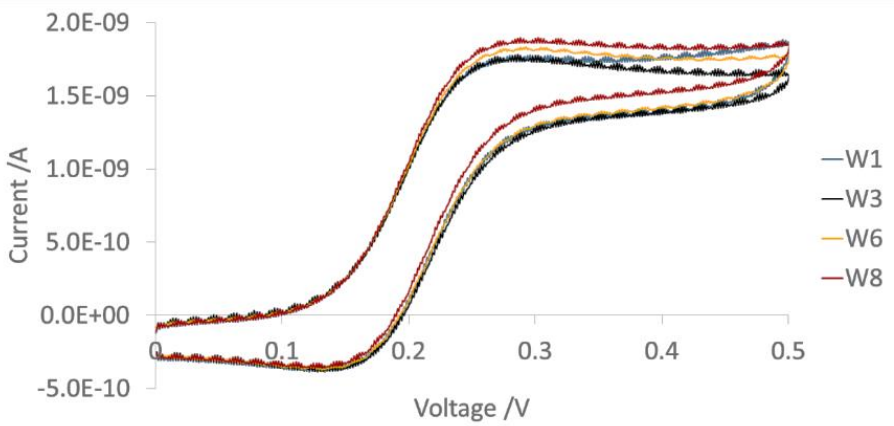

Figure 3.5: Results of cyclic voltammetry performed separately on working electrodes (W1, W3, W6 and W8 only shown in this figure) in ferrocenemethanol (FcMeOH, 0.5 mM) at a scan rate of 0.1 V s^{-1}.

The microdisc electrodes were characterised using a series of standard electrochemical methods. Cyclic voltammetry was performed in ferrocenemethanol (FcMeOH), a typical redox reporter, by sweeping the voltage between the working electrode and reference electrode from 0 V – 0.5 V – 0 V at a rate of 0.1 V s^{-1}, and measuring the current between the working and counter electrodes. The resulting cyclic voltammogram showed characteristic microelectrode responses, and little intra-device variation was observed between the working electrodes (Figure 3.5).

Experimental results were analysed using the Saito equation [95], which describes the limiting current, i_L, of a microdisc electrode in steady-state conditions, modified to account for the reduction in current due to recession into the substrate:

$$i_L = (4nFDc_0r)\left(\frac{\pi}{\pi+4L}\right) \quad (3.1)$$

where n is the number of electrons transferred in the reaction, F is the Faraday constant, D is the diffusion coefficient of the redox species (ferrocenemethanol), c_0 is the concentration, L is the ratio of recession depth to microdisc radius, and r is the radius of the microdisc. Values of $D = 5 \times 10^{-10}$ m^2 s^{-1} [47] and $c_0 = 0.5$ mol m^{-3} were used. A mean limiting current of 1.76 nA was found, while the theoretical model predicts a limiting current of 0.99 nA; i.e. an elevated current was drawn relative to theoretical expectations. This could be due to the increased resistance, capacitance and inductance of the meandering connection, and may suggest some degree of surface roughness, a feature which has been found to increase the limiting current of a microdisc electrode [96]. A roughness factor may be estimated based on the

effective area obtained by integrating the reduction peak of an H_2SO_4 cleaning cycle, and using the reported relation between charge and area (390 µC m^{-2}) [97]. In this way, a mean roughness factor of 4.2 was obtained across the electrodes (the ratio of the effective to geometric area).

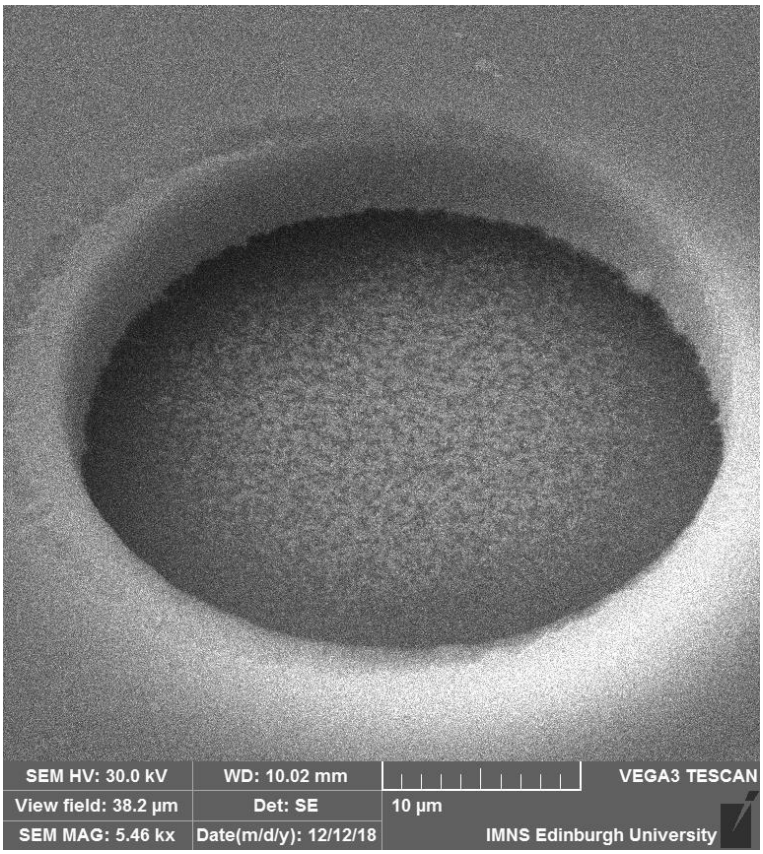

Figure 3.6: Scanning electron micrograph of a microdisc electrode.

Surface roughness of exposed gold areas was investigated during an earlier stage of work using the same fabrication method ([19], supplementary materials) and a root-mean-square roughness of 1.75 nm was measured using this reactive ion etch power of 40 W. Scanning electron micrographs also confirmed that the gold surface of the microelectrodes exhibited a degree of surface roughness (Figure 3.6). The increased current caused by this roughness during certain operations can be desirable, as it results in a more efficient use of the electrode area. However, the electrode performance is accordingly less well characterised, and does not agree well with the standard model for flat microdisc electrodes, although this was not a problem within the scope of this work.

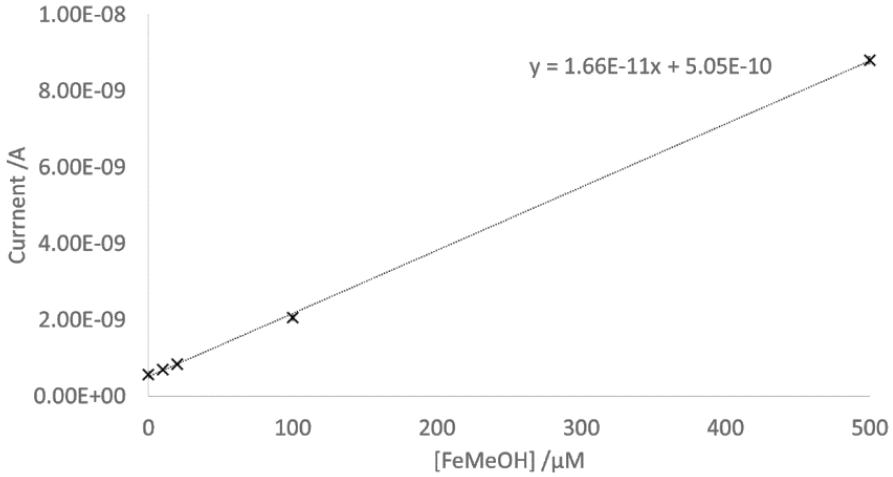

Figure 3.7: Current response of a microdisc electrode to a range of concentrations of FcMeOH; error bars are included.

Cyclic voltammetry was used to measure how the current responds across a range of concentration of FcMeOH, from 10 to 500 µM, and a 'blank' measurement of KCl (0.1 M). A linear current response was observed over the entire range of measurement (Figure 3.7), with $R^2 > 0.999$, indicating a very high confidence in the linear fit. Triplicate measurements were taken at each concentration and these were used to establish a limit of detection (LOD) following the IUPAC convention [98]:

$$x_L = \bar{x}_{bl} + k s_{bl} \tag{3.2}$$

where x_L is the smallest current that can be reliably detected, $\bar{x}_{bl}$ and s_{bl} are the mean and standard deviation respectively of the blank (KCl) measurement, and k is a numerical factor (a value of $k = 3$ was used to ensure a confidence level of > 99%). The LOD is obtained by substituting $x = x_L$ into the calibration function (Figure 3.7), giving the lowest concentration that can be detected at our chosen confidence level. Using this method a LOD of 0.016 mM was obtained. This result is comparable to that reported by Freeman *et al*. [46], in which a 100 µm diameter platinum disc electrode was found to have a LOD of 0.097 mM in ferrocene carboxylic acid, a similar redox reporter. Using an area ratio as a rough guide, it may be concluded that the 30 µm diameter microdisc electrodes have a LOD of the expected order of magnitude. Recessing the electrode into the polyimide substrate to a depth of 5.5 µm, which has the effect of reducing analyte flux by around 30%, may result in an elevated LOD compared to a non-recessed microdisc electrode.

3.4 Spatiotemporal Electrochemical Sensing

Various methods were explored during development of an appropriate spatiotemporal electrochemical method. Due to the potential impact on the size of the final ESCL design, integrating multiple counter and reference electrodes into the device was not considered to be satisfactory. It was also estimated that including multiple potentiostat units (i.e. one for each working electrode) into an embedded chip would increase the physical size and the power requirements to unmanageable levels, and set an undesirable limit on the number of working electrodes able to be supported by a single ESCL. Therefore, methods were considered which could be performed using a common counter and reference electrode, and a single potentiostat.

A measurement rate approaching video-speed was also preferred, in order to accurately track concentration variation across the surface of the eye. First, a potentiostat (Autolab PGSTAT128N) with in-built multiple working electrode capability was used to perform measurements at each working electrode in turn at a high rate. However, there was a non-negligible time delay during switching (approx. 50 ms), and significant noise was produced at the start of each measurement. These effects ultimately caused a relatively low measurement rate, with a poor signal quality. The method also used laboratory equipment of a large size with no clear path to miniaturisation.

A method was therefore designed which separated the complexity of fast-switching electrochemical methods into two well-characterised blocks: a potentiostat running a single extremely simple measurement protocol, and an analogue multiplexer which switches automatically between a series of outputs (i.e. the working electrodes). Miniaturisation of simple potentiostats has been demonstrated [3], and the addition of an analogue multiplexer incurs little additional complexity.

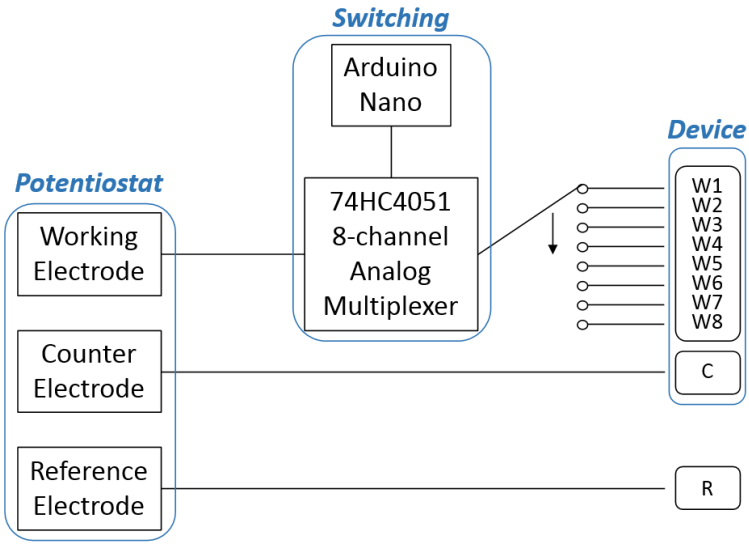

Figure 3.8: Schematic of the circuitry used for spatiotemporal experiments, illustrating the connections of the potentiostat (µAutolab) to the working electrodes (W1-8), via an analogue multiplexer driven by a microcontroller (Arduino Nano); to the on-device counter electrode (C); and to the external reference electrode (R).

The analogue multiplexer (74HC4051 8-channel) was driven by a microcontroller (an Arduino Nano [99]), which addressed the electrodes one-by-one in a cyclic sequence (Figure 3.8). Data processing was carried out using algorithms written in the Python programming language. This switching was performed constantly at a rate of 20 Hz (20 electrodes per second) while a potentiostat (µAutolab) was used to conduct chronoamperometric measurement at 0.4 V for 10 s. An in-device gold counter electrode was used, with an external Ag/AgCl reference electrode. Due to the rate of switching, higher currents were drawn compared to those found in cyclic voltammetry (Figure 3.5, Figure 3.9), resulting from the initial formation of the electrical double layer at the electrode site, and from parasitic capacitance, inductance and resistance in the device and the circuit beyond. Experiments were first carried out in a beaker. Calibration in KCl (0.1 M) and FcMeOH (0.5 mM) was performed, and subsequently an experiment was conducted in which FcMeOH was added by two separate injections of 1 mL volume each, using a micropipette, to a beaker of KCl (initial volume ~ 5 mL), while high-speed chronoamperometric measurements were taken as described above. Next, an on-droplet experiment was conducted to mimic a sensing environment analogous to that of a tear film under a SCL: the device was placed on top of a droplet of either KCl or FcMeOH solution to form a film of liquid between the active surface of the device and the glass underneath. After calibration, measurements were taken while FcMeOH was

injected into an initial KCl droplet of volume < 1 mL. Again, FcMeOH was added by two injections of 1 mL volume, with the micropipette placed at the W7-8 (working electrodes 7-8) end of the device.

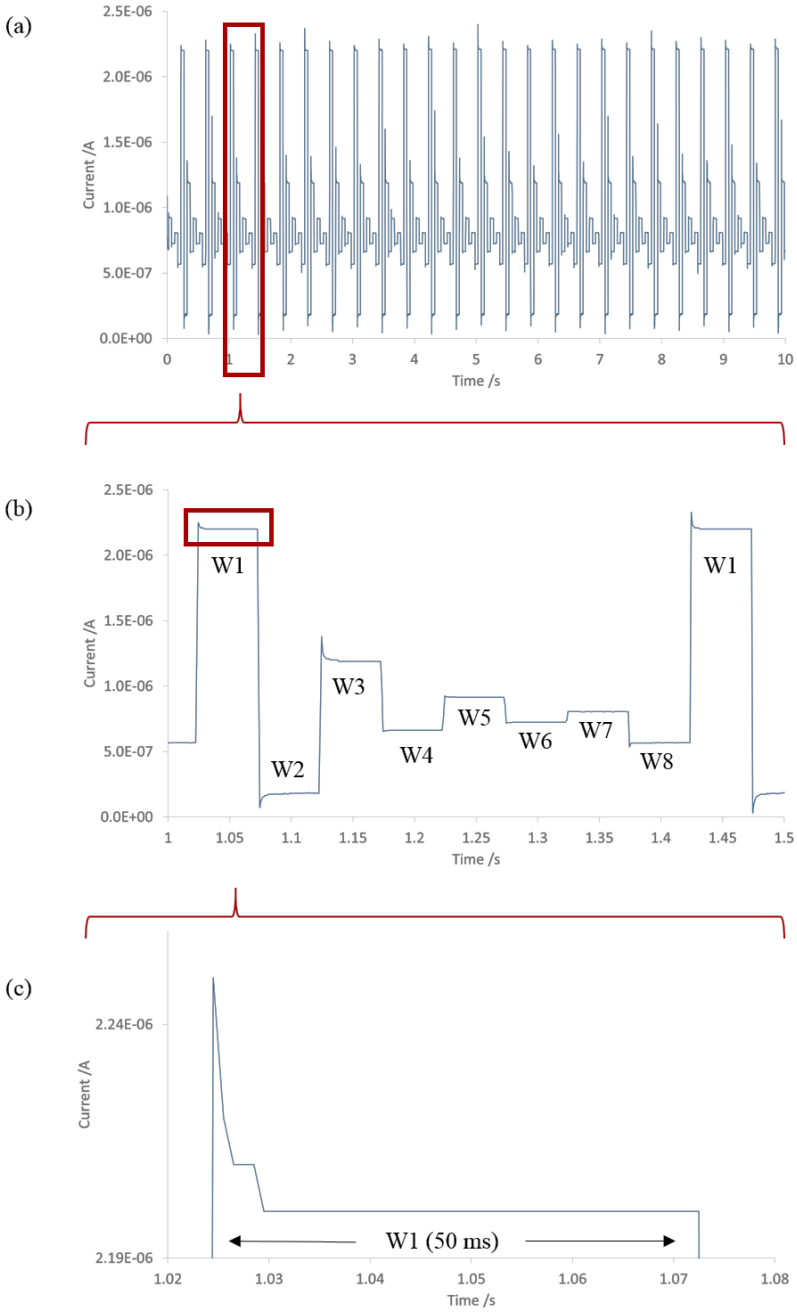

Figure 3.9: Raw data generated during fast-switching chronoamperometry. (a) Current measured over a 10 s experiment in a beaker of FcMeOH (0.5 mM) with the potentiostat running a chronoamperometric program, and multiplexer performing cyclic switching through the eight working electrodes. (b) Detail highlighted in (a), showing a complete cycle of the eight electrodes (denoted W1, W2 etc). (c) Detail highlighted in (b), showing a single electrode response.

Chronoamperometric data were collected in a single data stream with no sub-categorization of the individual response of each working electrode; the raw signal effectively consisted of a repeating eight-step sequence of 50 ms chronoamperometric measurements (Figure 3.9).

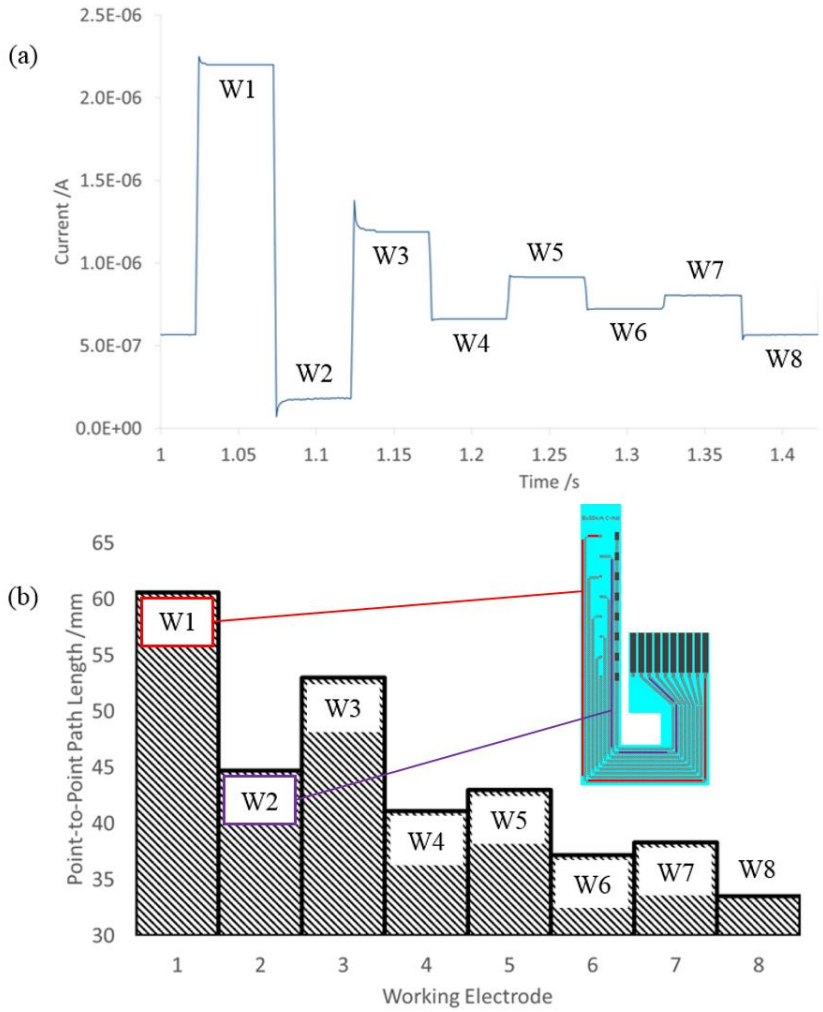

Figure 3.10: Intra-device variation in current drawn and path length. (a) Current measured during high-speed chronoamperometry, with the response of each working electrode illustrated (duplicated from Figure 3.9 b); (b) Electrical path length of each working electrode as measured from electrode to connection pad in-device. (Point-to-point path length is illustrated here; the true path length following the meanders would be a multiple of each of these values).

In electrochemical characterisation using cyclic voltammetry, at a sweep rate of 0.1 V s^{-1}, the current responses of the electrodes were found to be very similar (Figure 3.5). However, in high-speed chronoamperometric measurements (where the voltage step occurs at a rate greater than 400 V s^{-1}), a range of current responses was observed among electrodes (Figure 3.10 a). In high-speed

measurements, the effects of parasitic capacitance, inductance and resistance are of far greater importance. The current derived from the electrochemical response is combined with contributions from these additional effects. In this study, the variation in current response among the working electrodes was found to follow the variation in path length of meandering connections within the device (Figure 3.10 b; path length of in-device connections is variable, see Figure 3.1 a). It follows that part of the variation in current drawn during high-speed measurement derives from the variation in length of electrical connections in the device. Wire connections in the subsequent circuitry were also not always equal between electrodes; therefore it is likely that similar effects contributed beyond the device as well as within.

Electrical path length is greatly increased using meandering connections rather than straight wires. In a small device, proximity of connection paths is also usually increased with meanders. Although in this study the effect of parasitic capacitance, induction and resistance was easily corrected for during calibration, it is worth noting this result of using meandering connections and potentially limiting their use when not necessary, e.g. for wires in the circumferential direction of a smart contact lens [19].

An algorithm was designed to detect and separate the signals from the eight individual working electrodes (W1-8). Mean current was obtained from the 25 ms to 45 ms segment of each 50 ms sub-measurement. This period was chosen to avoid the initial non-Faradaic signal and any switching noise at either end of the measurement period. This process generated a single data point from each sub-measurement, each labelled to one of the eight working electrodes. Linear interpolation was used to smooth the data between pairs of consecutive time points and to avoid a rolling refresh effect, since the data at each electrode is updated only once in every eight samples.

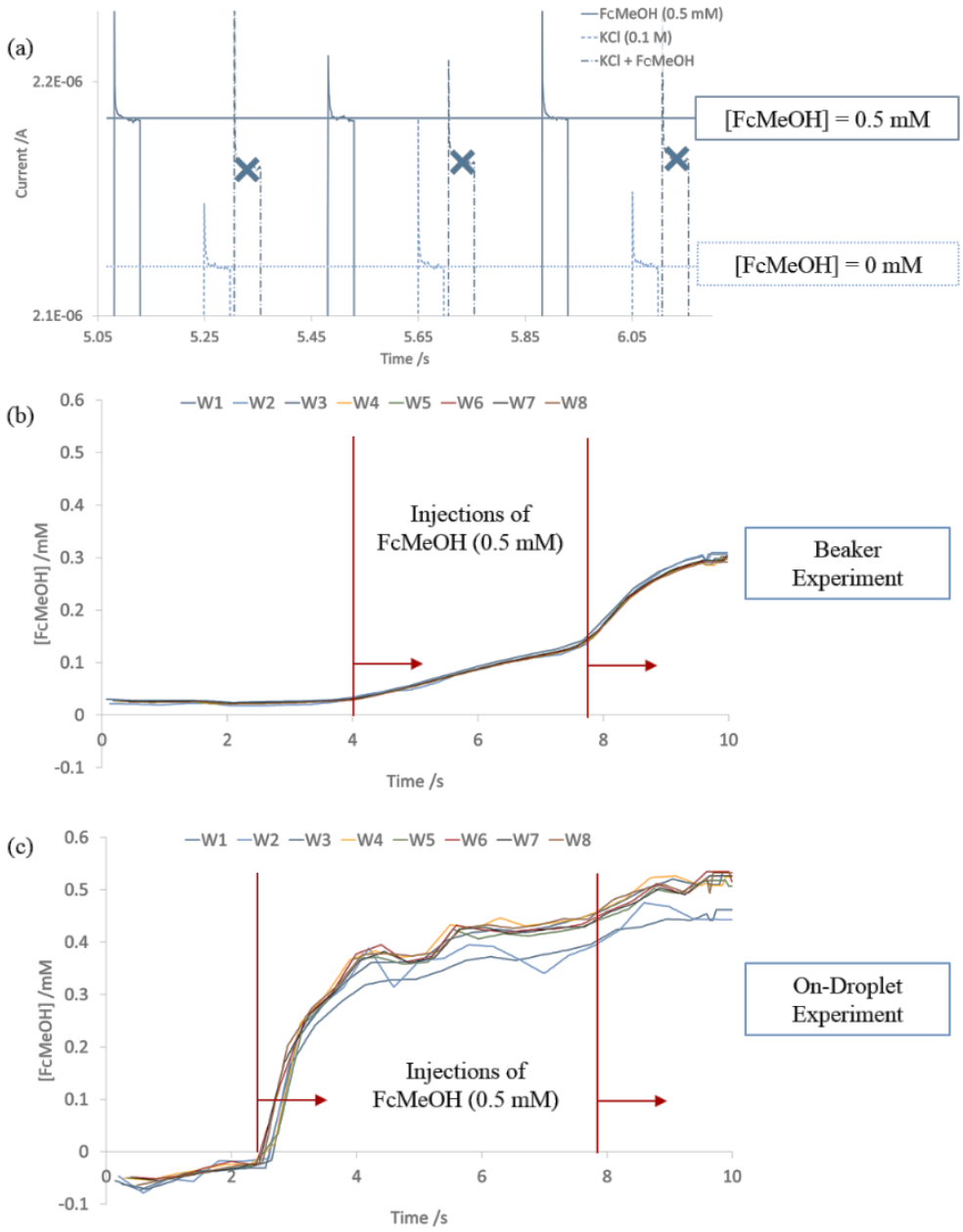

Figure 3.11: Signal processing during spatiotemporal electrochemistry and the results of two experiments. (a) Detail of the signal from W1 during on-droplet measurements of 'high' (FcMeOH 0.5 mM), 'zero' (KCl 0.1 M) and variable ('KCl + FcMeOH', where FcMeOH was injected into a KCl droplet at the W7-8 end of the device) concentrations. Annotations illustrate the calibration method. (b) FcMeOH concentration at all electrodes throughout the 10 second beaker experiment. Injections of FcMeOH are illustrated. (c) FcMeOH concentration at all electrodes throughout the 10 second on-droplet experiment. Injections of FcMeOH are illustrated. (Note: a single anomalous data point has been removed in W1)

Calibration between an average 'high' value (FcMeOH, 0.5 mM) and 'zero' value (KCl, 0.1 M) was performed individually for each working electrode. Figure 3.11 a

provides a detail of this process during the droplet experiment, showing three measurements (only W1 shown for clarity): the W1 ‘high’ (indicated with a solid horizontal line), W1 ‘zero’ (indicated with a dotted horizontal line) and the signal generated by W1 during time-varying concentration (‘KCl + FcMeOH’, marked with crosses). Figures 2.11 b and c show the time-varying concentration at each working electrode over the 10 second measurement period for the beaker experiment and the on-droplet experiment. In the beaker experiment there was virtually no spatial inhomogeneity of concentration across the device, and thus the eight working electrodes recorded almost identical concentrations at all times. The effects of the two injections of FcMeOH can be clearly observed in the data; the concentration rises slowly as the FcMeOH mixes with the KCl solution.

In the on-droplet experiment, the measured concentration rose very quickly upon the first injection. This was likely due to bulk flow of FcMeOH pushing the initial KCl film away. Diffusive and turbulent mixing would have taken place at the interface of the two fluids, but in the laminar flow regime it is likely that the incoming fluid simply pushed away the majority of the initial fluid with only a minor amount of mixing. Thus, the measured concentration rose to nearly 0.5 mM after the first injection (I1). The effect of the second injection (I2) was not so pronounced, because the concentration under the electrodes was already fairly high. It is also possible to observe in the data at various times a difference in the concentration observed at each electrode (Figure 3.11 c, e.g. at the second injection, t = 8), as fluid mixing was less efficient in this experiment compared to the beaker experiment, resulting in a not-always-homogeneous concentration across the device. These effects are explored in more detail with reference to Figures 2.12 a and b, but in Figure 3.11 c it is already clear that W1-2 experienced a slightly lower concentration throughout the experiment; since FcMeOH was injected from the W7-8 end of the device, it is likely that the initial KCl droplet was pushed in the direction of W1-2, resulting in this lower concentration. Figure 3.12 c also shows that the W1-2 end of the device was situated closer to the glass at the start of this experiment, such that the KCl situated there would have moved and mixed less readily than the rest of the droplet.

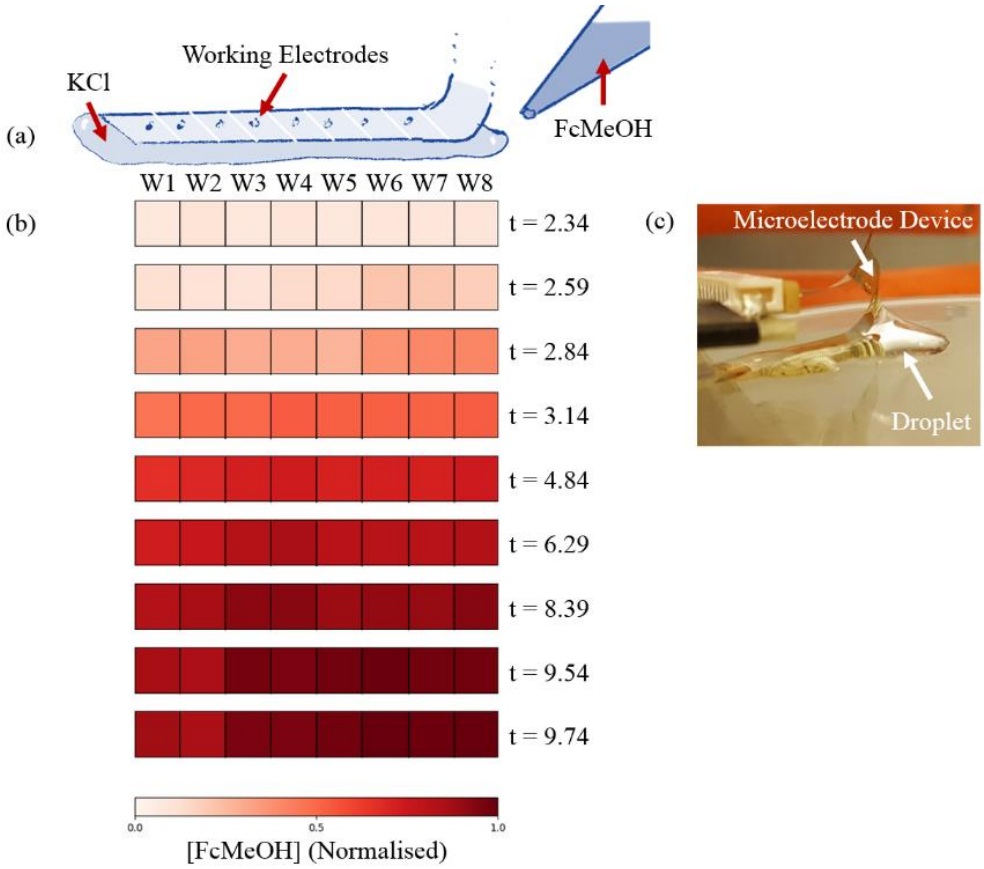

Figure 3.12: Visualisation of a spatiotemporal electrochemical measurement. (a) Illustration of the droplet experiment in schematic cross-section. FcMeOH is injected into a droplet of KCl from the W8 end of the microelectrode device (reference electrode not shown). (b) Still "frames" from the colour map "video" of concentration across the device. Time points are chosen to illustrate various features of the flow, particularly at I1 ($t \approx 2.5$) and I2 ($t \approx 8$). See Video 3.1 (Supplementary Materials) for full video. (c) Photograph of experimental setup, showing the microelectrode device resting on a KCl droplet (reference electrode not shown).

In order to better visualise the concentration flow the data were rescaled between 0 and 1, which was then used to prepare a colour map representing concentration at each electrode site (Figure 3.12 b). This can be viewed in real time (Supplementary Materials), while Figure 3.12 b shows some representative frames from the video. It is possible to see in these frames the initial injection of FcMeOH (from the W7-8 end of the device, e.g. t = 2.59 to 2.84) followed by mixing and homogenisation after I1 (e.g. t = 3.14). The effects of I2 can be seen in the same way (e.g. t = 8.39, where a larger volume underneath W3-8 perhaps allowed circular mixing which was observed at W3-4 before W5-6) and the unmixed solution at W1-2 (e.g. t = 9.54). When viewed in its entirety, the electrochemical video provides a clearer

visualisation of the flow of analyte across the device, with both bulk flow and diffusive mixing visible.

3.5 Conclusion

A linear 8 x 1 array of individually addressable microelectrodes was designed and fabricated on a flexible polyimide substrate. The device was flexible and robust to mechanical deformation when gold metallization was used, with no observed damage after manual deformation or standard laboratory use, while platinum metallization was observed to undergo damage after bending of the device. Standard electrochemical characterisation procedures produced expected microelectrode-like behaviour, while both circuit effects and increased surface roughness of the gold working electrodes was found to lead to a larger than expected current drawn during cyclic voltammetry. A spatiotemporal electrochemical method was described and demonstrated using the microelectrode device, and examples of spatiotemporal concentration variation in a beaker and a droplet experiment were illustrated.

The findings from this study were used to inform the next stage of device design. The useful section of the signal produced during fast-switching chronoamperometry was much smaller than the total current drawn from each working electrode, which also varied significantly from electrode to electrode. Meandering connections contributed to this issue due to their increased parasitic capacitance, inductance and resistance during high-speed electrochemical measurements when compared to straight wires. In an ESCL, meandering connections may be avoided by designing wires to travel only in the circumferential direction, and avoiding radial travel (since previous studies have shown that connections in the radial direction must be of a pre-defined serpentine form to avoid buckling behaviour in the substrate after thermoforming). The useful section of the signal could be also increased, and therefore signal to noise ratio decreased, by using connected arrays of microdisc electrodes instead of individual microelectrodes.

No significant flaws were encountered with this design or fabrication method, and it was concluded that the polyimide core of the polyimide/TPU SCL platform is a suitable substrate for microelectrode arrays built for SCL integration.

4 Flexible Through-Flow Ultramicro and Nanoband Electrodes

Miniaturisation of the working electrode in an electrochemical system improves sensing performance. However, reducing feature size in the image plane of photolithographically-defined structures incurs increasing cost in terms of design, tooling, process complexity and materials. Nanoelectrodes – electrodes with at least one relevant dimension smaller than 100 nm – can be fabricated more easily in a nanoband architecture, using the thickness of deposited metal layers to define the nano-dimension of the electrode, since very thin films of metal can easily be deposited in a standard cleanroom.

Nanoband electrodes have not been widely reported on flexible substrates, but there is no fundamental reason that the silicon-based process could not be adapted to a flexible substrate. However, in this chapter a further-simplified fabrication process is presented which avoids the need for conventional photolithography and instead combines thin-film technology with laser excision to produce flexible nanoband electrodes capable of being produced on a roll-to-roll basis. The same core polyimide technology found in the polyimide/TPU SCL platform is used, with a view to possible integration of these nanoband electrodes into an ESCL.

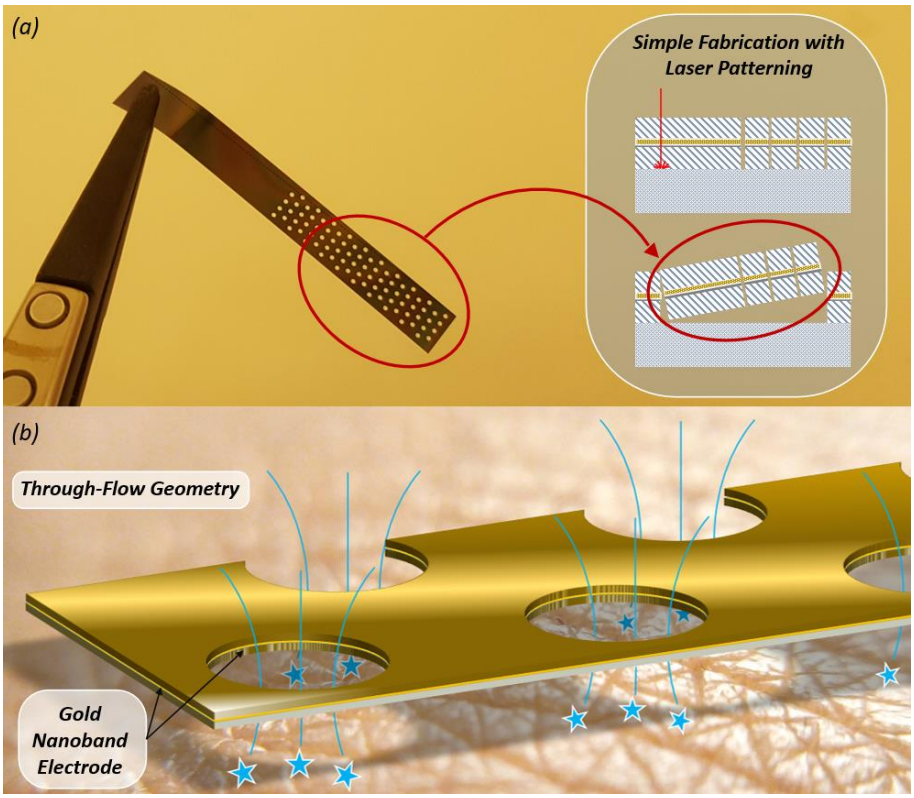

Figure 4.1: Overview of the through-flow electrode device. (a) Photograph of a nanoband mesh electrode device, with a schematic cross-section showing part of the fabrication method. (b) Visualisation of the through-flow geometry of the electrodes during on-skin sweat sensing.

The fabrication process produces a connected array of nanoband electrodes of arbitrary planar form, with the unusual property of a through-flow architecture (Figure 4.1). The sensing medium is free to flow past the nanobands, which (for certain scenarios such as flow environments like the tear film, or on-skin measurement) can engender a more efficient sensing environment. In this chapter the design and fabrication of these devices, characterisation of the physical form of the electrode sites, the electrochemical sensing properties, and the resilience to mechanical deformation and damage are demonstrated and discussed. A through-flow experiment, in which the device acts as an active-sensing filter through which a flow of fluid of varying concentration passes, is also illustrated. Finally, possible integration into an ESCL platform is discussed.

4.1 Design

The nanoelectrode devices comprise a layer stack of polyimide (5.5 µm), gold metallization (60 nm) with a titanium adhesion layer (40 nm), and a second layer of polyimide (5.5 µm). The total thickness of the stack is 11 µm. Due to the planar nature of the layer stack, all electrode sites shared an electrical connection via the gold metallization. After construction of the layer stack, electrode sites were digitally defined using laser excision. The laser could operate in two modes: localised pulse, or a continuous line. In this study two different devices were designed to investigate the electrochemical properties of the two main electrode geometries which could be created in these two modes: macropore (Figure 4.2) and micropore (Figure 4.3). Devices with features created by continuous line excision would be generally analogous to the macropore electrodes, while the micropore electrodes were created by localised laser pulses and represent the minimum feature size producible with this laser. The macropore electrodes consisted of a 4 x 20 array of circular holes (diameter = 455 µm), visible to the naked eye. The micropores consisted of either a 20 x 100 array of teardrop-shaped holes (diameter ≈ 22 µm) with 200 µm spacing, or a 16 x 100 array with 160 µm spacing.

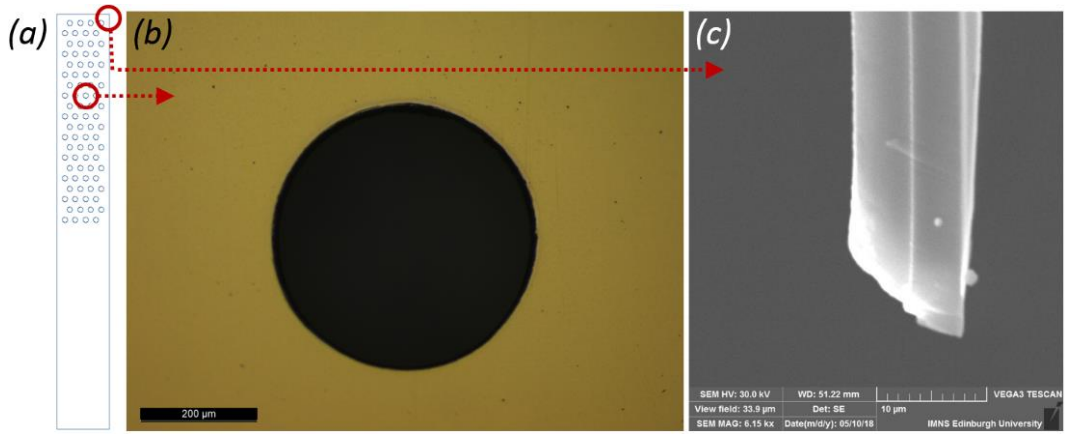

Figure 4.2: The macropore device. (a) Digital design schematic. (b) Photo micrograph of a macropore electrode. (c) Scanning electron micrograph of the side-view of the corner of the device, showing the layer stack, gold nanoband and edge profile.

The macropore electrodes were designed such that the predominant form of the diffusion field would be cylindrical. The radius of curvature of the macropore shape (228 µm) is much greater than the thickness of the nanoband (60 nm), and hence the diffusion field may be approximated as that of a linear nanoband. Scanning electron microscopy of the sidewall after continuous laser excision shows the gold

nanoband in the centre of the two polyimide layers (Figure 4.2 c). For any planar design with radius of curvature much larger than the nanoband thickness a linear nanoband approximation is valid.

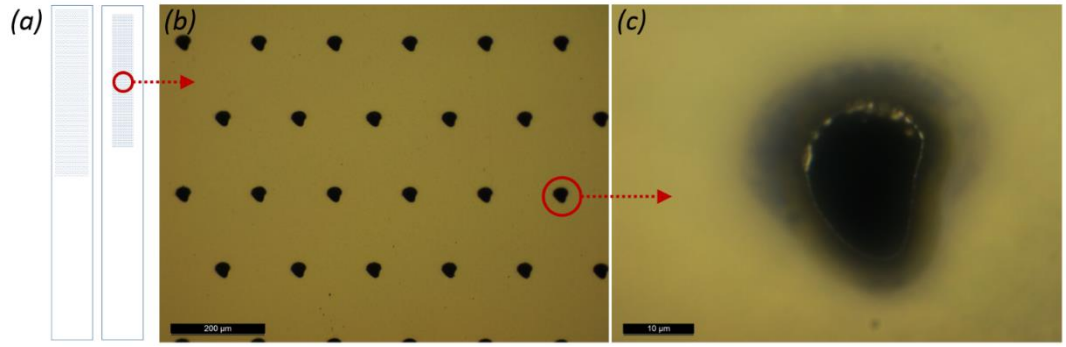

Figure 4.3: The micropore device. (a) Digital design schematics for both sparse and dense array types. (b) Photo micrograph of the micropores. (c) photo micrograph at higher magnification, showing the gold band in the middle of the stack.

Micropore devices were created with both dense and sparse array types (Figure 4.3 a). The denser array (160 µm spacing) was used for imaging to increase feature representation, but all electrochemical tests were carried out with the sparser array (200 µm) to minimize diffusion field overlap.

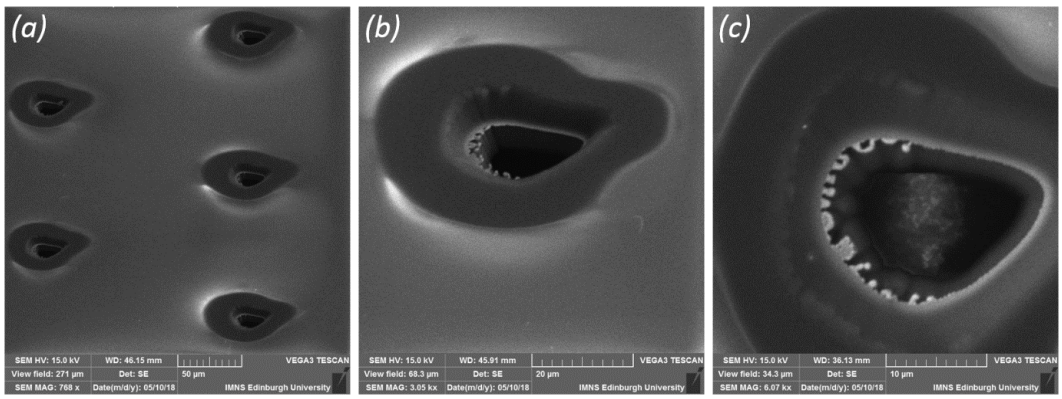

Figure 4.4: Scanning electron micrographs of the micropore electrodes at 45° (a, b) and top-down (c). An electron-depleted region is visible around the ablation site, and a filigree-like pattern of gold is seen in the wider part of the pore.

The physical form of the macro and micropores was characterised using a combination of optical microscopy and scanning electron microscopy. The electrode sites in the macropores were defined by the sidewall profile produced during laser ablation, while the micropore electrodes derived both their sidewall angle and their shape from the beam characteristics. The micropores exhibit minimal variation from

pore to pore and across different devices (Figure 4.3 b, Figure 4.4 a). The laser produced teardrop shaped holes with an average sidewall angle of 52° to horizontal (Figure 4.4 b, c), though the angle is shallower at the top and becomes steeper after the Au/Ti layer (Figure 4.5). Thus, the pore area at the top was larger than at the bottom (762 μm^2 and 235 μm^2 respectively).

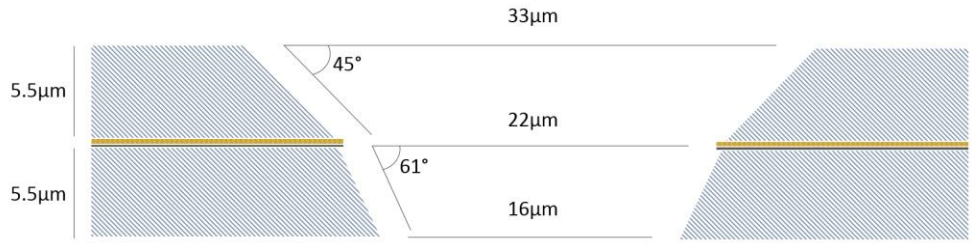

Figure 4.5: Schematic of the micropore sidewall profile. The laser produces holes that are wider at the top of the substrate than the bottom.

The micropores all contained a filigree-like pattern of gold at the wider part of the teardrop; this was consistently of the order of 1-2 µm in size, and was remarkably similar in every micropore (Figure 4.4 c). It is hypothesised that this derived from the effect of heat dissipation in the gold during laser ablation: the widest part of the ablation site receives the least laser intensity and excess heat dissipates into the surrounding metal, such that this filigree pattern represents to some extent the channels of energy flow during the ablation process. Experiments with a less powerful laser produced holes with larger filigree patterns, which provides some support for this hypothesis. Due to this feature, it is more appropriate to class the micropore electrodes as ultramicroelectrodes rather than nanoelectrodes.

Visible in the scanning electron micrographs, but not in the optical microscope images, is a dark region surrounding each micropore. It is hypothesised that the laser partially oxidised the polyimide in the blast region, resulting in fewer electrons available for detection during scanning electron microscopy (which operates by detecting secondary electron emission). This effect may have subtle consequences regarding electrochemical performance, particularly in the speed at which double-layer capacitance is formed at the electrode sites during measurement, though investigation of this effect is outwith the scope of this thesis.

4.2 Fabrication

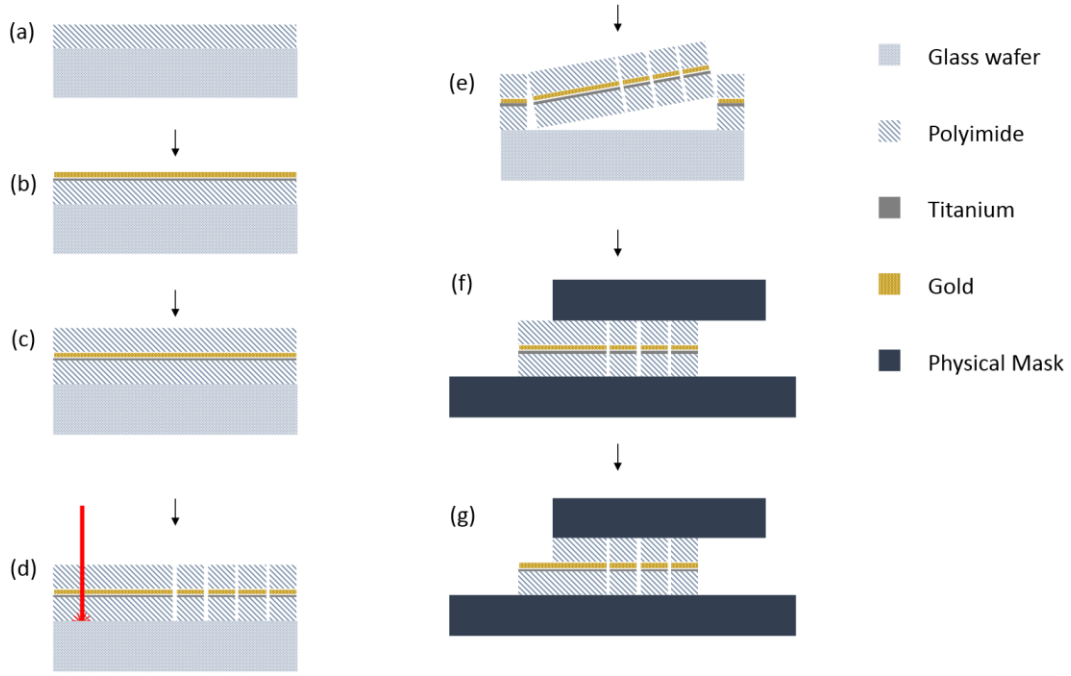

Figure 4.6: Sequence of schematic cross-sections illustrating fabrication steps for the nanoband mesh electrodes. (a) Two layers of polyimide spin-coated onto a glass wafer. (b) Au/Ti sputtered onto the polyimide. (c) A second layer of polyimide spin-coated over the metal layer. (d) Laser ablation defines electrode sites and device shape. (e) Device is released from glass wafer. (f) A physical mask defines contact pad areas. (g) Reactive ion etching removes top layer of polyimide to expose gold contact site.

The glass wafer was cleaned and treated with a chemical adhesion promoter ((3-Aminopropyl)triethoxysilane, APTES), then a layer of polyimide (5.5 µm thickness, PI-2611, HD Microsystems) was spin-coated onto the wafer (3000 rpm, 30 s), dried on a hot plate (200 °C, 10 min) and cured in a nitrogen oven (RT to 200 °C at 4 °C min^{-1}; 20 min at 200 °C; ramp to 350 °C at 2.5 °C min^{-1}; 60 min at 350 °C). Photolithography (S1818 photoresist, spin coating at 4000 rpm for 60 s, baking at 90 °C for 2 min, UV irradiance for 85 mJ cm^2, developing for 30 s with developer MF-319/deionized water (DI H_2O) at 1:1 ratio) was used to cover the central working area of the mask, while reactive ion etching (RIE) (1 min, 150 W, 150 mTorr, 15 sccm O_2, 5 sccm CHF_3) was used to roughen the exposed perimeter area of the polyimide before removal of the photoresist (1 min in acetone, 1 min in acetone/isopropyl alcohol at 1:1 ratio, 1 min in DI H_2O). A second layer of polyimide was spin-coated (same parameters as before). The second layer of polyimide adhered strongly to the roughened perimeter area of the first layer of polyimide, but

not strongly to the smooth central area. This ensured easier release of the devices (restricted to the central design area) after fabrication, while avoiding delamination of the second polyimide layer during processing.

An adhesion layer of Ti was sputtered (40 nm) followed by a layer of Au (60 nm). A second layer of polyimide was spin-coated using identical settings to the previous two. A picosecond laser (355 nm, 12 ps, 50 kHz, 320 mW) was used to ablate the two layers of polyimide and the gold, using five passes at 20 mm s^{-1}, in order to define the outlines of the devices and to etch the pores. For the smaller pores, a localised pulse was used to create the smallest possible opening, while the larger pores were defined by a circular path and the edges by straight paths. The devices were delaminated from the wafer using tweezers. To etch contact pads, a physical mask (e.g. a glass slide) was used to cover most of the device, with only the desired contact region left exposed. The top layer of polyimide was ablated using reactive ion etching (60 mTorr, 15 sccm O2, 5 sccm CHF3, 80 W).

An alternative method to create electrical contact without reactive ion etching would be to pierce the device with multiple small pins (i.e. a crocodile clip with very sharp teeth). This could eliminate the need for the final step in the fabrication process described above.

4.3 Electrochemical Characterisation

For electrochemical measurements, ferrocenemethanol (Aldrich, 97% purity) was prepared at various concentrations in 0.1M potassium chloride (Aldrich, 99% purity) with deionised water. Electrochemical experiments were carried out in a faraday cage where possible, using a µAutolab potentiostat, with a platinum counter electrode and an Ag/AgCl reference electrode (BASi, USA), in static solution unless stated otherwise. Control and data acquisition was performed using General Purpose Electrochemical System (GPES, version 4.9).

4.3.1 Theoretical Model

In steady-state conditions, the limiting current of a microdisc electrode is described by the Saito equation [95]:

$$i_l = 4nFDc_0r \qquad (4.1)$$

where n is the number of electrons transferred in the reaction, F is the Faraday constant, D is the diffusion coefficient of the redox species (ferrocenemethanol), c_0 is

the concentration, r is the radius of the microdisc, and i_l is the limiting current. From triplicate measurements at a concentration of 0.5 mM and a sweep rate of 0.1 V s^{-1}, a limiting current of i_l = 1.56 µA was calculated. In order to isolate the behaviour of the micropores a separate test was performed in which the edges of the device were covered with epoxy (since the edges of the device acts as a linear nanoband). It was found that 51% of the current derives from the micropores, which yields a value of $i_{l,micropores}$ = 0.80 µA. This number was used in the following analysis, and values of D = 5×10^{-10} m^2 s^{-1} [47] and c_0 = 0.5 mol m^{-3} were used.

It was assumed that the analyte flux from each side of the substrate was equivalent in this theoretical model to a separate electrode site. Recession of the electrode in a microdisc (and circular nanoband) has been calculated to reduce analyte flux by a factor of $\pi/(\pi + 4L)$ where L is the ratio between the recession depth and microdisc radius [94], and this analysis considers the smallest radius in the analyte diffusion field from each sides of the substrate, i.e. a minimum radius of r_{above} = 11 µm from above and r_{below} = 8 µm from below, while the recession depth is 5.5 µm in both cases (Figure 5). As the electrode spacing is much greater than the electrode size, largely independent diffusion fields can be assumed; thus total current is defined as:

$$i_l = 2000 \times i_{l,single} \ , \tag{4.2}$$

where $i_{l,single}$ accounts for diffusion from both above and below. Finally, a standard recessed nanoband electrode yields approximately half the current of a microdisc of the same radius [46], yielding

$$i_{l,theory} = \frac{2000}{2}(4nFDc_0)\left(\frac{\pi r_{above}}{\pi + 4L_{above}} + \frac{\pi r_{below}}{\pi + 4L_{below}}\right) \tag{4.3}$$

and a theoretical limiting current of $i_{l,theory}$ = 1.1 µA. This value is within the same order of magnitude as (and slightly higher than) the observed limiting current of 0.8 µA. Reduction in current versus the theoretical model may result from (i) accidental coverage of micropore sites while covering the edges of the electrode in epoxy, and (ii) some tolerance due to the approximations made regarding physical pore structure (since the models assume straight-wall recessed architecture), as well as other deviations from the ideal model such as polymer substrates, sidewall inhomogeneity and more. However, this result is a good indication that the micropores act akin to recessed nanoband electrodes with two-fold diffusion characteristics from the through-flow architecture.

Linear nanobands along the sidewall of an exposed edge do not have a well described theoretical limiting current in the literature, but the cyclic voltammetric measurements indicate approximately 4× current increase per unit area using linear nanobands when compared to micropores. This may be attributed to the open nature of the sites, and the fact that the diffusion field can wrap all the way around the thin substrate.

4.3.2 Electrochemical Testing

Nanoelectrodes excel in two primary characteristics: low limit of detection, and the ability to perform measurements at a much faster rate than macroelectrodes [44]. These features were investigated with a benchmark comparison to similar nanoband sensors fabricated on silicon [45]. The effect of sweep rate on the diffusion and mass transport characteristics of the electrodes was also investigated.

Cyclic voltammetry was used to investigate how the current responds to various concentrations of FcMeOH, ranging from 0.5 to 500 µM. Triplicate 'blank' measurements of 0.1 M KCl were performed, and these were used to establish a limit of detection (LOD) following the IUPAC convention [98]:

$$x_L = \bar{x}_{bl} + k s_{bl} \tag{4.4}$$

where x_L is the smallest current that can be detected, $\bar{x}_{bl}$ and s_{bl} are the mean and standard deviation respectively of the blank (KCl) measurement, and k is a numerical factor (a value of $k = 3$ was used to ensure a confidence level of > 99%). The LOD is obtained by substituting $x = x_L$ into the calibration function of the device (Figure 4.7), giving the lowest concentration that can be detected at our chosen confidence level. Using this method, a LOD was be determined for each device (Table 4.1).

Table 4.1: Limit of detection of a nanoband device, a macroelectrode of equivalent area, and the nanoband mesh devices.

Device	Limit of detection [µM]
Macroelectrode (Platinum Disc) [46]	97
Nanoband array [46]	0.10
Macropore mesh device	0.12
Micropore mesh device	0.67

In previous literature a silicon-based recessed nanoband array achieved an LOD of 1.0×10^{-7} M with ferrocene carboxylic acid, a similar redox reporter [46]. The authors also calculated the LOD of a macroelectrode of equivalent area (Table 4.1). This nanoband array had a total electrode area of 1.1×10^{-8} m^2; using a value of 60 nm nanoband width, a macropore device electrode area of 1.0×10^{-8} m^2 is calculated, and a micropore device electrode area (including edges) of 1.1×10^{-8} m^2. It is therefore asserted that the silicon-based nanoband array is a good benchmark against which to compare the devices in this study, due to the electrode area and the similar geometry of the electrode sites.

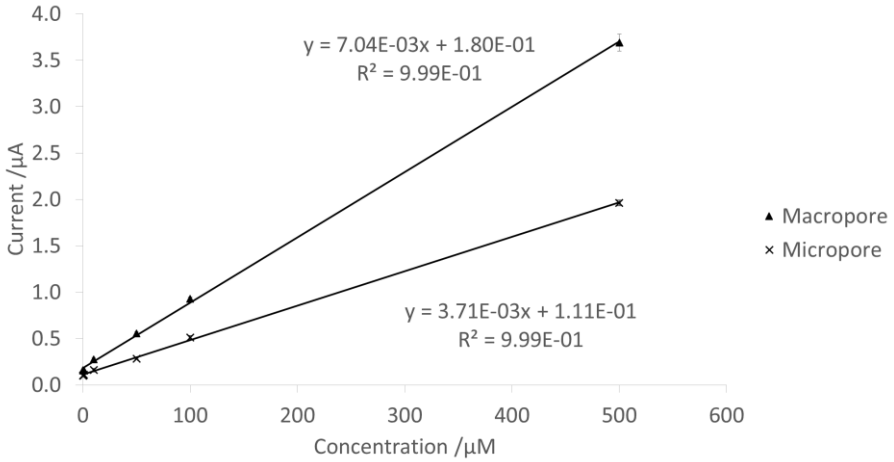

Figure 4.7: Current response to a range of concentrations for the macropore and micropore devices.

Both the macropore and micropore devices exhibited a highly linear current response to change of concentration, with R^2 values > 0.999 for the linear fit (Figure 4.7). We calculated a LOD of 6.7×10^{-7} M for the micropore device, and 1.2×10^{-7} M for the macropore device (Table 4.1).

These results indicate that the sensors exhibit sensitivity on the same order of magnitude as other state-of-the-art nanoband devices, without requiring expensive photolithographic techniques. It is interesting to note that the macropore device performed a little better than the micropore; the gold filigree-like structures found in the micropores were not observed in the linear nanoband areas (i.e. the macropores and the device edges), and it is therefore hypothesised that these regions display more nanoband-like behaviour than the micropores. Since the linear nanoband structures also exhibited a higher current drawn per unit area when compared to the micropores, it may be concluded that features made using the laser operating in a

continuous mode have better sensing characteristics than those made using localised pulses, although the small pores formed during the latter method may bring other benefits, such as flow-speed control and physical filtering of sensing media.

Chronoamperometry and cyclic voltammetry were both performed at the rate limit of the µAutolab potentiostat to determine how quickly a reliable measurement may be taken. Cyclic voltammery was performed at a sweep rate of 3 Vs^{-1}, which, with voltage steps of 1.06 mV, gave a sampling time of 350 µs. Chronoamperometry was performed with a sampling time of 50 µs.

Cyclic voltammograms were taken in triplicate using a macropore device. Very low deviation was seen between measurements and no anomalies were observed, demonstrating that the devices performed well at this rate (Figure 4.8 a). In the slightly faster case of chronoamperometry, triplicate measurements were taken and error plotted for each time point (Figure 4.8 b). The consistently low error observed here leads to the conclusion that the devices perform well at the operational limit of our potentiostat, giving a working sample rate of at least 20 kHz.

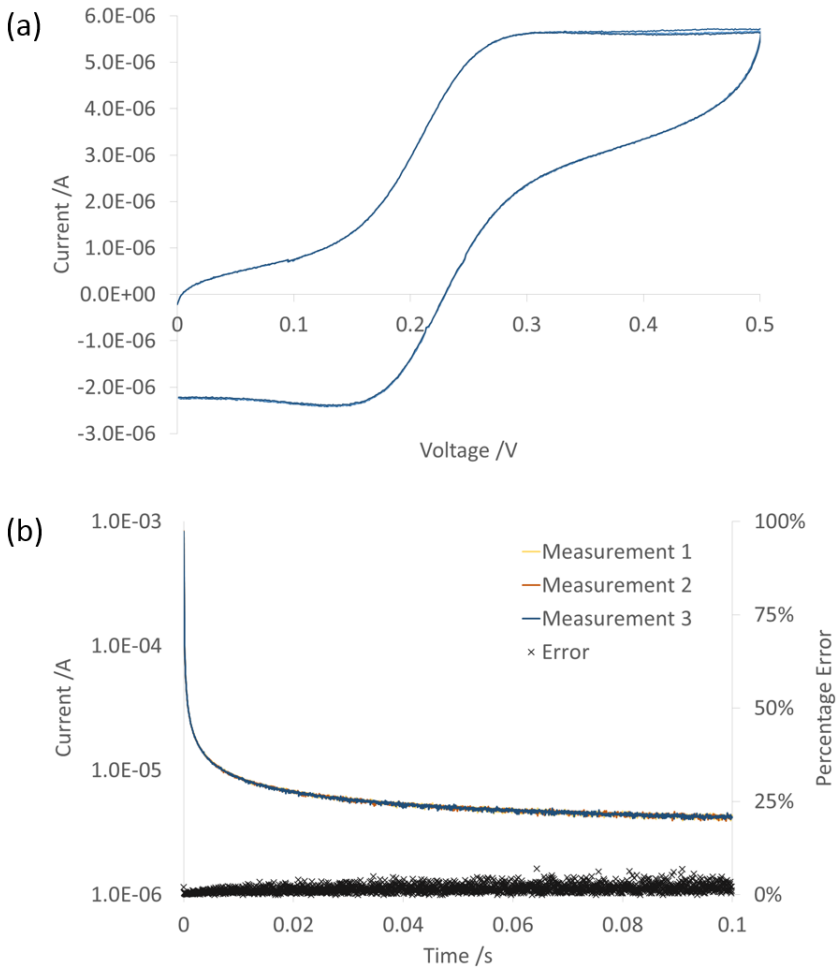

Figure 4.8: Cyclic voltammetric and chronoamperometric investigations into response speed. (a) Cyclic voltammetry at a sweep rate of 3 Vs^{-1}, performed in triplicate and demonstrating no errors or anomalies between the three measurements. (b) Chronoamperometric measurements performed in triplicate, demonstrating low measurement error at all time points.

Cyclic voltammetry shows a near-sigmoidal response at a sweep rate of v = 0.1 V s^{-1} (Figure 4.9), which is characteristic of a nanoelectrode array in steady-state conditions [45]. There is some current from parasitic capacitance, which arises through non-Faradaic charging of the capacitance between the gold layer and the solution through the polyimide substrate [45]; this additional current may be observed in the difference between the forward and backward sweeps, and it is possible to correct for it either with a blank (KCl only) measurement, or more approximately by averaging the forward and backward sweeps. The capacitive current is proportional in magnitude to sweep rate v (which is clearly demonstrated in Figure 4.9) and is insensitive to potential.

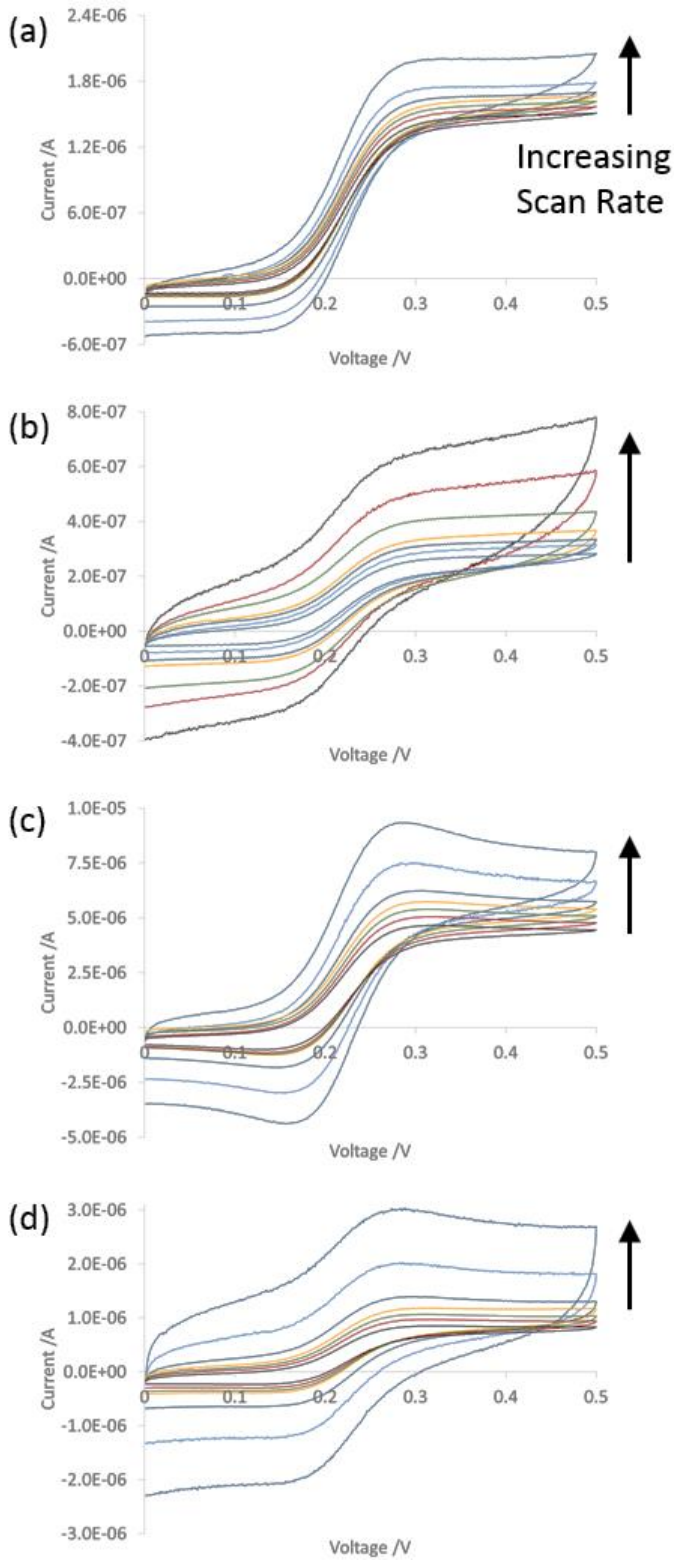

Figure 4.9: Cyclic voltammetry of FcMeOH in 0.1 M KCl, at sweep rates of 25, 50, 75, 100, 200, 500 and 1000 mV s^{-1}: (a) Micropore device at 0.5 mM FcMeOH, (b) Micropore device at 0.1 mM FcMeOH, (c) Macropore device at 0.5 mM FcMeOH, (d) Macropore device at 0.1 mM FcMeOH.

At very slow sweep rates the diffusion field of each electrode site grows to the point where they begin to overlap. The closer the features (micropores, macropores or linear nanobands), the higher the sweep rate at which this overlap will occur. This results in a decrease in area efficiency over time, as the diffusion fields eventually combine and mass transport approaches the macroelectrode case.

4.3.3 Electrochemical Performance after Mechanical Testing

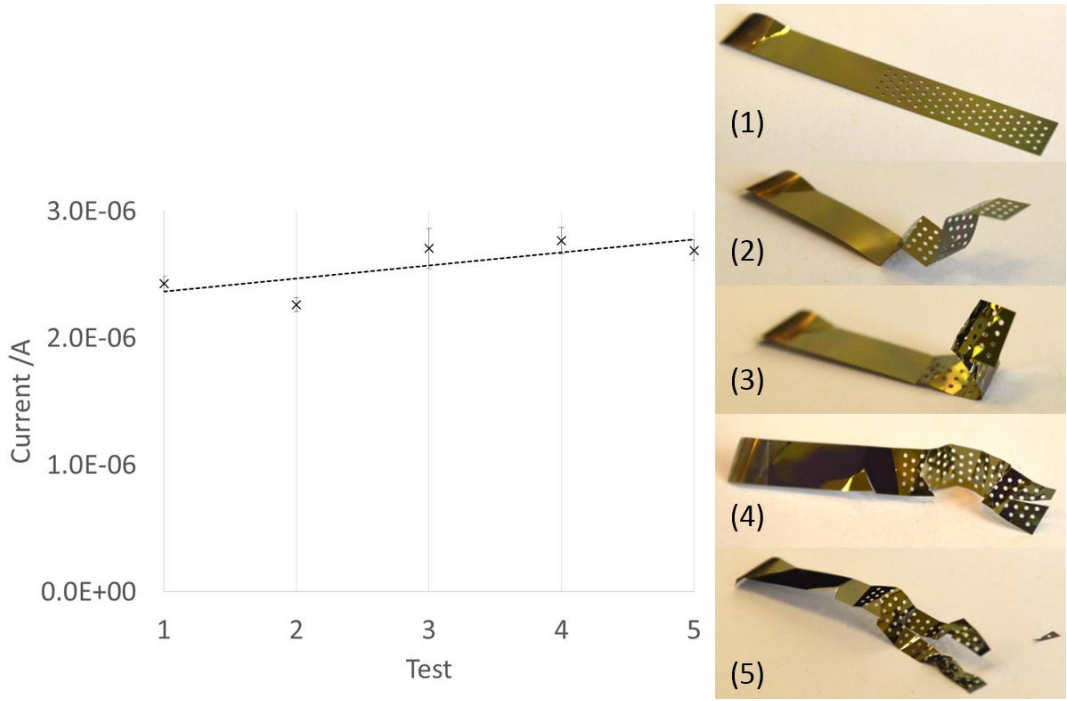

Figure 4.10: Current response to 0.5 mM FcMeOH after progressive stages of damage: (1) the original state, (2) multiple permanent folds, (3) permanent crumpling and scratching, (4) three small cuts added, (5) a large cut added which bisects the sensing area, and removal of a small piece of the device.

Cyclic voltammetry was performed at various stages of mechanical deformation and damage to investigate the effect on sensing performance of the nanoband mesh electrodes (Figure 4.10). Although non-Faradaic charging current increased as more folds and cuts were introduced, when this was compensated for (by averaging the current during the forward and backward voltage sweeps) very little change was observed as damage progressed. Thus, while the nanoband mesh devices are extremely thin compared to silicon- or even polymer-based electrode devices [100–102], with overall thickness of 11 µm and a gold layer thickness of only 60 nm, they appear to be remarkably robust to mechanical deformation, likely due to the strength of the polyimide layers and the fact that the metal layer resides in the neutral mechanical plane. During bending the polyimide layers experience tensile or

compressive forces, while the gold layer experiences (virtually) no such force. This design protects the integrity of the metal layer, and allows the sensor to continue functioning unaltered under severe mechanical stress or deformation, as demonstrated in Figure 4.10 (1-3). Additionally, the electrode sites are largely protected from physical damage such as scratching by their position in the sidewall of micropores, or the edges of the device in general. In the event of a cut through the device, or even a piece missing, the nature of the substrate is such that there is significant redundancy in the sensing array and robust electrical connection is maintained, as demonstrated in Figure 4.10 (4-5).

4.4 Through-Flow Experiment

To test the devices in a flow environment, an experiment was designed in which fluid of varying concentration flowed through a micropore electrode array, such that the array acted akin to an active-sensing filter.

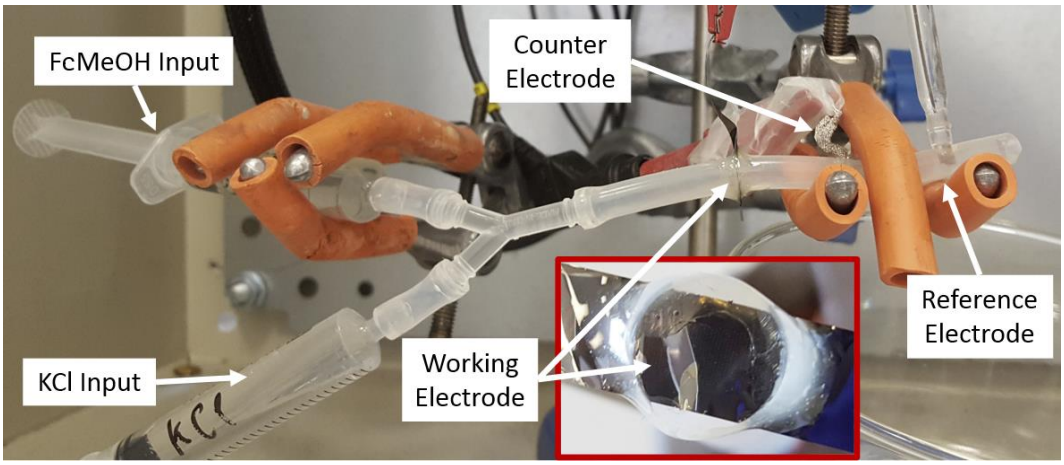

Figure 4.11: Photograph of the experimental setup during the through-flow tests. Inset shows a cross-sectional photograph of the nanoband mesh electrode acting as a filter through which flowing liquid passes.

A flow cell was created with two fluid inputs: KCl (0.1 M) and FcMeOH (0.5 mM). The two syringes were connected in a Y-junction into the main flow line (Figure 4.11); the fluid then passed through the micropores of a nanoband mesh electrode, sealed into the flow line using epoxy resin (Figure 4.11 inset), which acted as the working electrode. A counter electrode (platinum wire mesh) and reference electrode (Ag/AgCl) were inserted into the flow line after the working electrode.

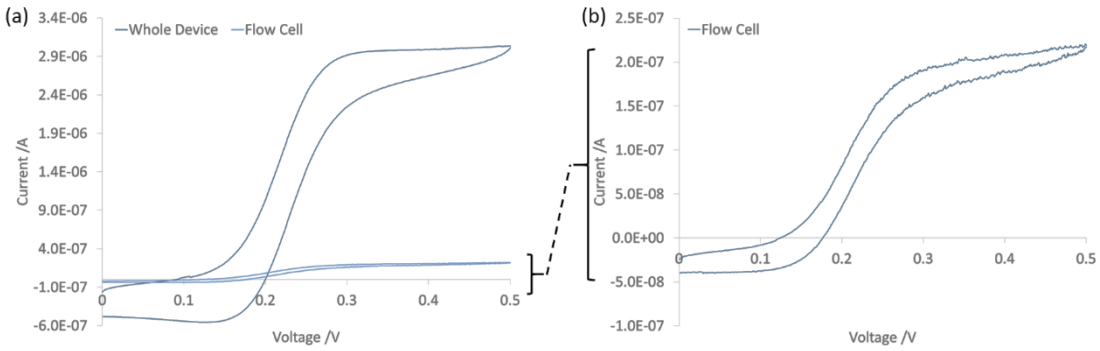

Figure 4.12: Cyclic voltammograms before and after integration of the nanoband mesh into the flow cell. (a) Both cyclic voltammograms. (b) Re-scaled plot of cyclic voltammogram taken after integration.

Cyclic voltammograms taken in static fluid before and after integration of the device into the flow cell showed an expected decrease (slightly greater than 10×) in current (Figure 4.12), as only a subset of the micropores and none of the device edge were in contact with the sensing medium. The characteristic form of the current response to cyclic voltammetry was preserved after integration (Figure 4.12 b).

Chronoamperometric measurement was performed (0.4 V for 30 s) during which 'high' concentration (FcMeOH, 0.5 mM; KCl, 0.1 M) and 'zero' concentration (FcMeOH, 0 mM; KCl, 0.1 M) fluid was pumped alternately through the flow cell. Figure 4.13 shows three measurements taken during different pumping profiles, in which the blue shading indicates pumping of FcMeOH and the white indicates KCl, while the guidelines indicated the approximate level of 'high' and 'zero' concentrations. The design of the flow system results in a non-binary concentration measured at the working electrode; instead, evidence of mixing and flushing of the previous fluid is observed, with a characteristic decay trending from high concentration to zero (e.g. Figure 4.13 b, t = 12 s), or vice versa (e.g. Figure 4.13 a, t = 11 s). With established linearity in this concentration range (Figure 4.7), a simple calibration method should be sufficient to infer the concentration of the fluid passing through the nanoband mesh electrodes, although, due to the effects of flow-mediated replenishment of analyte in the diffusion fields, the relationship between current measured and concentration may be flow-speed dependant.

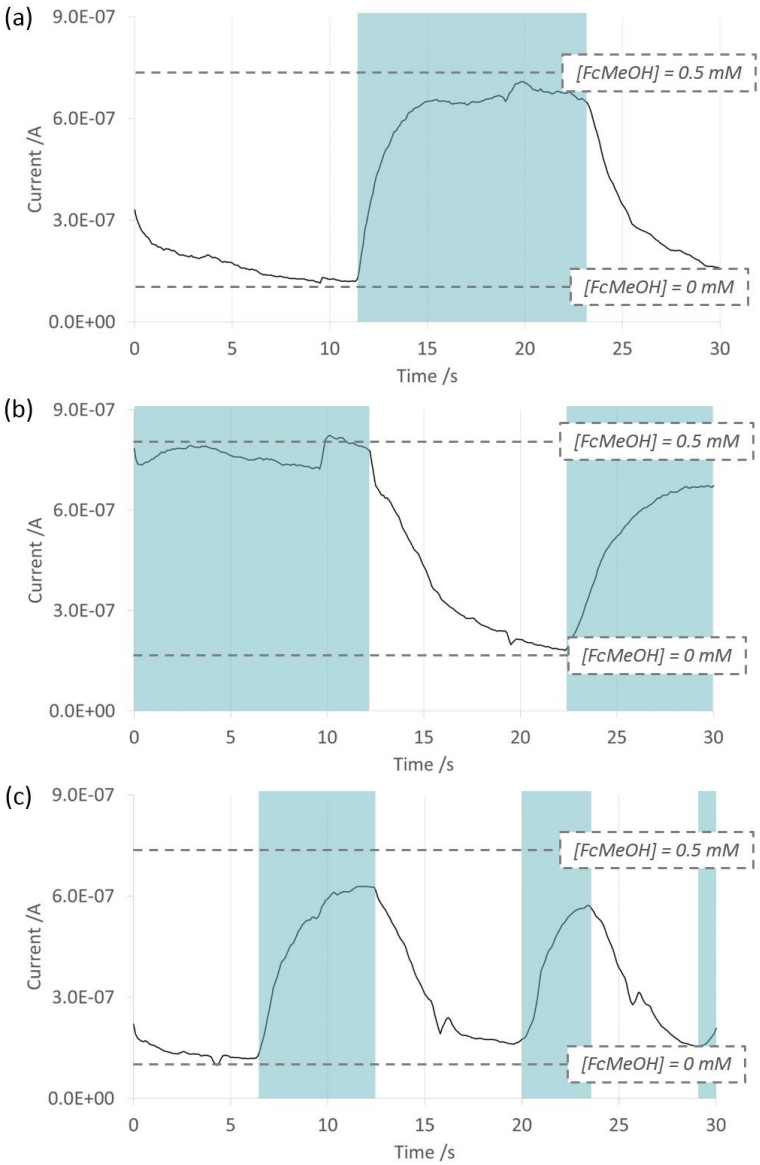

Figure 4.13: Current response during three 30 s chronoamperometric measurements in which 'high' and 'zero' concentration FcMeOH was pumped through the flow cell at various times. Shaded sections indicate flow of 'high' concentration FcMeOH, and approximate guides of the maximum 'high' (0.5 mM) and 'zero' (0 mM) concentration values are indicated by dashed lines.

In addition to through-flow architectures in flow cells such as this, suitable for continuous monitoring of concentration profiles of analytes in (e.g.) automated fabrication, water purification, fluid analysis, etc, a similar architecture may be achieved in sweat sensing. Electrochemical sweat sensors currently face the challenge of fluid pooling either underneath or on top of the device, rendering the measurements made therein inaccurate, since the newer sweat is mixed indeterminately with older fluid. By combining the nanoband mesh electrodes with a

wicking fabric on top, sweat would be drawn through the device into the fabric and wicked away, ensuring that only the most recent, and therefore most accurate, concentration levels are measured.

4.5 Conclusions

In this chapter, a new method of fabricating flexible nanoband electrodes has been introduced and discussed. Physical characterisation of the electrode sites created during different laser excision modes was described. The electrodes performed well during electrochemical characterisation, with comparison to equivalent macroelectrodes and equivalent silicon-based nanoband electrodes indicating preservation of the desired nanoelectrode sensing characteristics when adapting nanoband technology to this flexible substrate and simpler fabrication method. The devices proved extremely robust to mechanical deformation and damage, which, combined with the possibility of a cheap roll-to-roll production method, suggests that this work could lead to a viable high-quality disposable biosensor technology. A through-flow sensing architecture was illustrated by a flow cell experiment, in which a nanoband device provided continuous information on the concentration of a fluid flowing through the micropores. This may have applications in biosensing, for example in tattoo-based electrochemical sensors, in which sweat could be monitored as it flows through a skin-mounted device. It may also be applicable to production environments in which fluid flows need to be monitored for their chemical composition.

Due to the need to integrate separate components such as silicon chips and an antenna into an ESCL, the utility of a photolithography-free fabrication method is made somewhat redundant. Nanoband electrodes also may be more vulnerable to biofouling, as the architecture of both the macropores and micropores are less well-defined, deeper, and rougher than planar microelectrodes. It was therefore determined that a microelectrode technology would be a better choice for ESCL integration. However, the excellent sensing performance derived from using an array of connected nanoelectrodes in this study indicated that connected arrays of microelectrodes may improve the quality of electrochemical measurements taken in the eye when compared to the single microelectrodes designed in Chapter 3.

5 Interpreting Measurements Made in the Tear Film

In most cases, electrochemical measurements performed in the tear film are intended to be used to create estimations of the corresponding concentration of the analyte in the blood. However, the time-varying concentration profile of an analyte in the blood is not simply replicated in the tear film. The physiological processes which transport the analyte from the blood stream into the lachrymal fluid result in a complex mathematical distortion of the initial time-series profile; i.e. the time-series trend of concentration in the tear fluid is a distorted version of that in the blood. Therefore, if electrochemical measurements are taken in the tear film and assumed to be an accurate indication of concentration in the blood, the conclusions made using this data risk being catastrophically inaccurate.

In Chapter 3 a spatiotemporal electrochemical method was discussed which would provide information about the flow of lachrymal fluid across the eye, therefore producing more accurate information about the in-flowing fluid, in order to reduce the measurement distortion inherent to ESCLs. However, the distortion resulting from the transport of analyte from the blood to the lachrymal fluid must also be corrected for if sufficiently accurate estimates are to be achieved.

In this chapter a method based on a neural network is described which corrects this measurement distortion. Crucially, it learns a patient's individual measurement distortion, and assumes very little about the nature of the underlying process, making it patient-specific, generic, and applicable to a wide range of analytes and measurement scenarios.

5.1 Theory & Methods

The problem of measurement distortion has been observed and well-described in the case of glucose measurement in the interstitial fluid (ISF) [7]. However, the relationship of glucose concentration in the blood to the ISF is comparatively simple to the case of lachrymal fluid, and can be modelled using a two-compartment model to a degree of accuracy which is acceptable in clinical use. Calibration to an individual patient is usually necessary due to variation in physiology, but after calibration the mathematical model sufficiently corrects for the difference between glucose concentration measured in the ISF and that found in the blood to make useful diagnostic conclusions. In contrast, measurements performed in the tear film

face a greater challenge in correcting measurement distortion, as the analytes progress through a more complex metabolic pathway in reaching the tear fluid from the blood plasma.

To draw accurate conclusions from non-invasive measurements such as those made in the tear film it is necessary to correct for the difference between the measured data (i.e. the measured concentration in the tear film) and the underlying data (i.e. the concentration in the blood), which includes (but is not limited to) the difference between the concentration of analyte in the sensing medium and the concentration in the blood (as in most cases it is blood-analyte concentration with which we are concerned). This challenge is made difficult by a number of factors:

1. The metabolism of analytes, and the pathways by which they find their way from the blood to the sensing media, are complex and not always well-understood.
2. These metabolic profiles and pathways are patient-specific – it is not sufficient to measure the relationship between (e.g.) tear-glucose and blood-glucose in one patient and to assume the same relationship exists in another patient [67,103].
3. The metabolic profile may be situationally dependent – e.g. cortisol secretion has been found to be covariate with a range of other factors, including eating a meal [104], while performing exercise, sleeping, or the time of day may alter the proportion of blood glucose which is filtered through into the tear film or sweat.

An example of (2), above, is found in interstitial fluid (ISF) glucose, where a time constant characterizing the transfer rate of blood glucose into ISF ranges from $\tau = 7.1$ min to $\tau = 20.5$ min among different patients [7].

The consequence of these factors is that currently (in Q4 2019), in most cases, it is not possible to safely use data derived from non-invasive monitoring. It is also likely that simply assuming a lag/bias relationship between the measured and underlying data would be too simplistic, and would not lead to sufficiently accurate interpretations of data generated from tear film measurements.

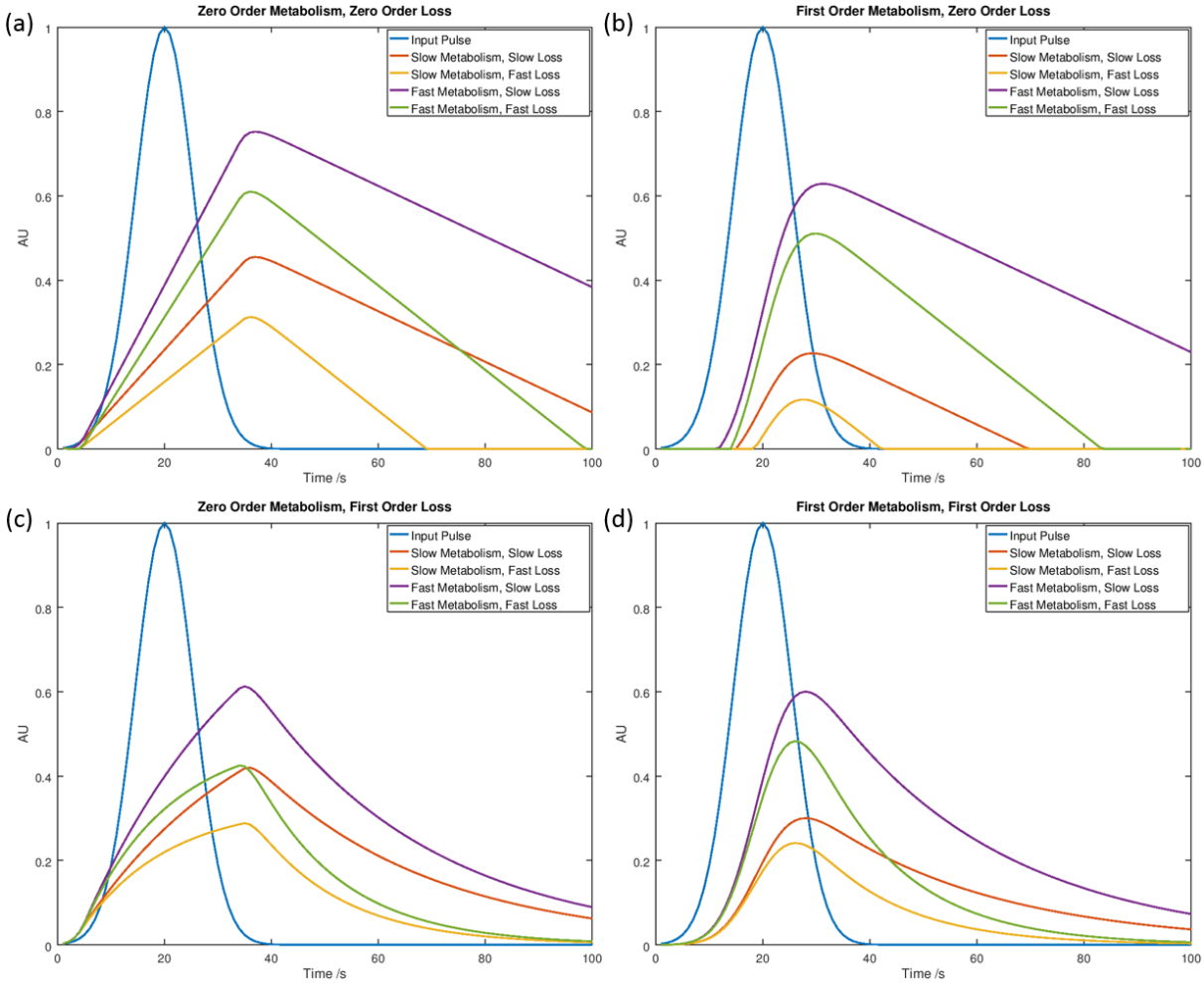

Figure 5.1: A Gaussian pulse of blood-analyte concentration and the 'measured' tear-analyte concentration based on four combinations of metabolic and loss profile: (a) 0th order – 0th order, (b) 1st order – 0th order, (c) 0th order – 1st order, (d) 1st order – 1st order. For each example, faster and slower rates are considered for both metabolism and loss.

A simplified formulation of the problem considers a naïve case of 0^{th} or 1^{st} order metabolism directly from blood biomarker to non-invasive biomarker, with no additional time delay. Once the analyte enters the non-invasive medium it is assumed to evaporate or filter out, either at a constant rate or a rate proportional to its concentration (equivalent to a 0^{th} or 1^{st} order metabolic pathway respectively). In this example, an arbitrary input profile – a normal distribution – of blood-analyte is traced through the 0^{th} or 1^{st} order metabolic pathway into the tears, and, by considering its subsequent 0^{th} or 1^{st} order loss-profile, a prediction of the tear-analyte concentration is generated. This process is shown schematically in Figure 5.1; for each example, fast and slow metabolism and loss rates are considered, analogous to four patients with differing physiologies. The first conclusion is

immediately obvious – even in this simple case, it is not possible to measure non-invasive biomarker concentration and expect to accurately reconstruct the underlying blood biomarker concentration without some form of mapping function (this problem is well described in [7]); and, a lag/bias treatment, in which measured data is corrected for both time-delay and magnitude bias, is unlikely to be sufficient – a conclusion supported by analysis of this problem in the literature [105]. It is also clear that a faster or slower metabolism, and faster or slower loss from the non-invasive medium, drastically alters the 'measured' concentration profile. Thus, an attempt to reconstruct the underlying input profile using inaccurate metabolic parameters (perhaps applying data taken from one patient to a different patient) may reach very incorrect conclusions.

However, even this example is vastly simplified. In a real patient, the mathematical mapping of measured non-invasive biomarker concentration to underlying blood biomarker concentration will be far more complex, due to the physiology of each patient's analyte absorption from the blood stream, enzymatic activity, kidney health, or even the architecture of their tear glands; all of these may complicate the mapping from underlying profile to measured data. It therefore seems that the best way to approach the reconstruction of underlying concentration profiles is an empirical process which learns, for each individual, their personal metabolic mapping for the analyte and measurement in question.

Two types of data were used in this study. For the first, glucose data from real patients was obtained from [106]. This is a set of 31 patients, whose ISF glucose was monitored over a 12 hour period using a continuous glucose monitor (CGM). For the purpose of this study, this continuous data was treated as the blood glucose data (for this analysis the ISF glucose has sufficiently similar features to that of blood glucose), and an accepted two-compartment model [7,107] was used to generate paired ISF data (Figure 5.2 a). The two-compartment model is well described in the literature, but it is worth noting here that it is closely related to the 1^{st} order – 1^{st} order case shown in Figure 5.1 d; effectively, the model describes the relationship of the ISF glucose to the blood glucose as an equilibration response, with characteristic time constant τ. Patients generally exhibit a range of time constants characterizing the transfer rate from blood glucose to ISF glucose; for this data, a time constant of τ = 20 mins was chosen (near the maximum of observed rates [7]). Of the 31 patients, 12 with statistically similar mean and maximum

glucose levels were selected (since in this study these 12 patients are treated as the same patient on 12 different days). One of these sets was used for training, one for cross validation (CV), and 10 for test sets.

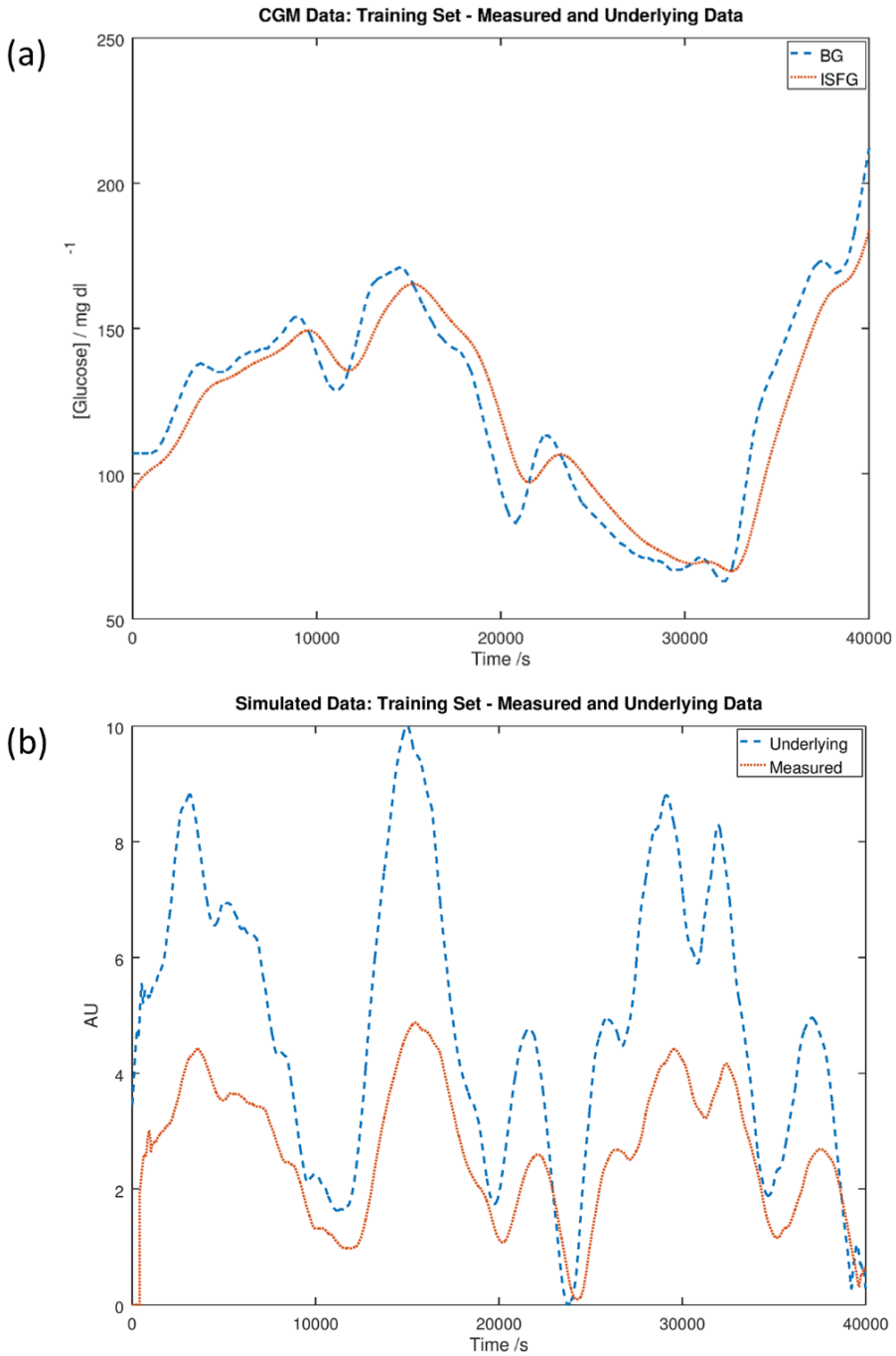

Figure 5.2: CGM and simulated data. (a) CGM glucose data ('BG') with paired ISF glucose data ('ISFG') generated by a two-compartment model. (b) Simulated blood biomarker data ('Underlying') with paired non-invasively measured biomarker data ('Measured').

In CGM monitoring, the Mean Absolute Relative Difference (MARD) is often used to evaluate the disparity between two data sets such as the ISF and blood glucose [105], where

$$MARD = \frac{1}{n}\sum_{i=1}^{n}\frac{|y_{i,blood} - y_{i,ISF}|}{y_{i,blood}}. \quad (5.1)$$

The average MARD in these sets before correction was 6.7%.

Next, to test the neural network method further, data was simulated which was more volatile than the real glucose data, and with a greater relative disparity between the non-invasive and blood biomarker measurements. The underlying (blood) data was constructed using a simple random walk, modified to walk preferentially towards zero

$$y_i := y_{i-1} + rand(-0.7 \rightarrow 0.3), \quad (5.2)$$

with values generated below zero set to zero before the next iteration. A series of coarse and fine smoothing functions were applied, so that the peaks and troughs reflected approximately the expected timescale of a particularly volatile biological marker, changing over the course of minutes. The data was scaled to an arbitrary maximum magnitude of ten simply to reflect the fact that biological data usually does not vary between zero and one.

The metabolic shift was chosen to represent a number of possible mathematical mappings working in concert. These were applied in the following order, starting with underlying data, *U*, and finishing with 'measured' data, M_5:

1. A time delay:

$$M_1(t) = U(t + t_{delay}) \quad (5.3)$$

2. Reduce magnitude by a proportional factor:

$$M_2(t) = f_1 M_1(t) \quad (5.4)$$

3. Reduce magnitude by a square factor:

$$M_3(t) = M_2(t) - f_2 M_2^2(t) \quad (5.5)$$

4. Reduce magnitude by a cube factor:

$$M_4(t) = M_3(t) - f_3 M_3^3(t) \quad (5.6)$$

5. Add a pooling effect, here approximated by addition of an average of the last $t_{pooling}$ seconds:

$$M_5(t) = M_4(t) + f_4\left(\frac{M_4(t-1)+\cdots+M_4(t-t_{pooling})}{t_{pooling}}\right) \quad (5.7)$$

By generating the underlying data in a pseudo-random way, the neural network gains no information from the underlying data – it cannot simply learn the standard patterns, and so must approximate only the metabolic mapping function. This mapping, with appropriately chosen factors, resulted in a 'measured' data set derived from the underlying data in a non-trivial manner (Figure 5.2 b). In these simulated data sets the concentrations were designed to vary near or at zero, which is represented physiologically in some biomarkers. Since MARD is not applicable in cases where data points vary around zero, a slightly adjusted metric was used, Mean Absolute Normalized Difference (MAND),

$$MAND = \frac{1}{n\times\bar{y}_u}\sum_{i=1}^{n}\left|y_{i,u} - y_{i,m}\right| , \quad (5.8)$$

where y_u is the underlying data and y_m is the measured data (or another data set in question). The average MAND in these sets before correction was 46.9%.

A common correction used in cases of measurement disparity such as CGM is lag/bias correction, in which a lag (time delay) and bias (magnitude correction) is estimated and corrected for [105]. A lag/bias correction, in which lag and bias values were estimated via an iterative method for each data set, was applied to both data types, and MARD or MAND values from this correction method were used as a benchmark from which to compare the neural network method's performance. Examples of the lag/bias corrected data is shown in Figure 5.3, and more information can be found in Appendix 12.1.

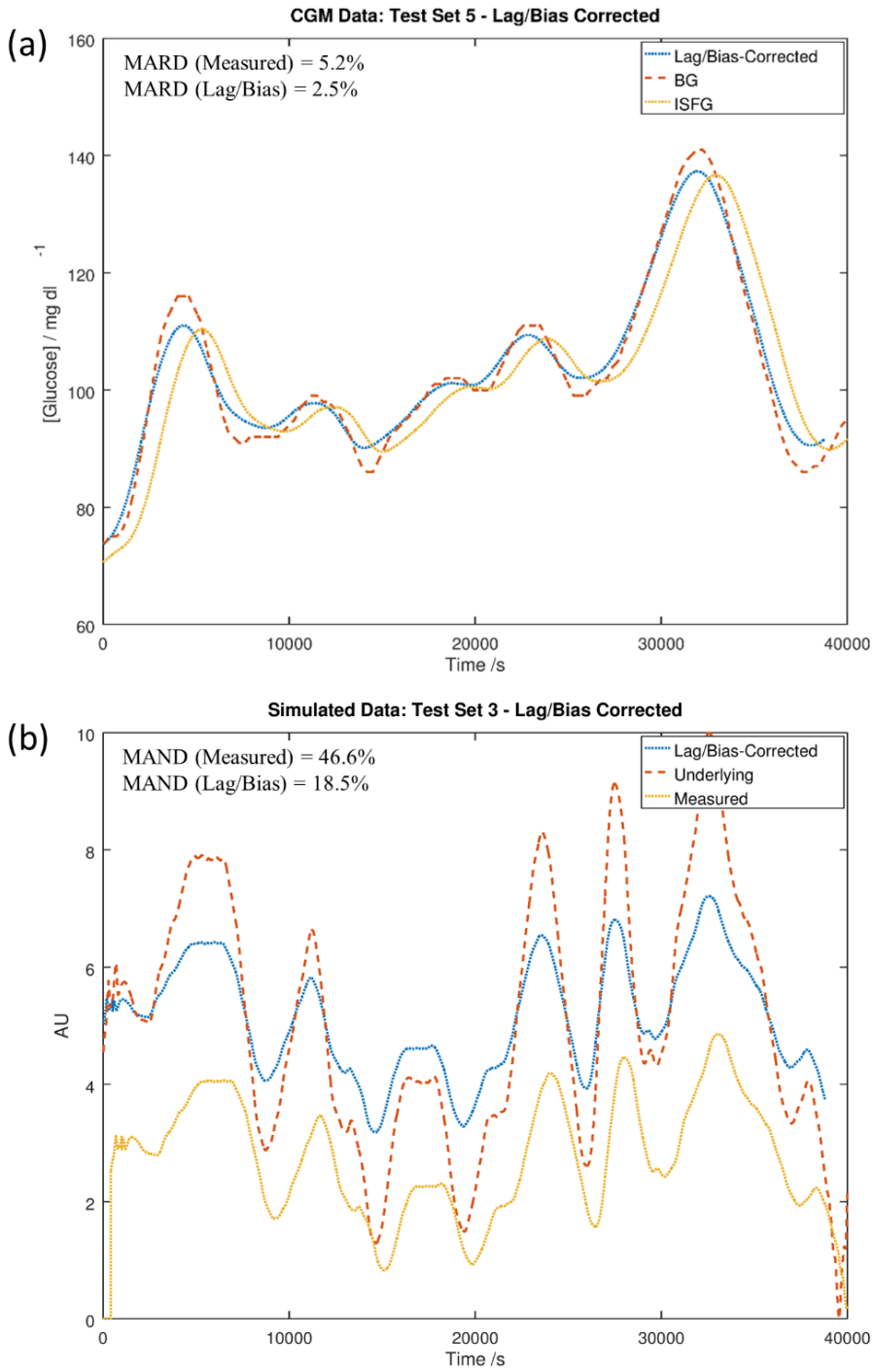

Figure 5.3: Lag/bias correction in CGM and simulated data sets. (a) CGM Test Set 5 illustrating blood glucose ('BG'), ISF glucose ('ISFG') and a lag/bias correction. (b) Simulated Test Set 3 illustrating simulated blood biomarker data ('Underlying') with paired non-invasively measured biomarker data ('Measured') and a lag/bias correction. Other lag/bias corrected sets found in Appendix 12.1.

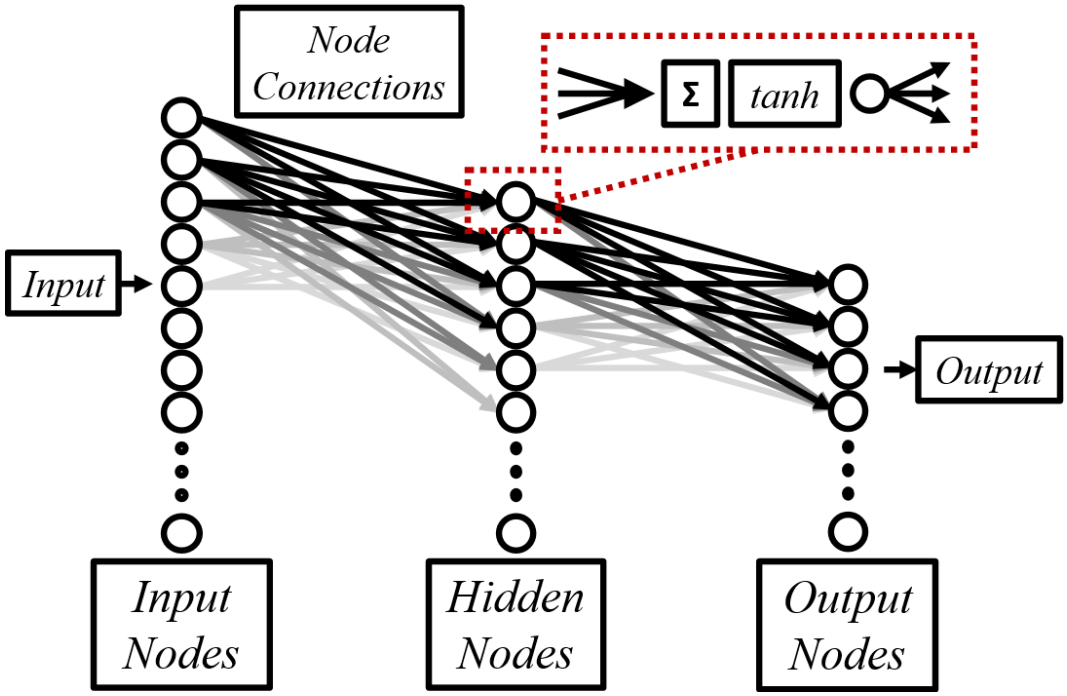

Figure 5.4: Schematic representation of the neural network, illustrating the three-layer nodal structure, the interconnections, and the hyperbolic tangent activation function used in the hidden layer.

A simple neural network was created with 300 input nodes, 30 output nodes, and a hidden layer of 165 nodes (the arithmetic mean of the input and output) (Figure 5.4). Input and hidden layers were also given a bias node. Hyperbolic tangent activation functions were used for the hidden layer; in a 'vanilla' neural network sigmoid functions are used, but in this case they had a tendency not to fit the mapping well without the ability to vary below zero. The data was split into windows of length 3,000 seconds (50 minutes); windows were created at 5 second intervals through the data. This window size was chosen in order to strike a balance between two factors: there must be sufficient data within the window for the neural network to learn the mapping, but the larger the window, the longer the initial measurement time before the network can begin predicting the underlying data. In addition, the window technique breaks up the natural patterns which might occur in real physiological data; this encourages the network to learn the mapping, not the patterns, which could otherwise lead to incorrect predictions in the case of a disruption to the underlying physiological process. The window separation of 5 seconds was simply chosen to manage data quantity. The input to the neural network, for each window, was the 3,000 seconds of 'measured' data, averaged in batches of 10 to give 300 data points, while the output of 30 neurons was compared

to 3,000 seconds of underlying data, averaged in batches of 100 to create 30 data points. This comparison yielded a cost function representing a measure of how well the network performed in predicting the true underlying data,

$$Cost = \frac{1}{m}\sum_{k=1}^{n}\sum_{l=1}^{m}(a_3^{k,l} - y^{k,l})^2 + \frac{\lambda}{2m}\left(\sum_{i=1}^{I}\sum_{j=1}^{h}\theta_1^{i,j} + \sum_{j=1}^{h}\sum_{k=1}^{n}\theta_2^{j,k}\right), \qquad (5.9)$$

where indices i, j, k and l correspond to input, hidden and output layer, and training examples respectively, *m* is the number of training examples, *I* is the number of input neurons, *h* the number in the hidden layer, *n* the number in the output layer, a_3 is the set of neuron values in the output layer, *y* is the underlying data against which the prediction is compared, θ are the weights between neurons and λ is the regularization function. Regularization in the form of ridge regression of the weight values (θ) was used to avoid overfitting the training set. The regularization parameter λ was determined by training the neural network with a range of λ values ($\lambda = 0, 10^{-4}, 10^{-3}, \ldots, 10^{3}$) and analysing training and CV cost for each value of λ to find the minimum.

Each individual window (nearly 8000 in total) was treated as a separate training example. Training of the neural network was enacted using a backpropagation algorithm, in which the network's output is compared to each training example, derived from the supervisory (underlying) data, and the difference at each output node is evaluated and used to compute a small change to each weight value within the network. This process is carried out iteratively until the inter-iteration variation approaches zero. Once the neural network is trained, this mapping would be carried out continuously throughout the day; every five seconds (in this case), the last 50 minutes of data may be fed into the trained neural network to update its reconstruction of the underlying data. This method also allowed a significant number of training examples to be created from only one day of data.

A basic regularized linear regression function was used to minimize the cost function, and backpropagation was used to train the neural network, yielding gradients Δ_1 and Δ_2 for weights θ_1 and θ_2 respectively, where

$$\Delta_1^{ij} = \frac{1}{m}\sum_{l=1}^{m}\left(\sum_{k=1}^{n}\left(\theta_2^{jk}\left(a_3^{kl} - y^{kl}\right)\right)\cdot\left(1 - tanh\left(a_2^{jl}\right)\right)^2 a_1^{il}\right) + \frac{\lambda}{m}\theta_1^{ij}, \qquad (5.10)$$

and

$$\Delta_2^{jk} = \frac{1}{m}\sum_{l=1}^{m}\left(\left(a_3^{kl} - y^{kl}\right)a_2^{jl}\right) + \frac{\lambda}{m}\theta_2^{jk}, \qquad (5.11)$$

with symbols defined as before. These gradients were used to update the weights after each training iteration, using a learning rate α.

The CGM data set was trained for 3,000 iterations with hyperparameters of: learning rate $\alpha = 0.02$, regularization $\lambda = 10^{-3}$. The simulated data set was trained for 3,000 iterations with hyperparameters of: learning rate $\alpha = 0.03$, regularization $\lambda = 10^{-2}$. All code was written in the GNU Octave programming environment, version 4.2.1; statistical methods such as ANOVA were performed in Microsoft Excel 2013.

5.2 Results and Discussion

Table 5.1: CGM data, mean absolute relative difference in measured, lag/bias corrected, and neural network corrected cases. Colour scale from red to green indicates high and low values within this table.

**Tests 5 and 7 are illustrated in Figure 5.6.*

CGM Data	MARD (Measurement)	MARD (Lag/Bias)	MARD (Neural Network)
Training	8.4%	5.0%	2.4%
CV	6.7%	3.0%	2.6%
Test 1	4.6%	7.0%	4.0%
Test 2	5.9%	5.9%	2.2%
Test 3	9.1%	3.9%	2.5%
Test 4	8.1%	4.9%	2.8%
Test 5*	5.2%	2.5%	1.2%
Test 6	7.9%	5.5%	5.5%
Test 7*	4.2%	2.3%	1.4%
Test 8	5.4%	2.8%	2.0%
Test 9	7.6%	3.2%	2.6%
Test 10	7.7%	6.3%	4.8%
Average	**6.7%**	**4.4%**	**2.8%**

For both CGM and simulated data, the neural network was trained as described in Section 5.1. The trained neural network was then applied to a series of test sets, and given only the 'ISF Glucose' or 'Measured' data respectively. It generated (for each window) an output which attempted to reconstruct the 'Blood Glucose' or 'Underlying' data. The individual windows were used to rebuild the entire day of data, to better analyze the results. MARD or MAND scores were calculated in order to characterize the performance of the neural network reconstruction in comparison to a lag/bias method, and the original measurement (Tables 4.1 and 4.2).

Table 5.2: Simulated data, mean absolute normalised difference in measured, lag/bias corrected, and neural network corrected cases. Colour scale from red to green indicates high and low values within this table.

**Tests 2 and 3 are illustrated in Figure 5.7.*

Simulated Data	MAND (Measurement)	MAND (Lag/Bias)	MAND (Neural Network)
Training	47.2%	21.6%	3.9%
CV	46.0%	20.0%	5.7%
Test 1	47.1%	26.5%	5.3%
Test 2*	48.0%	17.4%	4.0%
Test 3*	46.6%	18.5%	3.8%
Test 4	46.3%	21.5%	6.2%
Test 5	47.1%	23.1%	4.7%
Average	**46.9%**	**21.2%**	**4.8%**

The neural network method significantly improved on the measurement in the CGM data (MARD improved from 6.7% to 2.8%; using ANOVA analysis to investigate significance of difference of means, $p = 1.6\times10^{-6}$) and the simulated data (MAND improved from 46.9% to 4.8%; $p = 1.1\times10^{-18}$). In both cases, the neural network method also significantly outperformed the lag/bias correction (CGM: MARD improved from 4.4% to 2.8%; $p = 1.8\times10^{-2}$; simulated: MAND improved from 21.2% to 4.8%; $p = 1.1\times10^{-8}$). International standards provide guidelines on measurement fidelity: e.g. in glucose monitoring, ISO 15197 calls for 95% of measurements to fall within 20% of measured glucose value (if value > 75 mg dl^{-1}) or within 15 mg dl^{-1} (if value < 75 mg dl^{-1}), although, typically, modern devices improve on this standard.

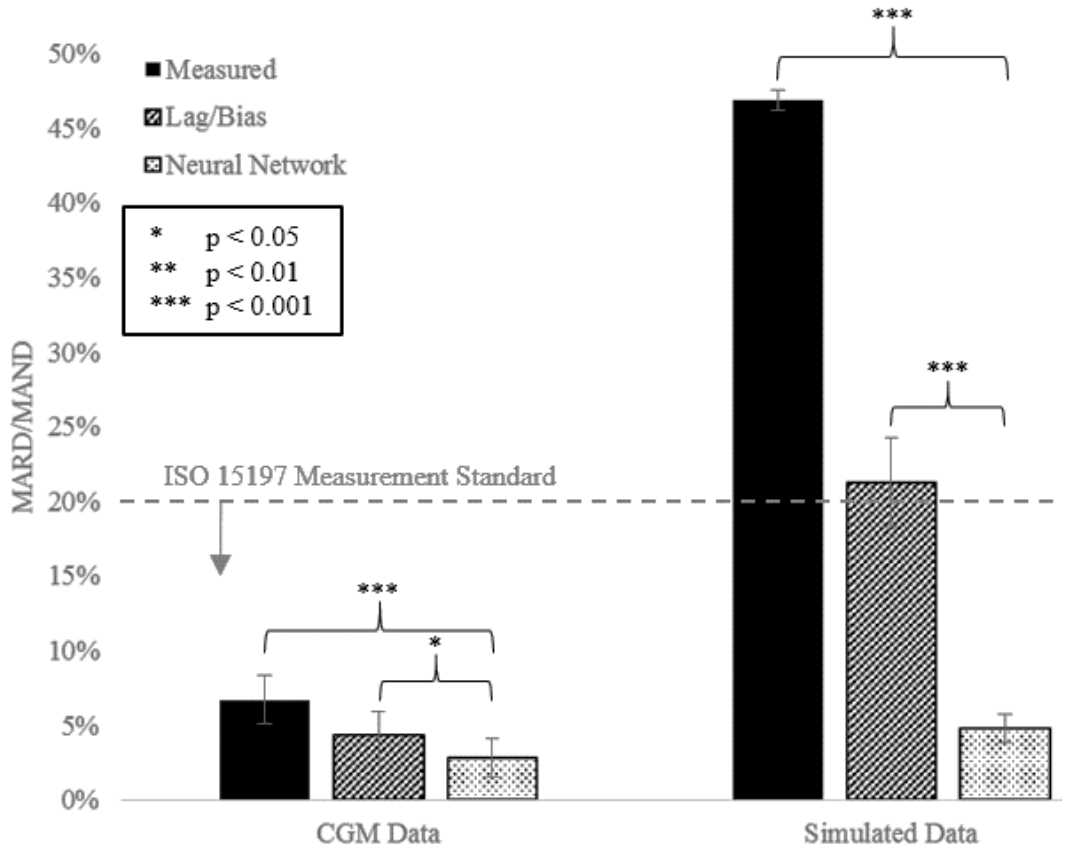

Figure 5.5: MARD/MAND values for CGM and simulated data sets. Significances of difference between measured and neural network corrected sets, and lag/bias and neural network corrected sets, are indicated.

Both of the data sets investigated here achieved accuracies well within this value, and, significantly, in the simulated data the neural network correction greatly improved measurement fidelity from outwith the standard to well within, while the lag/bias correction did not achieve the standard (Figure 5.5).

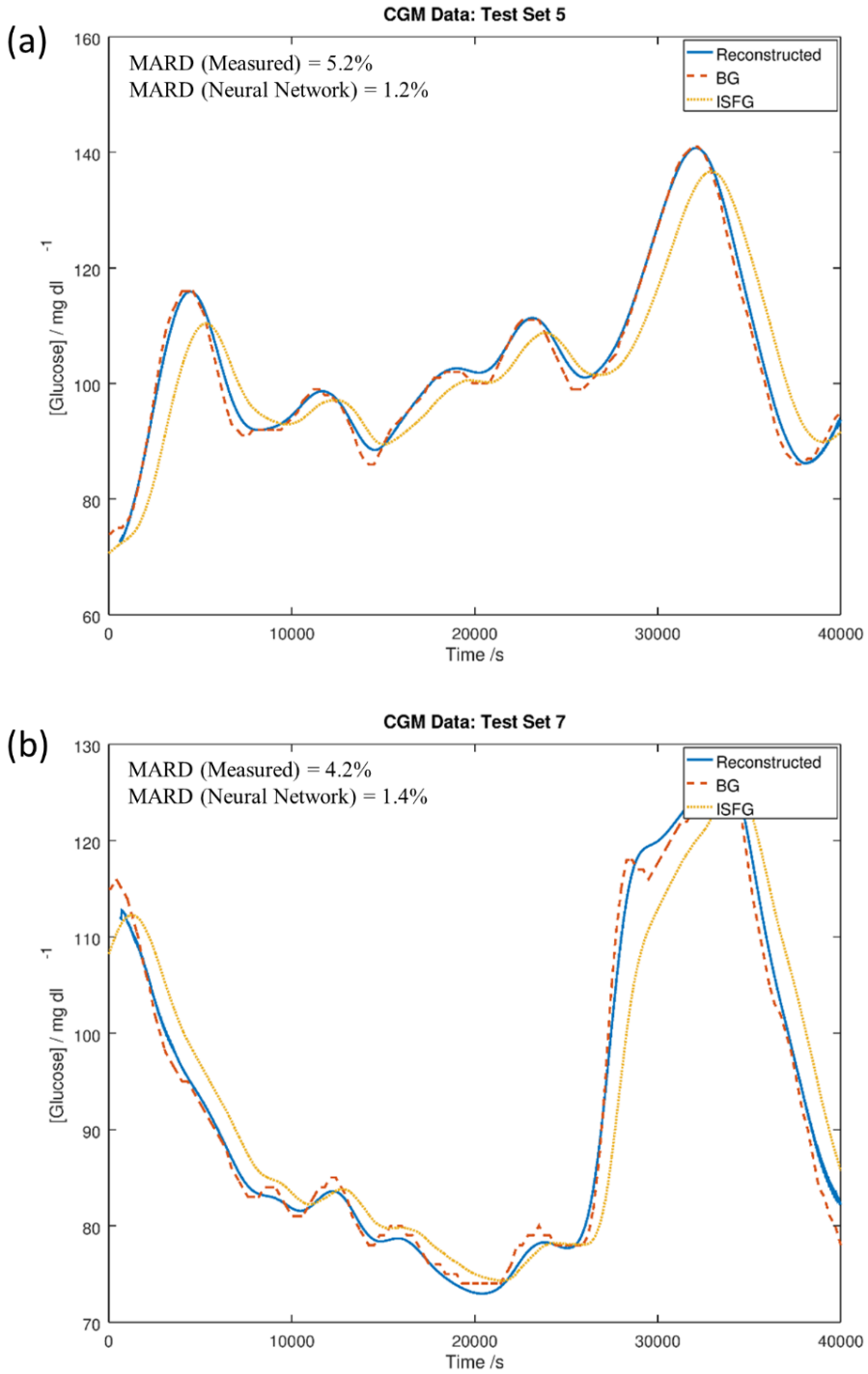

Figure 5.6: Neural network corrections for CGM data set. (a) CGM Test Set 5 illustrating blood glucose ('BG'), ISF glucose ('ISFG') and the reconstruction from the trained neural network; (b) CGM Test Set 7. Other test sets found in Appendix 12.2.

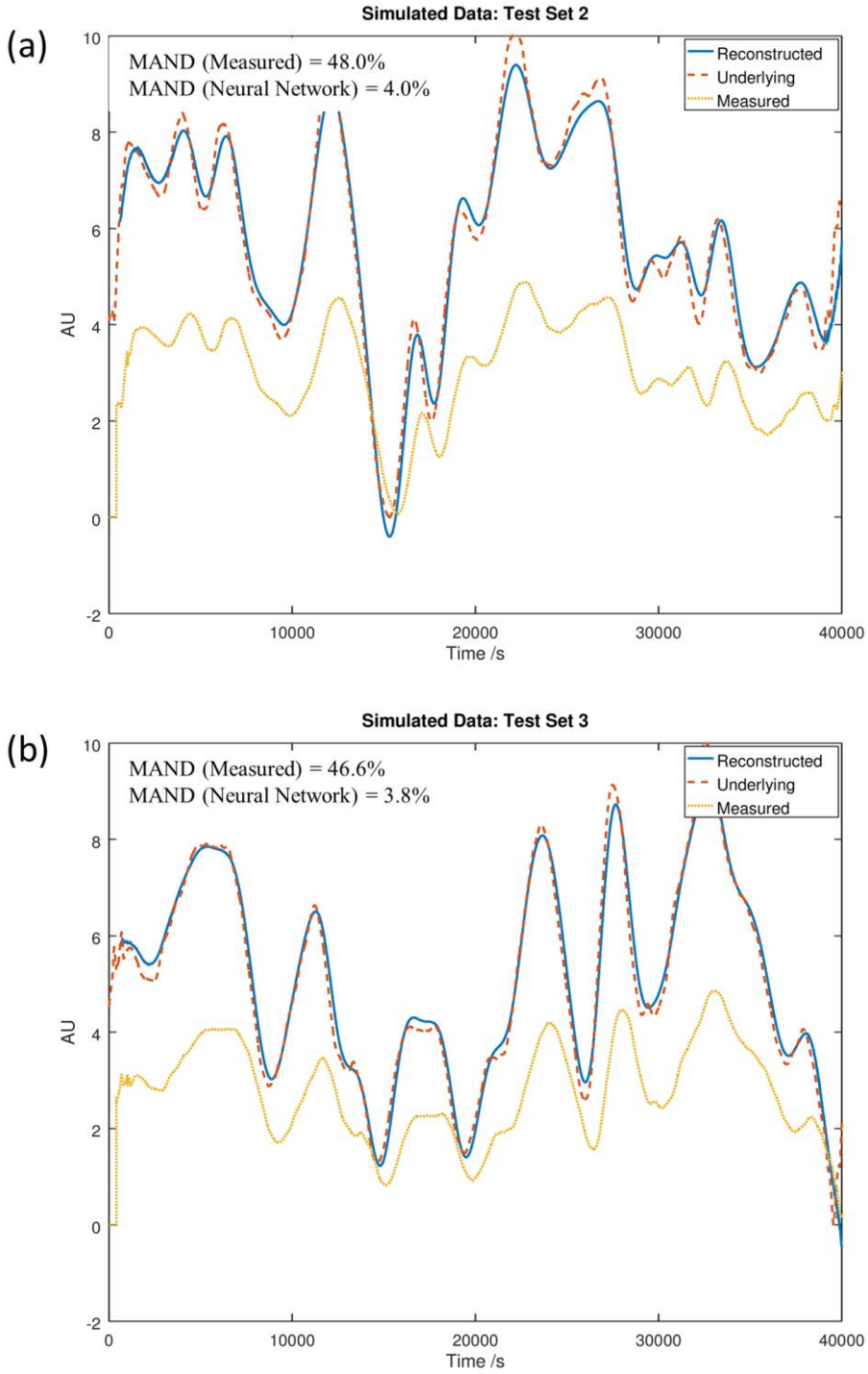

Figure 5.7: Neural network corrections for simulated data set. (a) Simulated Test Set 2 illustrating simulated blood biomarker data ('Underlying') with paired non-invasively measured biomarker data ('Measured') and the reconstruction from the trained neural network; (b) Simulated Test Set 2. Other test sets found in Appendix 12.2.

In general, smoother varying features were well reconstructed by the neural network method (e.g. Figure 5.6 a, t = 30,000 to 40,000). Features in the underlying data

which exhibited sudden discontinuity or volatility were not so well reconstructed (e.g. Figure 5.6 b, t = 30,000). In particular, the sharper peaks and troughs exhibited in the simulated data (e.g. Figure 5.7 a, t = 20,000 to 35,000) were not always followed by the reconstruction. This is due at least in part to the architecture of this particular neural network, since a small error is usually incurred due to the simplification of the output data, and again from the averaging functions during rebuilding of the data set. A larger network – in particular, more output neurons – would avoid these errors, at an increased computational cost.

It is notable that the neural network method has increasing utility with increasing difference between measurement and underlying data, particularly in comparison to the lag/bias correction method. Although non-invasive medical devices of this class are still largely in the research stage, it will be of great importance to have available a measurement correction method which is able to encompass the additional complexity of larger shifts than have been observed in CGM, both in clinical use and at the research level. Understanding the data handling methods in advance can inform device and experimental design, raising or answering questions about patient use protocols and target (and redundant increases in) sensor performance. For example, this correction method was achieved with only 12 hours of supervised training, a reasonable set-up time for a patient, and the training time may be further reduced by ‘priming’ the neural network with initial neuron parameters, or pre-training on a previous patient’s data, such that only fine-tuning is required. However, further investigation is required into the effects of covariate factors, such as the increase in cortisol observed with an increase in blood glucose [108]. Devices with multimodal sensing capability can obtain information about multiple biomarkers at once [49], and this data may be incorporated into an updated version of this neural network method. In the case of covariate factors, it may be necessary to develop a training protocol which accounts for the various features, e.g. including a high-glucose meal during training.

In medical devices with even a small discrepancy between the measured and underlying data, measurement distortion causes significant problems. For example, minimally-invasive glucose sensing requires correction via mathematical modelling, which is not always accurate or patient-specific – studies call for frequent voluntary calibration using fingerprick measurements [105], reducing the benefit of a minimally-invasive method. Now, minimally- and non-invasive devices are

increasingly the subject of research, or moving towards clinical use, with most non-invasive devices (analyzing tears or other non-invasive media) likely to exhibit an even greater degree of measurement distortion than that found in ISF. The neural network tool described in this study is potentially able to learn an individual patient's particular measurement distortion, without prior understanding of the form of this distortion, and subsequently correct for the difference in real time to give a reconstruction of the underlying data.

5.3 Conclusion

Reconstructing blood biomarker profiles from measurements taken in the tear film (or other non-invasive media) is a key part of obtaining data in an ESCL with real clinical utility. The problem is made difficult by the complexity of the difference between the measured data and the underlying data, resulting from the complexity and variability of physiological processes underlying the transport of analyte into the lachrymal fluid, and by the individuality of each patient's physiology. In this chapter, a method based on a neural network was demonstrated which can learn the correction required in a particular patient, potentially after only one day of supervised training, and subsequently reproduce the underlying blood biomarker profile with fidelity well within ISO requirements for glucose monitoring. The benefits of using a neural network method include the generic nature of the approach; i.e. it is not necessary to specify the type of biomarker being measured, or the method of non-invasive measurement. This method is therefore applicable to ESCL measurements and other non-invasive devices such as smart tattoos performing continuous measurement on the skin.

There is currently no method described in the literature which accounts for the problem of measurement distortion in ESCLs. It was therefore of great importance to explore solutions to the problem, in order to confirm the potential utility of an ESCL in the first place, and to inform the design of a next-generation ESCL. From this study it is clear that measurement distortion may be corrected for using a neural network method, and that, in combination with the spatiotemporal method described in Chapter 3, ESCLs may be used to produce electrochemical measurements of real clinical utility.

6 Spatiotemporal Electrochemical Sensing in a Smart Contact Lens

An ESCL device was designed, following the findings in Chapters 2-4, and incorporating (or using updated versions of) techniques from each. From Chapter 3, the fabrication method of the core gold/polyimide device was employed in the first stage of this device, with minor modifications in some of the cleanroom techniques. Parasitic capacitance, induction and resistance from the long meandering gold wires were found to be detrimental to the electrochemical signal, increasing signal-to-noise ratio (SNR), so shorter, straight wires were used in the new design in order to reduce these effects. Similarly, in Chapter 4 the use of a connected array of micro- or nanoelectrodes led to a better signal than the single microelectrodes found in Chapter 3; thus, connected arrays of microelectrodes were designed in order to draw more current and improve SNR. In Chapter 5, the algorithm described required continuous time-series concentration data, informing the measurement technique used for the ESCL device. It was also conjectured that, with more information about the introduction, progress and drainage of the tear fluid in the eye, the correction algorithm would be better able to reconstruct the underlying concentration found in the blood. Thus, working electrodes were placed in each quadrant of the eye to help monitor the tear flow relative to the lachrymal glands and the lachrymal puncta.

In this chapter the design and fabrication of the ESCL device is described, with further discussion on the challenges facing safe clinical use, and some potential solutions to these challenges. The sensing performance of the device is characterised, and an updated version of the fast-switching chronoamperometric method is described. Using this technique, spatiotemporal electrochemical sensing is demonstrated in various environments including a model eye, in which flow of a high-concentration fluid entering the model eye, flowing across the surface, and draining out, is monitored at real-speed.

This chapter presents work some of which has been published in peer-reviewed articles [16].

6.1 Design

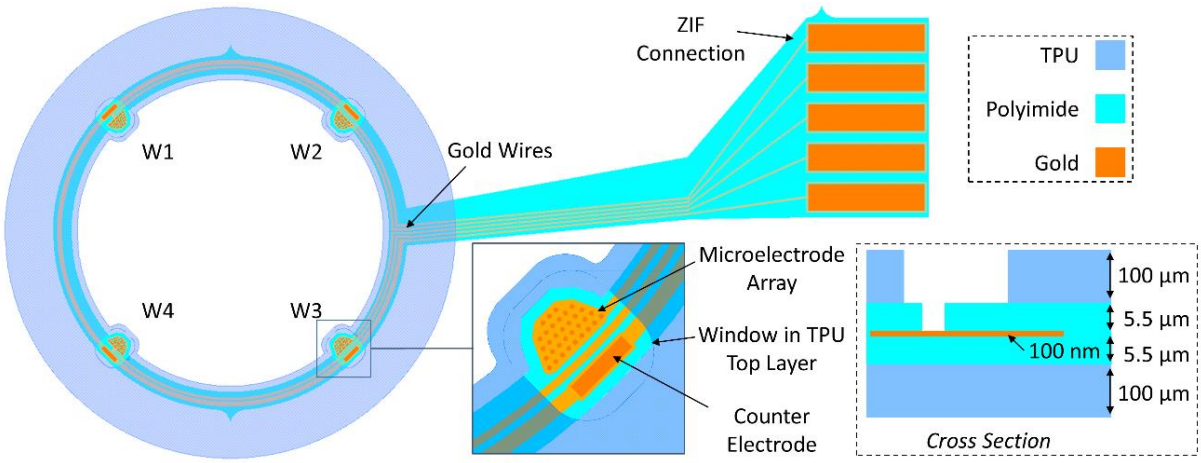

Figure 6.1: Schematic showing key aspects of the design of the ESCL device.

This ESCL (Figure 6.1) consists of a core device – comprising a layer of gold (100 nm in thickness, with a 50 nm titanium-tungsten adhesion layer), sandwiched between two layers of polyimide (each 5.5 µm in thickness) – which is encapsulated in two layers of TPU (each 100 µm in thickness), and moulded to a spherical cap shape (radius of curvature 9 mm). Gold wires connect the four working electrodes and the counter electrode to a ZIF (zero insertion force) connector. Each working electrode is comprised of a connected array of microelectrodes (Figure 6.1, inset).

In this study the device was placed on a hydrogel contact lens to illustrate intended use (Figure 6.2 a); further work would be required to develop processes for complete integration into a soft hydrogel platform. The device is flexible and robust to folding (Figure 6.2 b), returning to its original shape after repeated mechanical deformation.

The ESCL consists of a set of four individually addressable microelectrode arrays, with one placed in each quadrant of the device (Figure 6.1, Figure 6.2 c). Each is situated next to one of four counter electrodes (Figure 6.2 d), which share a single electrical connection. (An external reference electrode was used in this study.) Each microelectrode array comprises 33 microdisc electrodes of 30 µm diameter, spaced at 30 µm in the planar orthogonal directions, in an offset grid of a custom shape (Figure 6.2 d). The shape of the microelectrode arrays was chosen to optimise spatial efficiency and reduce deviation from the design area.

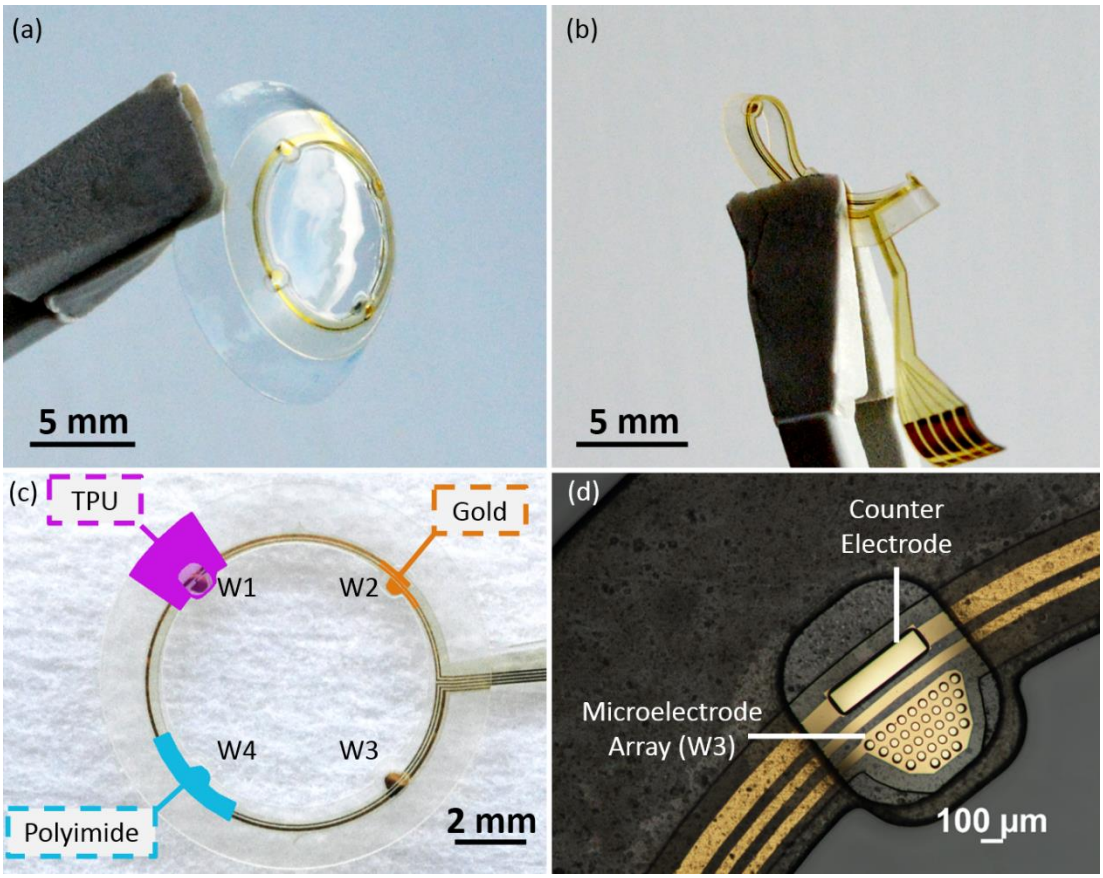

Figure 6.2: Images of the ESCL device. (a) Photograph of the ESCL device illustrating placement on a contact lens; (b) photograph of the ESCL undergoing mechanical deformation using tweezers. (c) Photograph of an unmoulded ESCL, illustrating material regions. Working electrodes 1-4 are indicated by W1-4; (d) photo micrograph of working electrode 3 (W3).

The close proximity of the microdisc electrodes within each array is such that, at longer time scales of continuous current flow, the individual diffusion fields overlap and reduce the sensing performance of the system (i.e. after diffusion field overlap the sensor performs akin to a larger electrode comprising the entire area of the array). An estimate of this time scale can be made using Fick's law, with overlap time t_{ov} occurring at approximately

$$t_{ov} = \frac{{L_{diff}}^2}{2D}, \qquad (6.1)$$

Where L_{diff} is the characteristic size of the diffusion field and D is the diffusion coefficient of the redox species (here ferrocenemethanol is used, with a value of $D = 5\times10^{-10}$ m^2 s^{-1} [47]. (For a physiological comparison, cortisol has a diffusion coefficient of $D_{cortisol} \approx 2.9\times10^{-10}$ m^2 s^{-1} [109]). Using $L_{diff} = 15$ µm, a value of $t_{ov} \approx 225$ ms is found. The fast-switching chronoamperometric technique used in this

study addresses each working electrode for less than 50 ms at a time. Thus, the microdisc spacing is sufficient to achieve microelectrode-like sensing characteristics during intended use.

Previous work has shown that serpentine connections reduces buckling behaviour in the substrate after thermoforming [19,93]; however, since these were only necessary in the radial direction, the design area was restricted to a narrow ring in the circumferential direction of the lens. Earlier work (described in Chapter 3) also highlighted the necessity of reducing parasitic capacitance, inductance and resistance in an ESCL device [49]; using non-meandering connections to the electrode sites, these effects were significantly reduced. Straight connections were also more spatially efficient, and therefore reduced the physical footprint of the device – this reduction is likely to improve comfort during normal use.

In practice, oxygen permeability is a key factor in contact lens comfort and safety. Modern contact lens materials are highly oxygen-permeable [32], and, unlike many reported ESCL prototypes, the ring-shaped design of this ESCL leaves the majority of the lens area free from non-oxygen-permeable materials, allowing sufficient oxygen transfer to the eye for safe extended use.

In this study a ZIF connector was used to provide and electrical interface to the device; placement of a thinned silicon chip has been described in previous work [19,28,62], and this ESCL is intended to incorporate wireless function once sensing protocols have been established. Using an antenna to harvest power inductively [62], power transfer of greater than 100 µW has been demonstrated [23], and new flexible battery technologies developed for smart contact lenses also lead to stringent power requirements [33]. Thus, a balance was required in designing the microelectrode arrays: increased current reduces the required sensitivity of the potentiostat system, and can lead to a more robust and compact chip design, and increase the signal to noise ratio. However, higher current leads to increased power requirements. Using previous results as a guide (Chapter 3), it was calculated that the fast-switching chronoamperometry sensing protocol drew an average of approximately 1 µA, including parasitic circuit effects (but not including sensor-driving electronics). At 0.4 V, this leads to an estimated power consumption of approx. 13.5 µW with 33 arrayed microdisc electrodes – that is, similar to the power transfer to the active element demonstrated by Pandey *et al* [23] (where the power consumption of the remaining architecture accounted for approximately 100 µW).

However, the design of the gold wires in the ESCL device significantly reduced these parasitic effects, and in fast-switching chronoamperometry the microelectrode arrays draw only approx. 40 nW (Section 6.4). Therefore, the new system falls very comfortably within the power requirements of current SCL platforms.

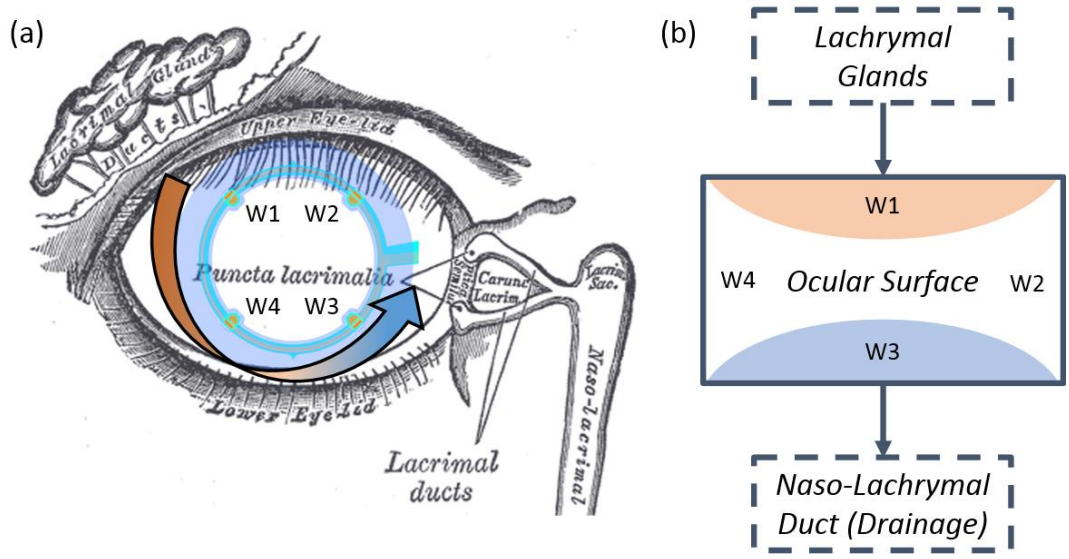

Figure 6.3: Illustration of fluid flow in the eye. (a) Illustration of the anatomy of the eye, and the placement of the ESCL on the corneal surface. The arrow indicates overall flow of tear film from source to drain. Some parts of this figure reproduced from Gray's Anatomy, Plate 896; (b) schematic illustration of a three-compartment model of lachrymal fluid introduction, progress and drainage.

Placement of the electrodes in each of the four quadrants of the ESCL was chosen to investigate the flow of chemical markers across the cornea, with reference to the position of the tear film source (the lachrymal ducts) and drain (the lachrymal puncta) (Figure 6.3 a). With spatially distributed sensing, more information about the introduction, progress and drainage of chemical markers in the lachrymal fluid may be gathered. For example, W1 might measure an increased concentration in new lachrymal fluid as it enters the eye; W4 and W2 provide information on the bulk tear fluid (i.e. within the lachrymal lake); and W3 provides information on the concentration at the point of drainage. Using these data and an appropriate three-compartment model, as shown schematically in Figure 6.3 b, an estimation can be made of the current concentration level in the lachrymal glands, giving the earliest possible indication of changes of the concentration in the rest of the body (particularly in blood). Earlier ESCL prototypes have struggled to measure markers (such as glucose) with sufficient fidelity and speed to make useful estimations of

current blood glucose levels [58]; using this spatiotemporal method, it may be possible to improve measurement fidelity sufficiently to make accurate diagnostic conclusions, and even early-warning health monitoring systems, using an ESCL.

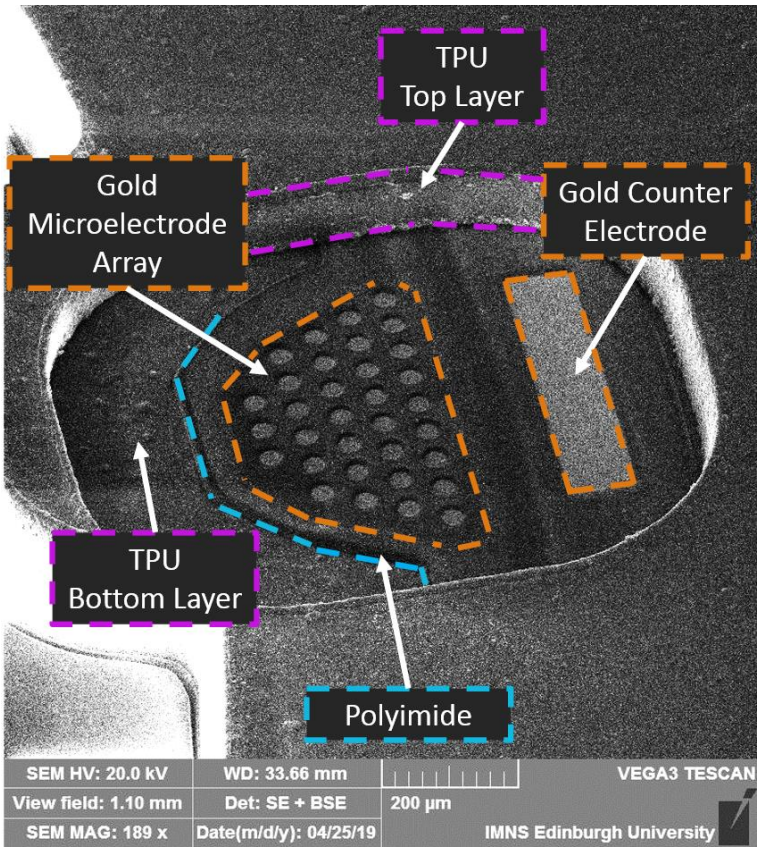

Figure 6.4: Scanning electron micrograph of a working electrode site.

Previous ESCL designs have not explicitly reported on the question of efficient tear film contact with the electrochemical sensors, generally assuming instead a bulk fluid scenario. However, integration of a device such as this into a contact lens likely entails encapsulation in hydrogel or a similar material. In addition, it is currently unclear whether the best position for the sensors is out- or in-facing. The current model of the tear film describes a bi-layer structure, with a thin superficial lipid layer and an aqueous/mucin gel layer with decreasing mucin content from the corneal surface to the lipid layer [51], and it is not currently understood exactly how the addition of a contact lens affects this structure. It is possible that different analytes may variously be better represented on either the out- or in-facing side of the lens, depending on their representation in each fluid environment (i.e. aqueous, mucosal or lipid), and therefore two classes of ESCL or a combined lens may be necessary. Corneal irritation must be considered in the in-facing case. In this ESCL, the sensing

sites are recessed 100 µm into the TPU surface (Figure 6.4), which is greater than the estimated depth of the tear film (40 µm [110]), and it is not yet known whether this architecture would cause irritation or discomfort if placed in direct contact with the ocular surface. In this study both in- and out-facing lenses were moulded, and no difference in performance was observed. The out-facing lenses were estimated to be more suited to the ocular environment, and this architecture is also less likely to cause irritation in the eye. However, in-facing sensors may experience less interference from environmental effects such as rain and humidity. A more in-depth investigation into this question may be useful on the route to clinical use, though it is outside the scope of this particular thesis.

6.2 Fabrication

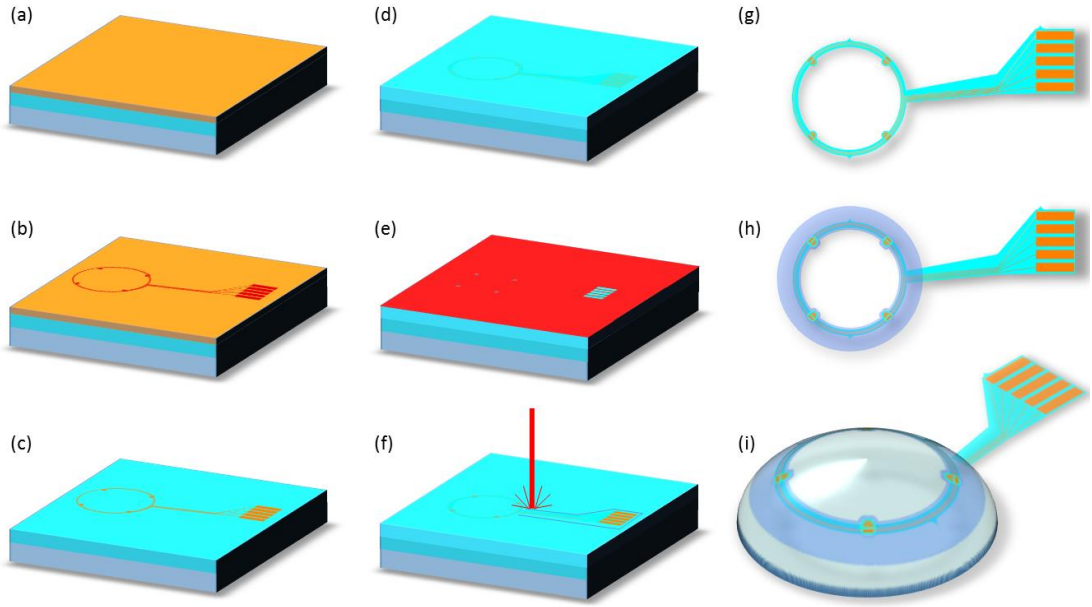

Figure 6.5: Diagrammatic representation of fabrication steps. (a) Polyimide and TiW/Au layers on a glass wafer; (b) S1818 resist patterned to define metal layers; (c) metal layers defined by wet etching and stripping of photoresist; (d) polyimide layer spin-coated over metal layers; (e) thick photoresist (AZ4562) patterned to define contact pads and electrode sites; (f) after reactive ion etch and stripping of photoresist, a picosecond laser is used to cut out the device; (g) device released from glass wafer; (h) pre-patterned thermoplastic polyurethane bonded on either side of the device, and device cut to shape using a picosecond laser; (i) device thermoformed to a spherical cap shape and added to hydrogel contact lens.

The device fabrication process is illustrated in Figure 6.5 and described below. The glass wafer was cleaned and treated with a chemical adhesion promoter ((3-Aminopropyl)triethoxysilane, APTES), then a layer of polyimide (5.5 µm thickness,

PI-2611, HD Microsystems) was spin-coated onto the wafer (3000 rpm, 30 s), dried on a hot plate (200 °C, 10 min) and cured in a nitrogen oven (RT to 200 °C at 4 °C min^{-1}; 20 min at 200 °C; ramp to 350 °C at 2.5 °C min^{-1}; 60 min at 350 °C). Photolithography (S1818 photoresist, spin coating at 4000 rpm for 60 s, baking at 90 °C for 2 min, UV irradiance for 85 mJ cm^2, developing for 30 s with developer MF-319/deionized water (DI H_2O) at 1:1 ratio) was used to cover the central working area of the mask, while reactive ion etching (RIE) (1 min, 150 W, 150 mTorr, 15 sccm O_2, 5 sccm CHF_3) was used to roughen the exposed perimeter area of the polyimide before removal of the photoresist (1 min in acetone, 1 min in acetone/isopropyl alcohol at 1:1 ratio, 1 min in DI H_2O). A second layer of polyimide was spin-coated (same parameters as before). The second layer of polyimide adhered strongly to the roughened perimeter area of the first layer of polyimide, but not strongly to the smooth central area. This ensured easier release of the devices (restricted to the central design area) after fabrication, while avoiding delamination of the second polyimide layer during processing.

Metal layers of TiW (50 nm, adhesion layer) and Au (100 nm) were deposited by sputtering. These metal layers were patterned with photolithography (S1818 photoresist) and wet etching. A second layer of polyimide was added as described above. Thick photoresist (AZ4562, target thickness 10 µm) was used as a hard mask to define contact pads and electrode sites, and reactive ion etching (45 min, 22 sccm O_2, 5 sccm N_2, 350 mTorr, 75 W; or using parameters previously described in Chapter 3 and [49]) was used to etch the top layer of polyimide through to the gold layer. The photoresist was stripped and the devices cut out using a picosecond laser (355 nm, 12 ps, 50 kHz, 320 mW). The devices were then released from the glass wafer using thermal release tape. Thermoplastic polyurethane was pre-patterned with the picosecond laser (355 nm, 12 ps, 50 kHz, 400 mW, 10 passes at 40 mm s^{-1}), creating vias at the electrode sites and contact pads. These pre-patterned sheets were bonded to either side of the devices with a custom two-step method using a wafer bonder. The encapsulated devices were once again cut out using the picosecond laser (same parameters as previous step) and moulded into a hemispherical cap shape with thermoforming.

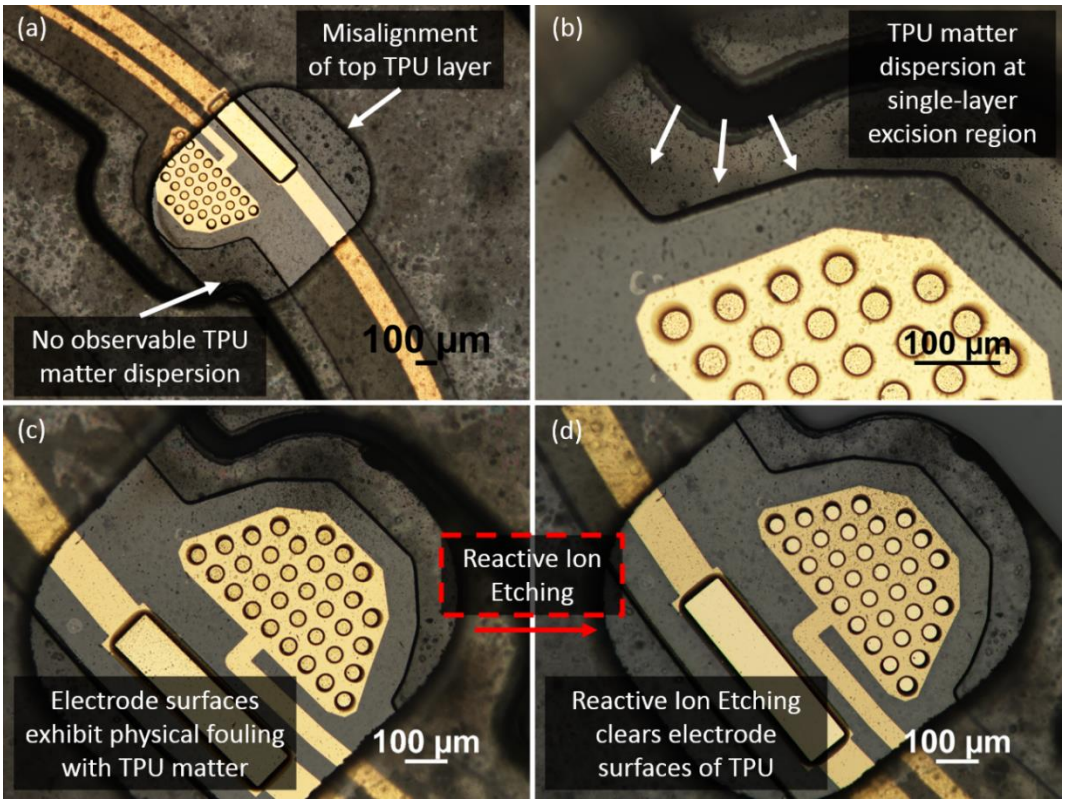

Figure 6.6: Fouling of the electrode surfaces. (a) Photo micrograph of an electrode site with misaligned TPU top layer. (b) Photo micrograph of a misaligned electrode site on a different device, where TPU spray from the laser excision is observed. (c) Photo micrographs showing fouled electrode sites before and (d) after reactive ion etching, a process which cleans the electrode surfaces of deposited TPU matter.

In some devices, the top TPU layer was either partially or catastrophically misaligned (Figure 6.6 a shows an example of a catastrophic misalignment, in which some part of the microelectrode array is covered, while Figure 6.6 b-d shows partial misalignment). In all of these cases, the laser excision of the device, designed to cut through both layers of TPU, usually cuts into the window in which only a single layer of TPU exists. In some cases, this caused no issues (e.g. Figure 6.6 a), while in other cases the laser caused dispersion of the TPU matter away from the excision line, often covering the electrode surfaces (e.g. Figure 6.6 b). Although we did not use devices in which significant physical fouling was observed for electrochemical testing, it is possible that some small quantity of TPU dispersion occurs even when not easily observed, and possibly even without misalignment. Since this would happen to varying degrees at different electrode sites on a single device, the result may be an intra-device variation of electrode performance, which was indeed observed in Figure 6.7 (Section 6.3). Although in the scope of this thesis it was not

necessary to address this effect in more detail, a method was sought to clean the surface in case of future fouling issues; reactive ion etching (5 min, 20 sccm O^2, 150 mTorr, 40 W) was successfully used to remove the residual TPU from the surface of the electrodes (Figure 6.6 c-d).

6.3 Electrochemical Characterisation

For electrochemical measurements, ferrocenemethanol (Aldrich, 97% purity) was prepared in various concentrations in 0.1 M potassium chloride (Aldrich, 99% purity) with deionised water. All devices were electrochemically cleaned in H_2SO_4 with 5 cycles of cyclic voltammetry (0 V – 1.6 V – 0 V). Electrochemical experiments were carried out in a Faraday cage using an Autolab PGSTAT128N potentiostat, using the on-device gold counter electrode and an external Ag/AgCl reference electrode (BASi, USA). Control and data acquisition was performed using Nova 2.0.1.

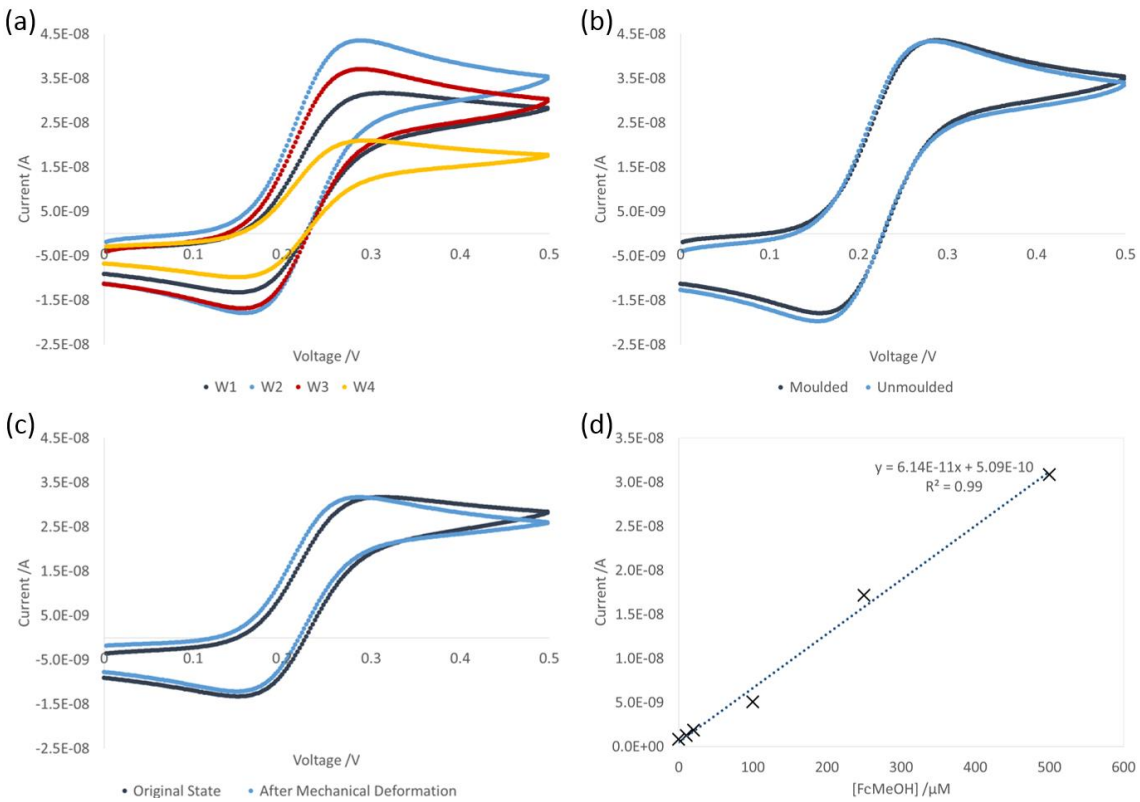

Figure 6.7: Electrochemical characterisation of the microelectrode arrays. (a) Cyclic voltammograms of each working electrode in a single lens; (b) cyclic voltammograms taken before and after moulding; (c) cyclic voltammograms taken before and after repeated mechanical deformation; (d) current response to a range of concentrations of FcMeOH.

Electrochemical characterisation was carried out using standard cyclic voltammetry (0 V – 0.5 V – 0 V, at 0.1 V s^{-1}), in 0.5 mM ferrocenemethanol (FcMeOH) – a redox

reporter which exhibits well-characterised electrochemical behaviour at bare metal electrodes, and is often used to investigate electrochemical systems. The microelectrodes showed expected sensing characteristics in these experiments; however, it is worth noting that these arrays were designed for high-speed sensing protocols (Section 6.1), and therefore diffusion field overlap may result in reduced sensitivity during these standard tests.

Variation in current response between the different electrode sites was observed (Figure 6.7 a). In earlier work, the effect of surface roughness was quantified and discussed ([49], Chapter 3), and the intra-lens variation here is likely due in part to a non-uniform reactive ion etch profile during fabrication (faster etch speeds were observed at the periphery of the wafers than at the centre), which resulted in higher surface roughness in some electrodes. In addition, misalignment of the TPU windows caused physical fouling of the electrode surfaces during the last laser excision stage in some electrode sites, and to varying degrees between electrode sites (Section 6.2), which may also account for the observed variation. This variation is corrected for during normalisation in the high-speed chronoamperometric sensing protocol.

Sensing performance before and after thermoforming was investigated, and no significantly measurable difference was found between the two states (Figure 6.7 b). Similarly, sensing performance was unchanged after repeated mechanical deformations (Figure 6.7 c; ten full folds of the lens, as illustrated in Figure 6.2 b). The position of the metal layer in the neutral mechanical plane reduces stress during mechanical deformation to a minimum and avoids cracking or damage to the wire tracks.

Comparison of these results to an established theoretical model of microdisc electrodes was carried out using the Saito equation (equation 6.2) [95], which calculates limiting current under steady-state conditions:

$$i_L = 4nFDc_0r\,, \tag{6.2}$$

where n is the number of electrons transferred in the reaction, F is the Faraday constant, D is the diffusion coefficient of the redox species (FcMeOH), c_0 is the concentration, and r is the radius of the microdisc. Values of $D = 5\times10^{-10}$ m^2 s^{-1} [47], and $c_0 = 0.5$ mol m^{-3} were used. In addition, theoretical models suggest that the recession of a microdisc electrode of radius 15 µm into the polyimide by 5.5 µm will

result in a reduction in current drawn by 32% [94]; this correction was included in the analysis. A mean limiting current from the four electrodes was found to be 3.01×10^{-8} A, which in this model yields a microdisc radius of 13.8 µm (for an array of 33 microdiscs). This is slightly smaller than the true size, a reduction which may result from physical fouling of some of the electrode surfaces by TPU during the last laser excision stage (Section 6.2).

Cyclic voltammetry was also used to investigate linearity of the current response to a range of concentrations of FcMeOH, from 10 to 500 µM, and a 'blank' measurement of KCl (0.1 M) (Figure 6.7 d). As found in Chapter 3, a linear current response was observed, with $R^2 > 0.99$, indicating a high confidence in the linear fit. Limit of detection (LOD) was calculated following the IUPAC convention [98]:

$$x_L = \bar{x}_{bl} + ks_{bl} \tag{6.3}$$

where x_L is the smallest current that can be reliably detected, $\bar{x}_{bl}$ and s_{bl} are the mean and sample standard deviation respectively of the blank (KCl) measurement, and k is a numerical factor ($k = 3$ was used to ensure a confidence level of > 99%). The LOD is obtained by substituting $x = x_L$ into the calibration function (Figure 6.7 d), yielding the lowest detectable concentration at this confidence level. Despite the close proximity of the microdiscs in the array (Section 6.1), a LOD of 7.8 µM was calculated. This is a twofold improvement on previous results (Chapter 3), most likely due to the increased signal (and therefore higher signal-to-noise ratio) of the microelectrode array.

6.4 Spatiotemporal Electrochemical Sensing

During spatiotemporal sensing a 74HC4051 8-channel analog multiplexer, driven by a microcontroller (Arduino Nano [99]), was used to rapidly switch in sequence through the eight working electrodes (Figure 6.8). Data processing was carried out using algorithms written in the Python programming language.

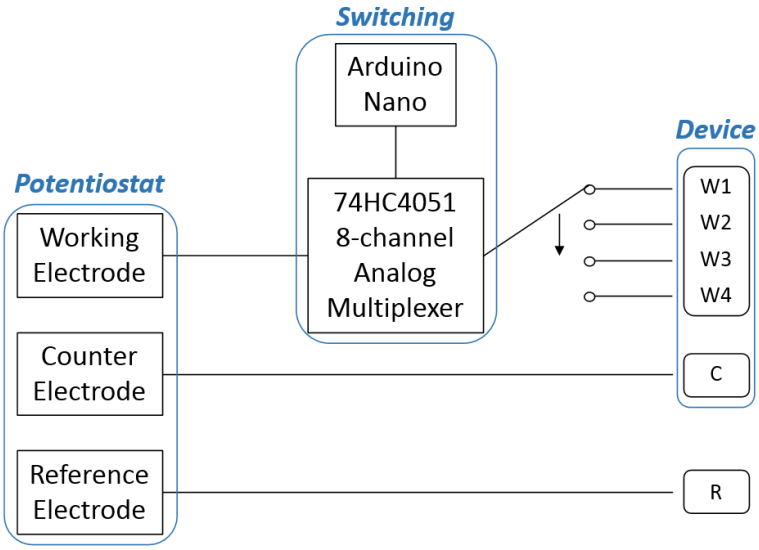

Figure 6.8: Schematic of the circuitry used for spatiotemporal experiments, illustrating the connections of the potentiostat (Autolab PGSTAT128N) to the working electrodes (W1-4), via an analogue multiplexer driven by a microcontroller (Arduino Nano); to the on-device counter electrode (C); and to the external reference electrode (R).

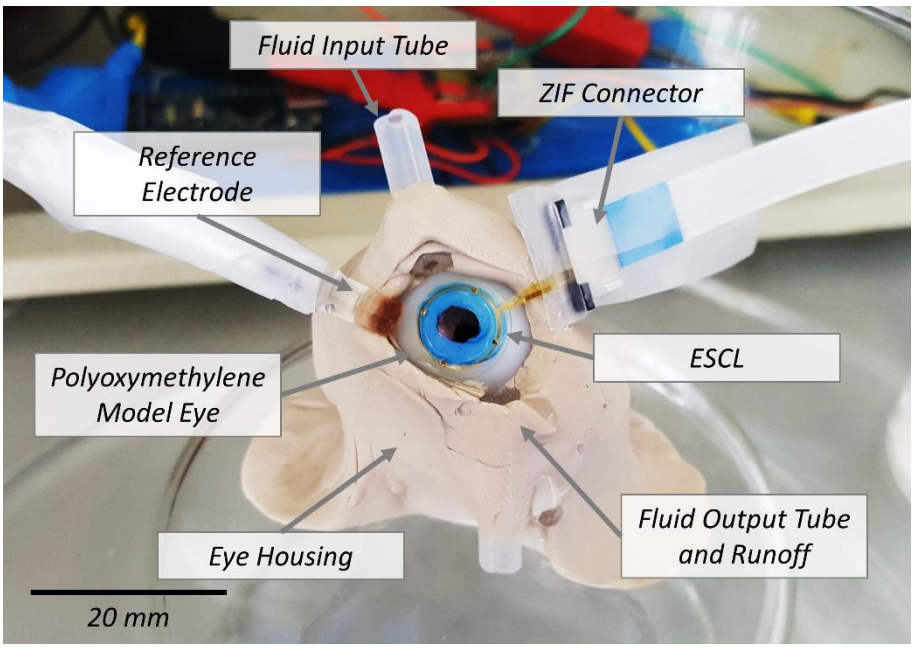

Figure 6.9: Photograph of the eye model used in spatiotemporal experiments.

To test the ESCL in a representative flow environment, an eye model was constructed using Newplast (modelling clay), silicone tubing and a polymer (polyoxymethylene) sphere (Figure 6.9). While a real eyeball has an overall radius of around 12 mm, contact lenses usually have radius of curvature closer to 9 mm to account for the shape of the cornea; thus, a sphere radius of 9 mm was chosen.

During experiments, fluid was added via the fluid input tube (placement chosen to mimic the location of the lachrymal ducts), and drained through or over the fluid output tube (placement chosen to mimic the location of the lachrymal puncta). The surface of the eye model was irrigated before each experiment, both topically and through the fluid input tube.

Spatiotemporal electrochemical sensing was performed using an updated version of the fast-switching chronoamperometric method described in Chapter 3. An analogue multiplexer driven by a microcontroller (Arduino Nano [99]) was used to address the working electrodes one-by-one in a cyclic sequence. Working electrode 1 (W1) was addressed for 60 ms, while W2-4 were addressed for 50 ms; this variation was used to tag W1 for easier signal separation. The sequence resulted in a frame rate of approximately 19 Hz (i.e. 19 electrodes per second). A potentiostat performed a chronoamperometric measurement (10 s, 0.4 V, 200 Hz sample rate) while the switching cycle repeated. In combination this produced a signal effectively consisting of a repeating four-step sequence of 50 ms (or 60 ms) chronoamperometric measurements (Figure 6.10 a). The 30-45 ms period within each measurement was isolated and, taking the arithmetic mean of the data within this period, a single current value was calculated at that time point (Figure 6.10 a). The time period was chosen to avoid non-Faradaic signal at the beginning of the chronoamperometric measurement and any switching noise at the end. For each experiment, a full (10 s) measurement was performed in 0.1 M KCl (a zero concentration measurement) and 0.5 mM FcMeOH (a high concentration measurement), before spatiotemporally-varying concentration profiles were investigated. Having established the linearity of the current-concentration relationship (for this range) in Section 6.3, these measurements were used to calibrate each electrode at each time point, as shown schematically in (Figure 6.10 b). Since each electrode was updated every four frames, linear interpolation was used to avoid a rolling shutter effect.

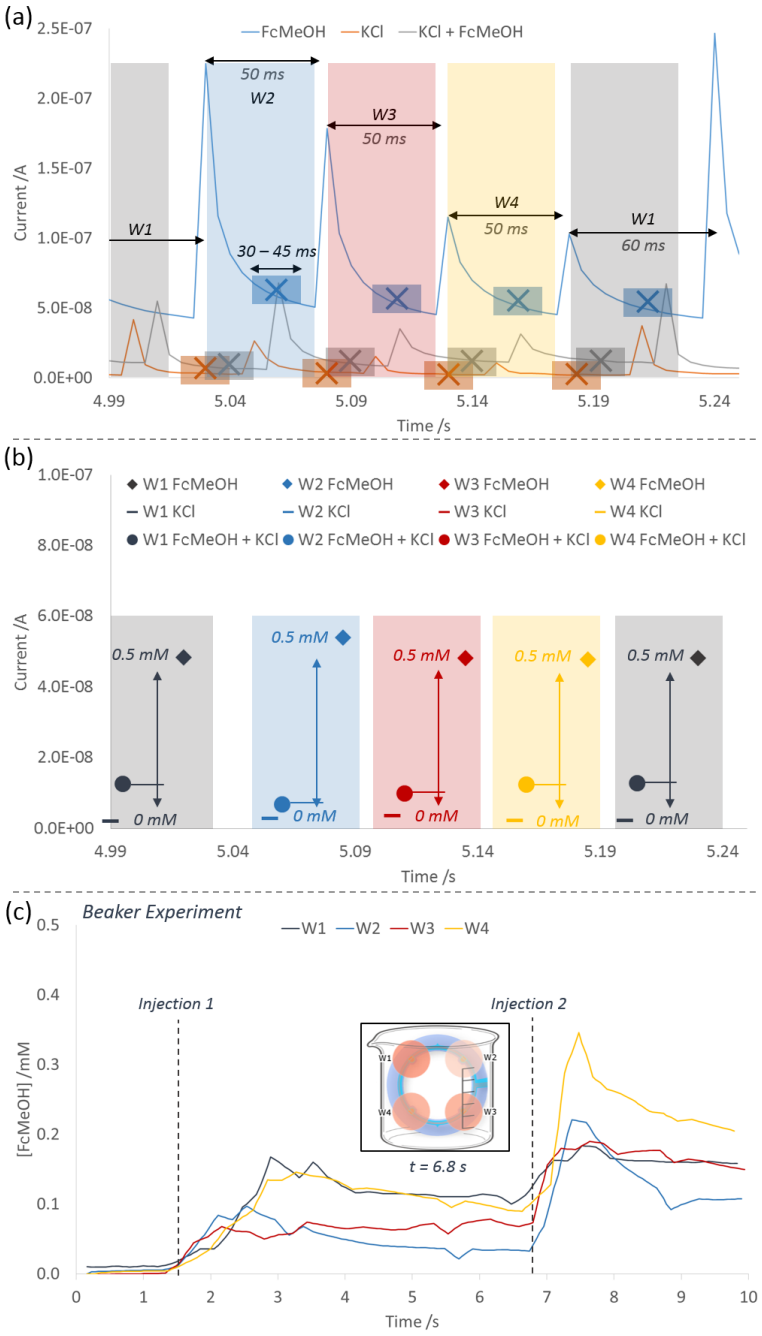

Figure 6.10: Illustration of the signal processing method, and the data produced. (a) Raw signal from fast-switching chronoamperometry in high concentration ('FcMeOH'), zero concentration ('KCl') and varying concentration ('KCl + FcMeOH'). Extraction of a single data point from each chronoamperometric sub-measurement is denoted by crosses; (b) calibration procedure using the extracted data points from (a), in which varying concentration measurements are compared with temporally-aligned high and zero measurements; (c) calibrated concentration data for each working electrode during a full 10 s experiment with varying concentration in a beaker. Two injections of FcMeOH into an initial volume of KCl are indicated. Inset: visual representation of the concentration at each working electrode, with concentration values represented by red colour shading (see Video 6.1).

Compared to the flexible microelectrode array discussed in Chapter 3, the quality of the chronoamperometric signal (Figure 6.10 a) was greatly improved, both in terms of signal-to-noise ratio, and reduction in variation between the different working electrodes. This is due to the use of microelectrode arrays, which increase the signal without sacrificing the enhanced sensing properties of microelectrodes, and the reduction of parasitic capacitance, inductance and resistance in the device (Section 6.1).

The result of this signal processing method is shown in Figure 6.10 c, in which time-varying concentration data are shown for each working electrode during a beaker experiment. In this experiment, measurements were first performed in a beaker of KCl (0.1 M) and FcMeOH (0.5 mM) to produce calibration data as described above. Next, two 1 ml injections of FcMeOH (0.5 mM) were added to a beaker KCl (0.1 M, initial volume ~ 5 ml) during a 10 s measurement period. The effects of each injection are clearly visible in the plot, and the distribution of concentration across the device shows some spatial inhomogeneity resulting from the position of the ESCL in the beaker and the location of the pipette tip. At the moment of injection, the concentrations measured at each electrode are somewhat volatile (e.g. t = 7 to 8 s), reflecting agitation and bulk movement in the two miscible fluids. As time progresses subsequent to each injection, mixing effects begin to reduce the disparity in concentration between each working electrode (e.g. t = 9 to 10 s).

To investigate the ESCL in environments more representative of the ocular surface, two more experiments were designed. Both experiments were performed multiple times, with representative results shown in Figure 6.11. As injection of fluid was performed manually, there was a large variation in the resulting data, as would be expected in the physiological case. For each experiment, at least two successful instances were carried out, with success being defined empirically and qualitatively as smooth injection of the correct quantity of fluid within the 10 s time frame, with no misalignment of the pipette or other components.

In the first experiment, the device was placed on top of a droplet of KCl for a zero concentration calibration measurement, then FcMeOH for a high concentration calibration measurement, with electrodes facing down. After calibration, a time- and space-varying concentration was created by slowly injecting FcMeOH (~ 0.5 ml) into an initial droplet of KCl (~ 0.5 ml) at the W1 and W4 side of the ESCL (Figure 6.11 a). By injecting the FcMeOH slowly, bulk mixing was kept to a minimum, and

very little increase in concentration was observed at W2 and W3, while W1 and W4 measured large changes in concentration. Flow of the droplet away from the ESCL towards the lower left direction during this experiment drew residual KCl into the W1 region, which resulted in a transient reduction in concentration from t = 6 to 8 s. As injection continued, both W1 and W4 measured an increasing concentration, with diffusive effects beginning to reach W3 by the end of the measurement period (t = 9 to 10 s).

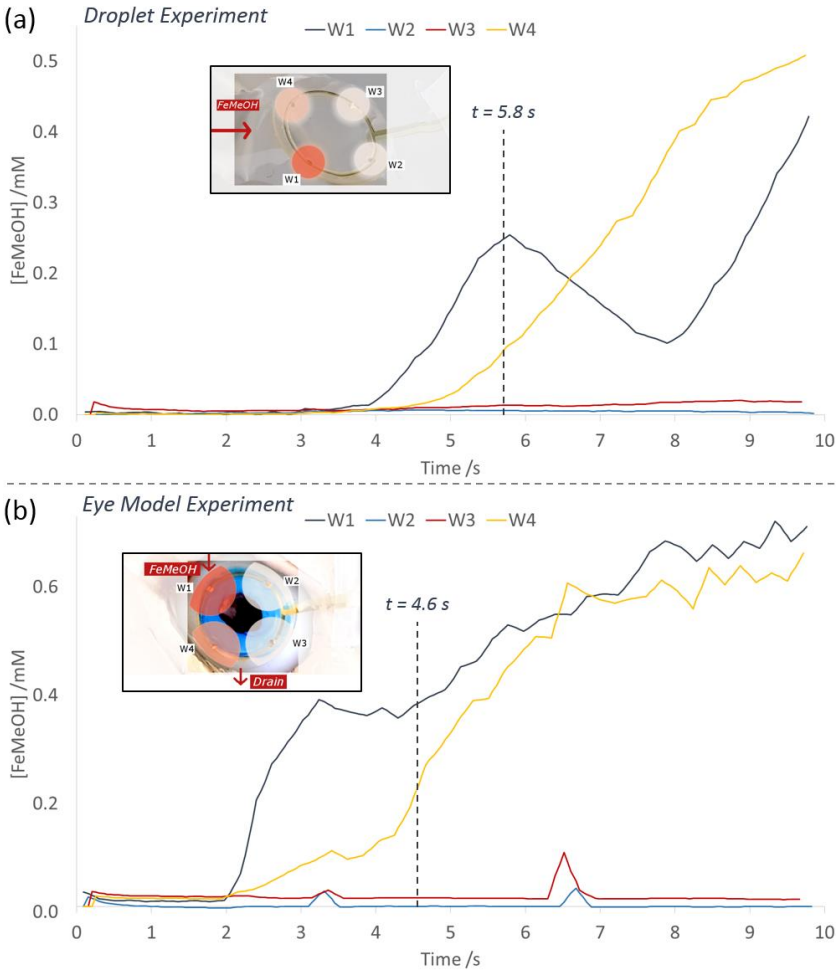

Figure 6.11. Concentration data for each working electrode during droplet and eye model experiments. (a) Concentration data for each working electrode during a 10 s droplet experiment, in which FcMeOH was pipetted into an initial droplet of KCl. Inset: visual representation of the concentration at each working electrode, with concentration values represented by red colour shading (see Video 6.2); (b) concentration data for each working electrode during a 10 s eye model experiment, in which FcMeOH was introduced to the fluid input of the eye model after previous irrigation with KCl. Inset: visual representation of the concentration at each working electrode, with concentration values represented by red colour shading (see Video 6.3).

In the second experiment, measurements were carried out on a model eye, built to mimic some aspects of the flow of tear film in the eye (Figure 6.9). While blinking effects and viscosity play key roles in the flow of the lachrymal fluid in a real eye, this experiment was designed as a proof of principle, to show that (a) spatial variation in concentration can be measured in a flow environment at a high rate of change, and (b) the ESCL can work effectively on the curved surface of a structure similar to the eye. Since little is known about the flow of tear film in the eye when a contact lens is worn, there may be diminishing returns in creating more 'accurate' eye models; a more informative next step would be to work in an animal or human model.

FcMeOH was injected through the fluid input tube, located in a position analogous to the lachrymal ducts (Figure 6.11 b, see Figure 6.3 a). The flow of liquid was observed first at W1, then W4, at which point the fluid ran along the lower eyelid section of the model to the fluid output tube, located in a position analogous to the lachrymal puncta. Fluid was occasionally observed around the W3 region, although without blinking effects the transport of fluid to W2 and W3 was very limited. The eye model was irrigated with KCl before the input of FcMeOH; calibration from the droplet experiment was used to ensure a good fluid connection during those procedures.

The data measured from the four working electrodes shows evidence of all empirically observed fluid flow effects. W1 quickly measured a concentration change (t = 2 s), and after an initially steep increase, continued to increase more slowly as residual KCl was flushed out (t = 7 to 10 s). W4 measured an increase in FcMeOH concentration after an additional delay (t = 2.5 s), and, since the fluid was flowing over a larger area after the initial injection point when compared to W1, measured a slower increase in local concentration (t = 3 to 5 s). W2 and W3 measured a slight increase in concentration on occasion, when fluid happened to flow away from the ordinary path (e.g. t = 6.5 s).

In the eye model experiment, concentrations above the maximum (0.5 mM) were occasionally measured, which shows some limitations of the normalisation technique; namely, in a static setting (such as the droplet experiment, from which normalisation data was obtained), some FcMeOH depletion occurs in the local environment of the sensors over the 10 s measurement period, approaching a pseudo-steady-state condition with growth of a secondary diffusion region supplying

the intermittent primary diffusion fields at each working electrode site (17% reduction in current during the first second of measurement, Figure 6.12).

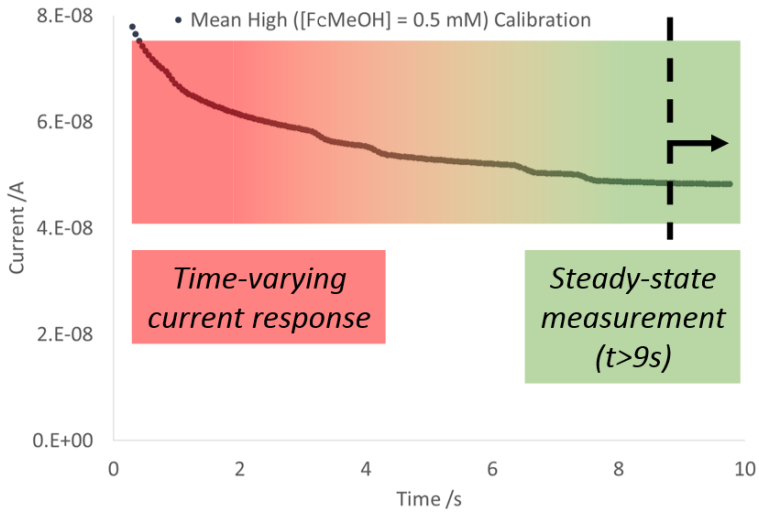

Figure 6.12: Mean current drawn from all working electrodes in both beaker and droplet high concentration calibration measurements ([FcMeOH] = 0.5 mM). Initially the current decreases, while after 9 s the change in current is less than 0.5% s^{-1}, indicating pseudo-steady-state conditions.

However, in the (fast) flow environment of the eye model, fresh FcMeOH replenishes the supply in the diffusion region of the working electrodes in a flow-, rather than diffusion-mediated manner. Therefore, as the measurement continues, the data from the static experiment becomes increasingly less applicable to a fast flow experiment. However, real flow in the eye occurs at a mean rate of 1.2 µl min^{-1} [111], although higher rates up to 7 µl min^{-1} may be observed during reflex tear production [55], and potentially even higher during blinking. These values are significantly below the approximate maximum flow rate of 3 ml min^{-1} generated in the model eye (chosen to test the performance of the lens in a particularly fast-flowing environment), and is much closer to a static environment, with low rates of concentration change. In calibration data, a steady-state (change in current < 0.5% s^{-1}) was reached within the ten second measurement period (Figure 6.12), and, with a mean tear film turnover of 16% min^{-1} [111], it is likely that a steady state calibration method would be appropriate for accurate measurements in the tear film under physiological flow conditions.

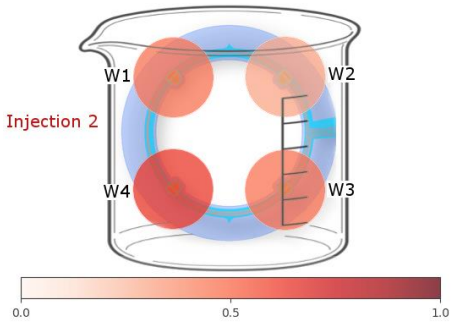

Video 6.1. Electrochemical video in which a colour map representation of FcMeOH concentration is used to visualise spatiotemporal concentration variation during the beaker experiment (see Supplementary Materials).

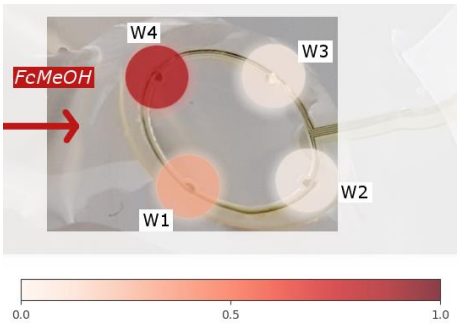

Video 6.2. Electrochemical video in which a colour map representation of FcMeOH concentration is used to visualise spatiotemporal concentration variation during the droplet experiment (see Supplementary Materials).

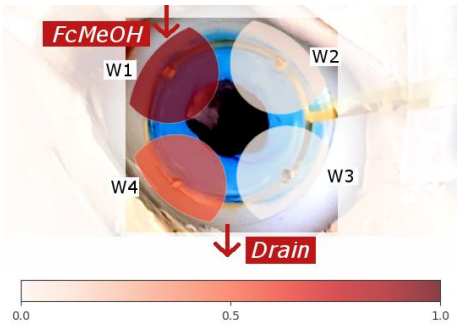

Video 6.3. Electrochemical video in which a colour map representation of FcMeOH concentration is used to visualise spatiotemporal concentration variation during the eye model experiment (see Supplementary Materials).

A spatiotemporal electrochemical measurement is intuitively visualised by an electrochemical video. For each experiment, the data were rescaled between 0 and 1, and used to create a colour map, in which FcMeOH concentration is represented

by the colour scale. These can be viewed in real time in Videos 1-3 (Supplementary Materials). These electrochemical 'videos' illustrate the various fluid effects discussed above.

6.5 Conclusions

A new ESCL has been designed and built, following SCL platform technology developed by Vásquez Quintero *et al*. [19]. Gold metallization sandwiched between layers of polyimide formed the wires and electrodes; after vias were opened to expose the electrode sites, the core device was encapsulated in TPU and moulded into a spherical cap shape. Four individually addressable microelectrode arrays were placed in the four quadrants of the lens, in order to monitor introduction, mixing and drainage of tear film from the lachrymal glands, across the surface of the eye, and out via the lachrymal puncta. In electrochemical tests the microelectrode arrays exhibited expected sensing characteristics when compared to a theoretical microdisc array, indicating that the fabrication method, the flexible substrate, encapsulation, moulding process and repeated mechanical deformation had no observable impact on the sensing performance of the device. In addition, the design of the ESCL, leading on from the results of Chapters 2 and 3, significantly increased the signal quality during high-speed chronoamperometry, with a reduction in parasitic capacitance, inductance and resistance, and the increased number of microdisc electrodes for each working electrode, greatly improving SNR.

Experiments in a beaker, on a droplet and in a model eye demonstrated the ability of this device to perform real-speed spatiotemporal electrochemistry, measuring spatially disparate concentrations at a rate of ~ 20 Hz. In the model eye experiment, the introduction, progress and draining of high-concentration fluid was tracked at real-speed, with flow rates far greater than the maximum expected flow rates of the tear film, indicating the suitability of this ESCL for monitoring progress of the tear film in the eye.

Future work may be carried out in developing the ESCL into a wireless device, improving comfort during use and overall utility. More working electrodes may be included to increase spatial resolution, and functionalised for various different biomarkers in order to investigate multiple processes in one device. This ESCL may also be used to investigate tear film flow in the eye when wearing a contact lens, something which is currently hard to measure accurately, and which information

may inform future ESCL designs. With a wireless ESCL capable of spatiotemporal monitoring of analytes in the eye, measurements of real clinical utility may be made.

7 Summary and Conclusions

This chapter summarises the work detailed in this thesis, the key results and the significance of the findings within the field. Suggestions for further work are also presented, followed by some concluding remarks.

7.1 Summary

This work has addressed a number of fundamental issues facing ESCLs in current research. The primary goal of an ESCL – to take measurements non-invasively and continuously, and of real clinical utility – were previously undermined by various factors affecting the measurement, including uncertainty about the composition of the tear fluid being measured, performance of the electrochemical sensor, and disparity between the concentrations measured in the tear film versus that measured in the blood. The advances detailed in this work have offered solutions to each of these issues.

Micro- (Chapter 3) and nanoelectrodes (Chapter 4) were investigated, with fabrication methods on flexible substrates developed for both types of sensor. Microelectrodes were deemed to be the most suitable for SCL integration. The development of spatially distributed microelectrode arrays, integrated for the first time into a soft, moulded SCL platform (Chapter 6), has increased sensing performance in comparison to the types of electrodes used in other ESCL prototypes, which are generally macroelectrodes of arbitrary physical form [3]. Microelectrodes have enhanced sensing properties such as better limit of detection, better signal to noise ratio (SNR) and shorter response time, all of which are important when carrying out measurements in the tear film – a dilute, low-volume medium undergoing continuous compositional change. Using microelectrode arrays allows control over the signal size of the working electrode, while preserving the enhanced sensing properties of the lens; previous work on ESCLs had not innovated with respect to the sensing properties of the working electrodes. Integrated into the neutral mechanical plane of the core polyimide substrate, and encapsulated in thermoplastic polyurethane, these microelectrode arrays have proven to be robust under expected use conditions such as full 180° folding, with sensing performance unchanged. Previous ESCL work has used PET [3] or silicone substrates [77] with issues of buckling [80], oxygen permeability, fabrication and user comfort. The ESCL presented in this thesis exhibits no buckling behaviour, is

stretchable, mouldable, and allows oxygen flow into the surface of the eye, and represents a clear improvement on the previous state of the art [16].

To address the uncertainty surrounding the composition of the tear fluid, a new electrochemical technique has been developed. Using fast-switching chronoamperometry, the introduction, mixing, progress and drainage of tear fluid can be tracked at real-speed at multiple sites across the surface of the cornea. This technique was introduced in Chapter 3, and refined in Chapter 6 to produce electrochemical videos of an analyte flowing across a model eye. This new technique provides far more information about the nature of the sensing medium than any previous work, in which a single electrochemical sensor is operated on a continuous basis [3,77]. Using a single potentiostat, and a basic multiplexing unit, the physical requirements of the system are kept to a minimum, ensuring a path to facile integration into a wireless SCL system. Similarly, power requirements remain well within the safe limit deliverable to a SCL (Chapter 6), with a simple measurement protocol and the use of microelectrode arrays (which can draw far less current than macroelectrodes).

The combination of the enhanced sensing properties of the advanced electrochemical sensors and the new electrochemical technique designed for this particular measurement challenge results in measurements of significantly greater clinical utility than the current state of the art. New tear fluid introduced at the lachrymal glands can be monitored before (and while) mixing into the bulk tear fluid in the eye. Subsequent analysis can produce a temporally accurate model of tear fluid composition, providing more information on the nature of the sensing medium than any other technique demonstrated in the literature. The data, after this retro-analysis, therefore yields information about the concentration of the most recently-introduced lachrymal fluid, reducing the time delay from concentration in the blood as much as possible, and reducing interference from environmental effects in the eye including evaporation, adulteration by other fluids such as rain or sweat, and drainage of the tear film via the lachrymal puncta or via tear formation.

Finally, to correct for the remaining difference between the concentration of an analyte measured in the tear film, and the equivalent concentration in the blood, a neural network method has been developed. This process learns the particular mathematical correction of an individual patient, without assuming anything about the biomarker in question or even the type of measurement being undertaken. On

simulated non-invasive data, the correction method improved the mean absolute normalised difference (MAND) versus the measured data from 46.9% to 4.8%, while the widely-used lag/bias model [7] achieved an improvement of only 46.9% to 21.2% This neural network method addresses the remaining step in producing data of real clinical utility from measurements made in the tear film.

The result of these three primary advances in ESCL technology, and the various secondary improvements made on previous state-of-the-art prototypes, is to create a blueprint for a complete system capable of continuous, non-invasive and unobtrusive measurement, capable of measuring multiple biomarkers simultaneously for a wide range of diagnostic applications, and performing measurements of sufficient quality to help draw meaningful diagnostic conclusions in a clinical setting. There is a number of exciting applications for this technology, including investigation into processes which cannot yet be satisfactorily monitored: e.g. the variations of salts and sugars in a person's body during normal day-to-day activities, exercise or ultramarathons; the spiking of cortisol in a firefighter's bloodstream as they perform hazardous tasks; dopamine and serotonin in an expecting mother, or even while giving birth; or a complete measurement of the endocrine system as a patient trials a new anti-depressant medication. This technology offers a window into a world we have only just started to explore.

7.2 Further Work

The use of this ESCL has been demonstrated in a wired device, on a model eye. There is therefore a number of clear advances to be made at this stage.

7.2.1 Development of Analogue Front-End Electronics

CMOS implementation of analogue electronics designed to harvest power from an inductive source, drive electrochemical measurement and communicate data has been demonstrated in previous work [3]. Integration of thinned silicon circuits into the polyimide/TPU platform has also been demonstrated [19]. An ESCL device suitable for clinical trials would benefit from development of a bespoke CMOS implementation of the spatiotemporal electrochemical measurement architecture. The requirements of this function are similar to implementations found in previous work (signal conditioning, a potentiostat unit, etc); the primary addition is an analogue multiplexing module, used to switch sequentially between working electrodes.

7.2.2 Development of Wireless Capability

Integration of wireless capability into this ESCL would enable comfortable use in live animals or humans. Therefore, the development of wireless capability should be a key focus. Wireless function of an ESCL has already been demonstrated, with an on-board chip containing signal conditioning and potentiostat functions, and an antenna for both wireless power and data transfer [3]. Following this established work, and other similar designs in SCLs, it only remains to design a custom chip to carry out the fast-switching chronoamperometry algorithm, and similar power conditioning and signal processing functions. Integration of the chip, design of the antenna, and the periphery devices has already been demonstrated, and these methods can be adapted to this device [19].

7.2.3 Refinement of the Placement of Working Electrodes

A refinement of the microelectrode array design may improve the sensing properties of the system. In Chapter 3 the fast-switching chronoamperometry technique was demonstrated with eight working electrodes, while the final ESCL design in Chapter 6 only used four. It would therefore be a simple task to integrate more working electrodes into the SCL platform – up to eight and likely more. Positioning of each electrode may also be refined. While an electrode array was placed in each quadrant in the final ESCL device (Figure 7.1 a), analysis of the tear film flow may be improved by placing more electrode arrays in the region near the lachrymal ducts (Figure 7.1 b), to better monitor ingress of new tear fluid. The physical design of the ESCL, and particularly the electrode placement, may require iterative optimisation, i.e. using a current ESCL design to better understand the flow characteristics of the tear film and thus inform the next generation of design.

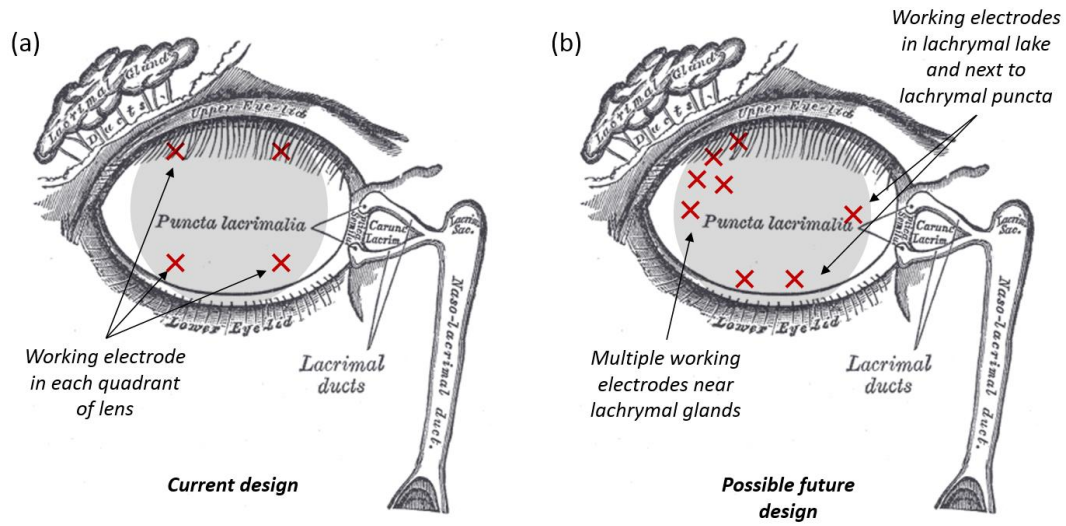

Figure 7.1: Possible refinement of the working electrode placement. (a) The current design, with a working electrode in each quadrant of the lens. (b) A possible future design, in which a cluster of working electrodes near the lachrymal glands monitors introduction of new tear fluid, and others are placed to take measurements in the lachrymal lake at the lower eyelid, and by the lachrymal puncta. Parts of this figure reproduced from Gray's Anatomy, Plate 896.

7.2.4 Functionalisation of the Working Electrodes and Clinical Testing

With a wireless device, testing in an animal or human subject would be possible with minimal irritation to the wearer. Building on established SCL designs which have been approved for clinical use, an optimised, wireless and safe ESCL could be built and the flow characteristics of the tear film may be investigated. Next, functionalisation of the working electrodes to select for different biomarkers may be developed. There exist already established chemical methods to functionalise an electrode for various biomarkers such as glucose, lactate and cortisol, which may be adapted to this device. Functionalisation could be carried out in bulk (across the whole device) or with more precision using inkjet printing methods. If multiple biomarkers are measured on one ESCL, differential or multimodal use may improve diagnoses, measurement fidelity, and cost efficiency of a device. In the design described in Chapter 6 an external reference electrode was used, but on-board reference electrodes have been demonstrated for ESCL designs [1], and, since they are used in common with each electrode, would not increase design footprint significantly.

7.2.5 Safe Encapsulation of the ESCL

Partial and full hydrogel encapsulations are both possible. For a partial encapsulation, the active side of the ESCL may be left exposed to allow for tear film contact; for a full encapsulation, analyte diffusion through the hydrogel may be sufficient for electrochemical sensing, or active functionalised hydrogels may be used to avoid the need to rely on diffusion [92]. Direct windows to the sensing sites may be created in the hydrogel, akin to those in the TPU top layer of the device described in Chapter 6. Alternatively, channels could be etched into the hydrogel to provide flow access to the sensors, perhaps with a passive blink-mediated pumping system to improve fluid transport (similar to musculovenous pumping) [91]. However, irritation might occur at the window or channel sites, and biofouling could result in significant flow problems.

7.2.6 Skin-based Sensing with the Nanoband Mesh Electrode

Beyond the ESCL itself, further development of the nanoelectrode devices described in Chapter 4 may be of interest. Although the through-flow architecture is not necessarily suitable for an ESCL, it may be of great utility to skin-based sensing. Skin-based electrochemical sensing has suffered from issues with sweat pooling – i.e. uncertainty about the composition of sweat from various points in time being mixed together in the sensing region (an analogous problem to that found in the tear film, which was addressed with the spatiotemporal sensing method). Planar sensors either trap sweat underneath the device, or wait for sweat to arrive on top of the device, both of which leads to great uncertainty in measurements. The through-flow nanoband mesh sensors, combined with a wicking fabric on top, would draw sweat through the sensing regions (the channels) and measure concentrations of biological markers during fluid transport. The sweat would subsequently be drawn away by the wicking fabric. This would ensure measurements are taken in only the most recently produced sweat, and unmixed with older sweat. The nanoband design of the sensors leads to extremely fast sensing capabilities, and the fabrication method allows for arbitrary 2-D designs to be created, for optimum conformation to skin and integration into devices. Future work may therefore develop the physical shape and functionalisation of these sensors to achieve non-invasive, continuous sensing in sweat.

7.2.7 Monitoring of Flowing Fluids

The active monitoring of flowing fluids described in Section 4.4 by the nanoband mesh devices may be further developed to cater for specific cases, such as monitoring of fluid concentrations in automated industrial fabrication facilities and water monitoring or purification. The electrochemical methods used to achieve this require further development to ensure measurement quality, and optimisation of the physical aspects of the nanoband mesh, such as pore size and design of the counter and reference electrodes, is also necessary.

7.2.8 Improvements to the Neural Network Method

The neural network method described in Chapter 5 may be developed further in a number of ways. First, by improving the method itself, such as increasing the resolution of the network to avoid averaging errors, increasing the number of neurons, or adding layers (to create a 'deep neural network'). Next, integration of covariate data into the method – e.g. allowing the network to analyse glucose data as well as cortisol data to establish corrections with respect to interactions or correlations between the two data sets. In a simple implementation, the covariate data sets (i.e. a number of additional time-series concentration data sets from monitoring of other covariate species) may simply be added to the neural network at the input neuron layer, and co-interactions allowed to establish themselves via iterative training as before. Finally, in the future, the generation of real non-invasive data sets, paired with concurrent measurement in the blood, will allow testing and refinement of this neural network method on real data.

7.3 Concluding Remarks

This work, culminating in a new ESCL architecture, new sensing methodology and new signal processing methods, advances the state of the art in ESCLs and wearable devices in general. Having utilised fabrication methods, technologies and materials with established biocompatibility and safety in other medical devices, there now exists a clear route to clinical utility for this device. With the potential for truly non-invasive, continuous, unobtrusive sensing, this ESCL could advance our understanding of a wide array of different conditions, and help change the way we approach healthcare and medicine.

8 References

[1] H. Yao, A.J. Shum, M. Cowan, I. Lähdesmäki, B.A. Parviz, A contact lens with embedded sensor for monitoring tear glucose level, Biosens. Bioelectron. 26 (2011) 3290–3296. https://doi.org/10.1016/j.bios.2010.12.042.

[2] N. Thomas, I. Lähdesmäki, B.A. Parviz, A contact lens with an integrated lactate sensor, Sensors Actuators, B Chem. 162 (2012) 128–134. https://doi.org/10.1016/j.snb.2011.12.049.

[3] H. Yao, Y. Liao, A.R. Lingley, A. Afanasiev, I. Lähdesmäki, B.P. Otis, B.A. Parviz, A contact lens with integrated telecommunication circuit and sensors for wireless and continuous tear glucose monitoring, J. Micromechanics Microengineering. 22 (2012) 075007. https://doi.org/10.1088/0960-1317/22/7/075007.

[4] A.J. Bandodkar, J. Wang, Non-invasive wearable electrochemical sensors: a review, Trends Biotechnol. 32 (2014) 363–371. https://doi.org/10.1016/j.tibtech.2014.04.005.

[5] W.R. Lovallo, Cortisol secretion patterns in addiction and addiction risk, Int. J. Psychophysiol. 59 (2006) 195–202. https://doi.org/10.1016/j.ijpsycho.2005.10.007.

[6] A. Hartmann, Twenty-Four Hour Cortisol Release Profiles in Patients With Alzheimer's and Parkinson's Disease Compared to Normal Controls: Ultradian Secretory Pulsatility and Diurnal Variation, Neurobiol. Aging. 18 (1997) 285–289. https://doi.org/10.1016/S0197-4580(97)80309-0.

[7] C. Cobelli, M. Schiavon, C. Dalla Man, A. Basu, R. Basu, Interstitial Fluid Glucose Is Not Just a Shifted-in-Time but a Distorted Mirror of Blood Glucose: Insight from an In Silico Study, Diabetes Technol. Ther. 18 (2016) 505–511. https://doi.org/10.1089/dia.2016.0112.

[8] B.S. McEwen, Protective and Damaging Effects of Stress Mediators, N. Engl. J. Med. 338 (1998) 171–179. https://doi.org/10.1056/NEJM199801153380307.

[9] R.S. Stawski, K.E. Cichy, J.R. Piazza, D.M. Almeida, Associations among

daily stressors and salivary cortisol: Findings from the National Study of Daily Experiences, Psychoneuroendocrinology. 38 (2013) 2654–2665. https://doi.org/10.1016/j.psyneuen.2013.06.023.

[10] W. Jia, A.J. Bandodkar, G. Valdés-Ramírez, J.R. Windmiller, Z. Yang, J. Ramírez, G. Chan, J. Wang, Electrochemical Tattoo Biosensors for Real-Time Noninvasive Lactate Monitoring in Human Perspiration, Anal. Chem. 85 (2013) 6553–6560. https://doi.org/10.1021/ac401573r.

[11] N.M. Farandos, A.K. Yetisen, M.J. Monteiro, C.R. Lowe, S.H. Yun, Contact lens sensors in ocular diagnostics, Adv. Healthc. Mater. 4 (2015) 792–810. https://doi.org/10.1002/adhm.201400504.

[12] Google Press Release, (2014). https://googleblog.blogspot.co.uk/2014/01/introducing-our-smart-contact-lens.html.

[13] M.S. Mannoor, H. Tao, J.D. Clayton, A. Sengupta, D.L. Kaplan, R.R. Naik, N. Verma, F.G. Omenetto, M.C. McAlpine, lGraphene-based wireless bacteria detection on tooth ename, Nat. Commun. 3 (2012) 763. https://doi.org/10.1038/ncomms1767.

[14] J. Kim, W.R. de Araujo, I.A. Samek, A.J. Bandodkar, W. Jia, B. Brunetti, T.R.L.C. Paixão, J. Wang, Wearable temporary tattoo sensor for real-time trace metal monitoring in human sweat, Electrochem. Commun. 51 (2015) 41–45. https://doi.org/10.1016/j.elecom.2014.11.024.

[15] J. Park, J. Kim, S.-Y. Kim, W.H. Cheong, J. Jang, Y.-G. Park, K. Na, Y.-T. Kim, J.H. Heo, C.Y. Lee, J.H. Lee, F. Bien, J.-U. Park, Soft, smart contact lenses with integrations of wireless circuits, glucose sensors, and displays, Sci. Adv. 4 (2018) eaap9841. https://doi.org/10.1126/sciadv.aap9841.

[16] M. Donora, A.V. Quintero, H. De Smet, I. Underwood, Spatiotemporal Electrochemical Sensing in a Smart Contact Lens, Sensors Actuators B Chem. (2019) 127203. https://doi.org/10.1016/j.snb.2019.127203.

[17] J. Kim, S. Imani, W.R. de Araujo, J. Warchall, G. Valdés-Ramírez, T.R.L.C. Paixão, P.P. Mercier, J. Wang, Wearable salivary uric acid mouthguard biosensor with integrated wireless electronics, Biosens. Bioelectron. 74 (2015) 1061–1068. https://doi.org/10.1016/j.bios.2015.07.039.

[18] C. Vanhaverbeke, R. Verplancke, J. De Smet, D. Cuypers, H. De Smet, Microfabrication of a spherically curved liquid crystal display enabling the integration in a smart contact lens, Displays. 49 (2017) 16–25. https://doi.org/10.1016/j.displa.2017.05.005.

[19] A. Vásquez Quintero, R. Verplancke, H. De Smet, J. Vanfleteren, Stretchable Electronic Platform for Soft and Smart Contact Lens Applications, Adv. Mater. Technol. 2 (2017) 1700073. https://doi.org/10.1002/admt.201700073.

[20] M. Leonardi, E.M. Pitchon, A. Bertsch, P. Renaud, A. Mermoud, Wireless contact lens sensor for intraocular pressure monitoring: Assessment on enucleated pig eyes, Acta Ophthalmol. 87 (2009) 433–437. https://doi.org/10.1111/j.1755-3768.2008.01404.x.

[21] Sensimed, (2015). http://www.sensimed.ch/en/.

[22] H. Sei Kwang, K. Do Hee, Smart contact lens and smart eye glasses, Front. Bioeng. Biotechnol. 4 (2016). https://doi.org/10.3389/conf.FBIOE.2016.01.01493.

[23] J. Pandey, Y.-T. Liao, A. Lingley, R. Mirjalili, B. Parviz, B.P. Otis, A Fully Integrated RF-Powered Contact Lens With a Single Element Display, IEEE Trans. Biomed. Circuits Syst. 4 (2010) 454–461. https://doi.org/10.1109/TBCAS.2010.2081989.

[24] Contact Lens Spectrum, (2019) 18.

[25] C.S.A. Musgrave, F. Fang, Contact Lens Materials: A Materials Science Perspective, Materials (Basel). 12 (2019) 261. https://doi.org/10.3390/ma12020261.

[26] Contact Lenses, Ophthalmology. 92 (1985) 138–143. https://doi.org/10.1016/S0161-6420(85)34123-4.

[27] M. Lira, C. Pereira, M.E.C.D. Real Oliveira, E.M.S. Castanheira, Importance of contact lens power and thickness in oxygen transmissibility, Contact Lens Anterior Eye. 38 (2015) 120–126. https://doi.org/10.1016/j.clae.2014.12.002.

[28] K. Mansouri, T. Shaarawy, Continuous intraocular pressure monitoring with a wireless ocular telemetry sensor: initial clinical experience in patients with open angle glaucoma, Br. J. Ophthalmol. 95 (2011) 627–629.

https://doi.org/10.1136/bjo.2010.192922.

[29] S. Gupta, W.T. Navaraj, L. Lorenzelli, R. Dahiya, Ultra-thin chips for high-performance flexible electronics, Npj Flex. Electron. 2 (2018) 8. https://doi.org/10.1038/s41528-018-0021-5.

[30] M.A. Hopcroft, W.D. Nix, T.W. Kenny, What is the Young's Modulus of Silicon?, J. Microelectromechanical Syst. 19 (2010) 229–238. https://doi.org/10.1109/JMEMS.2009.2039697.

[31] Dupont, Dupont Kapton HN Datasheet, (n.d.). https://www.dupont.com/content/dam/dupont/products-and-services/membranes-and-films/polyimde-films/documents/DEC-Kapton-HN-datasheet.pdf.

[32] M.D. Young, W.J. Benjamin, Oxygen Permeability of the Hypertransmissible Contact Lenses, Eye Contact Lens Sci. Clin. Pract. 29 (2003) S17–S21. https://doi.org/10.1097/00140068-200301001-00006.

[33] M. Nasreldin, R. Delattre, M. Ramuz, C. Lahuec, T. Djenizian, J.-L. de Bougrenet de la Tocnaye, Flexible Micro-Battery for Powering Smart Contact Lens, Sensors. 19 (2019) 2062. https://doi.org/10.3390/s19092062.

[34] M. Falk, V. Andoralov, Z. Blum, J. Sotres, D.B. Suyatin, T. Ruzgas, T. Arnebrant, S. Shleev, Biofuel cell as a power source for electronic contact lenses, Biosens. Bioelectron. 37 (2012) 38–45. https://doi.org/10.1016/j.bios.2012.04.030.

[35] IEEE Standard for Safety Levels with Respect to Human Exposure to Radio Frequency Electromagnetic Fields, 3 kHz to 300 GHz, IEEE Std C95.1. (1999) 1–83. https://doi.org/10.1109/IEEESTD.1999.89423.

[36] S. Nayak, N.R. Blumenfeld, T. Laksanasopin, S.K. Sia, Point-of-Care Diagnostics: Recent Developments in a Connected Age, Anal. Chem. 89 (2017) 102–123. https://doi.org/10.1021/acs.analchem.6b04630.

[37] M. Yan, Y. Kawamata, P.S. Baran, Synthetic Organic Electrochemical Methods Since 2000: On the Verge of a Renaissance, Chem. Rev. 117 (2017) 13230–13319. https://doi.org/10.1021/acs.chemrev.7b00397.

[38] D. Bruen, C. Delaney, L. Florea, D. Diamond, Glucose Sensing for Diabetes

Monitoring: Recent Developments, Sensors. 17 (2017) 1866. https://doi.org/10.3390/s17081866.

[39] A.J. Bard, L.R. Faulkner, Electrochemical Methods: Fundamentals and Applications, 2nd Edition, 2001.

[40] C. Cannes, F. Kanoufi, A.J. Bard, Cyclic voltammetry and scanning electrochemical microscopy of ferrocenemethanol at monolayer and bilayer-modified gold electrodes, J. Electroanal. Chem. 547 (2003) 83–91. https://doi.org/10.1016/S0022-0728(03)00192-X.

[41] M. Matsumiya, M. Terazono, K. Tokuraku, Temperature dependence of kinetics and diffusion coefficients for ferrocene/ferricenium in ammonium-imide ionic liquids, Electrochim. Acta. 51 (2006) 1178–1183. https://doi.org/10.1016/j.electacta.2005.06.006.

[42] K.R.J. Lovelock, A. Ejigu, S.F. Loh, S. Men, P. Licence, D.A. Walsh, On the diffusion of ferrocenemethanol in room-temperature ionic liquids: an electrochemical study, Phys. Chem. Chem. Phys. 13 (2011) 10155. https://doi.org/10.1039/c1cp20392d.

[43] M. Falk, R. Sultana, M.J. Swann, A.R. Mount, N.J. Freeman, Nanoband array electrode as a platform for high sensitivity enzyme-based glucose biosensing, Bioelectrochemistry. 112 (2016) 100–105. https://doi.org/10.1016/j.bioelechem.2016.04.002.

[44] R.M. Wightman, Voltammetry with Microscopic Electrodes in New Domains, Science (80-.). 240 (1988) 415–420. https://doi.org/10.1126/science.240.4851.415.

[45] I. Schmueser, A.J. Walton, J.G. Terry, H.L. Woodvine, N.J. Freeman, A.R. Mount, A systematic study of the influence of nanoelectrode dimensions on electrode performance and the implications for electroanalysis and sensing, Faraday Discuss. 164 (2013) 295. https://doi.org/10.1039/c3fd00038a.

[46] N.J. Freeman, R. Sultana, N. Reza, H. Woodvine, J.G. Terry, A.J. Walton, C.L. Brady, I. Schmueser, A.R. Mount, Comparison of the performance of an array of nanoband electrodes with a macro electrode with similar overall area, Phys. Chem. Chem. Phys. 15 (2013) 8112. https://doi.org/10.1039/c3cp50759a.

[47] I. Schmüser, The design, fabrication and characterisation of nanoelectrodes for electrochemical sensing, (2015).

[48] S.L. Caston, R.L. McCarley, Characteristics of nanoscopic Au band electrodes, J. Electroanal. Chem. 529 (2002) 124–134. https://doi.org/10.1016/S0022-0728(02)00948-8.

[49] M. Donora, E. Gonzalez-Fernandez, A. Vásquez Quintero, H. De Smet, I. Underwood, Spatiotemporal electrochemistry on flexible microelectrode arrays: Progress towards smart contact lens integration, Sensors Actuators B Chem. 296 (2019) 126671. https://doi.org/10.1016/j.snb.2019.126671.

[50] J.G. Terry, I. Schmüser, I. Underwood, D.K. Corrigan, N.J. Freeman, A.S. Bunting, A.R. Mount, A.J. Walton, Nanoscale electrode arrays produced with microscale lithographic techniques for use in biomedical sensing applications., IET Nanobiotechnol. 7 (2013) 125–34. https://doi.org/10.1049/iet-nbt.2013.0049.

[51] U. Stahl, M. Willcox, F. Stapleton, Osmolality and tear film dynamics, Clin. Exp. Optom. 95 (2012) 3–11. https://doi.org/10.1111/j.1444-0938.2011.00634.x.

[52] K. a. Polse, Tear flow under hydrogel contact lenses, Investig. Ophthalmol. Vis. Sci. 18 (1979) 409–413.

[53] S. Khanal, T.J. Millar, Nanoscale phase dynamics of the normal tear film, Nanomedicine Nanotechnology, Biol. Med. 6 (2010) 707–713. https://doi.org/10.1016/j.nano.2010.06.002.

[54] M.B. Jones, C.P. Please, D.L.S. McElwain, G.R. Fulford, A.P. Roberts, M.J. Collins, Dynamics of tear film deposition and draining, Math. Med. Biol. A J. IMA. 22 (2005) 265–288. https://doi.org/10.1093/imammb/dqi012.

[55] R.L. Farris, R.N. Stuchell, I.D. Mandel, Basal and Reflex Human Tear Analysis, Ophthalmology. 88 (1981) 852–857. https://doi.org/10.1016/S0161-6420(81)34939-2.

[56] R.N. Stuchell, R.L. Farris, I.D. Mandel, Basal and Reflex Human Tear Analysis, Ophthalmology. 88 (1981) 858–862. https://doi.org/10.1016/S0161-6420(81)34938-0.

[57] A. Tomlinson, S. Khanal, Assessment of Tear Film Dynamics: Quantification Approach, Ocul. Surf. 3 (2005) 81–95. https://doi.org/10.1016/S1542-0124(12)70157-X.

[58] J.T. Baca, D.N. Finegold, S.A. Asher, Tear Glucose Analysis for the Noninvasive Detection and Monitoring of Diabetes Mellitus, Ocul. Surf. 5 (2007) 280–293. https://doi.org/10.1016/S1542-0124(12)70094-0.

[59] J.T. Baca, C.R. Taormina, E. Feingold, D.N. Finegold, J.J. Grabowski, S.A. Asher, Mass Spectral Determination of Fasting Tear Glucose Concentrations in Nondiabetic Volunteers, Clin. Chem. 53 (2007) 1370–1372. https://doi.org/10.1373/clinchem.2006.078543.

[60] B. Peng, J. Lu, A.S. Balijepalli, T.C. Major, B.E. Cohan, M.E. Meyerhoff, Evaluation of enzyme-based tear glucose electrochemical sensors over a wide range of blood glucose concentrations, Biosens. Bioelectron. 49 (2013) 204–209. https://doi.org/10.1016/j.bios.2013.05.014.

[61] L. Yu, Z. Yang, M. An, Lab on the eye: A review of tear-based wearable devices for medical use and health management, Biosci. Trends. 13 (2019) 308–313. https://doi.org/10.5582/bst.2019.01178.

[62] Y.-T. Liao, H. Yao, A. Lingley, B. Parviz, B.P. Otis, A 3-uW CMOS Glucose Sensor for Wireless Contact-Lens Tear Glucose Monitoring, IEEE J. Solid-State Circuits. 47 (2012) 335–344. https://doi.org/10.1109/JSSC.2011.2170633.

[63] Á. Farkas, R. Vámos, T. Bajor, N. Müllner, Á. Lázár, A. Hrabá, Utilization of lacrimal urea assay in the monitoring of hemodialysis: Conditions, limitations and lacrimal arginase characterization, Exp. Eye Res. 76 (2003) 183–192. https://doi.org/10.1016/S0014-4835(02)00276-2.

[64] A. Singh, A. Kaushik, R. Kumar, M. Nair, S. Bhansali, Electrochemical Sensing of Cortisol: A Recent Update, Appl. Biochem. Biotechnol. 174 (2014) 1115–1126. https://doi.org/10.1007/s12010-014-0894-2.

[65] S.K. Kim, D. Kim, S. Jeon, Electrochemical determination of serotonin on glassy carbon electrode modified with various graphene nanomaterials, Sensors Actuators B Chem. 174 (2012) 285–291. https://doi.org/10.1016/j.snb.2012.08.034.

[66] S. Reddy, B.E. Kumara Swamy, H. Jayadevappa, CuO nanoparticle sensor for the electrochemical determination of dopamine, Electrochim. Acta. 61 (2012) 78–86. https://doi.org/10.1016/j.electacta.2011.11.091.

[67] L.K. Banbury, Stress biomarkers in the tear film, Southern Cross University, 2009.

[68] F. Holsboer, The Corticosteroid Receptor Hypothesis of Depression, Neuropsychopharmacology. 23 (2000) 477–501. https://doi.org/10.1016/S0893-133X(00)00159-7.

[69] Y.I. Sheline, P.W. Wang, M.H. Gado, J.G. Csernansky, M.W. Vannier, Hippocampal atrophy in recurrent major depression, Proc. Natl. Acad. Sci. 93 (1996) 3908–3913. https://doi.org/10.1073/pnas.93.9.3908.

[70] D.L. Delahanty, A.J. Raimonde, E. Spoonster, Initial posttraumatic urinary cortisol levels predict subsequent PTSD symptoms in motor vehicle accident victims, Biol. Psychiatry. 48 (2000) 940–7. http://www.ncbi.nlm.nih.gov/pubmed/11074232 (accessed June 3, 2019).

[71] P. Chhadva, T. Lee, C.D. Sarantopoulos, A.S. Hackam, A.L. McClellan, E.R. Felix, R.C. Levitt, A. Galor, Human Tear Serotonin Levels Correlate with Symptoms and Signs of Dry Eye, Ophthalmology. 122 (2015) 1675–1680. https://doi.org/10.1016/j.ophtha.2015.04.010.

[72] V. Andoralov, S. Shleev, T. Arnebrant, T. Ruzgas, Flexible micro(bio)sensors for quantitative analysis of bioanalytes in a nanovolume of human lachrymal liquid, Anal. Bioanal. Chem. 405 (2013) 3871–3879. https://doi.org/10.1007/s00216-013-6756-x.

[73] N. von Thun und Hohenstein-Blaul, S. Funke, F.H. Grus, Tears as a source of biomarkers for ocular and systemic diseases, Exp. Eye Res. 117 (2013) 126–137. https://doi.org/10.1016/j.exer.2013.07.015.

[74] M. Nakatsukasa, C. Sotozono, K. Shimbo, N. Ono, H. Miyano, A. Okano, J. Hamuro, S. Kinoshita, Amino acid profiles in human tear fluids analyzed by high-performance liquid chromatography and electrospray ionization tandem mass spectrometry, Am. J. Ophthalmol. 151 (2011) 799–808. https://doi.org/10.1016/j.ajo.2010.11.003.

[75] Sensimed AG, SENSIMED Triggerfish® provides reproducible 24 hour profile, 2014. http://www.sensimed.ch/en/.

[76] G.E. Dunbar, B. Shen, A. Aref, The Sensimed Triggerfish contact lens sensor: efficacy, safety, and patient perspectives, Clin. Ophthalmol. Volume 11 (2017) 875–882. https://doi.org/10.2147/OPTH.S109708.

[77] J. Kim, M. Kim, M.S. Lee, K. Kim, S. Ji, Y.T. Kim, J. Park, K. Na, K.H. Bae, H.K. Kim, F. Bien, C.Y. Lee, J.U. Park, Wearable smart sensor systems integrated on soft contact lenses for wireless ocular diagnostics, Nat. Commun. 8 (2017). https://doi.org/10.1038/ncomms14997.

[78] A. Georgiev, D. Dimov, E. Spassova, J. Assa, P. Dineff, G. Danev, Chemical and Physical Properties of Polyimides: Biomedical and Engineering Applications, in: High Perform. Polym. - Polyimides Based - From Chem. to Appl., InTech, 2012. https://doi.org/10.5772/53918.

[79] Y. Wang, W. Wang, Z. Zhang, L. Xu, P. Li, Study of the glass transition temperature and the mechanical properties of PET/modified silica nanocomposite by molecular dynamics simulation, Eur. Polym. J. 75 (2016) 36–45. https://doi.org/10.1016/j.eurpolymj.2015.11.038.

[80] J. De Smet, A. Avci, R. Beernaert, D. Cuypers, H. De Smet, Design and wrinkling behavior of a contact lens with an integrated liquid crystal light modulator, IEEE/OSA J. Disp. Technol. 8 (2012) 299–305. https://doi.org/10.1109/JDT.2012.2183575.

[81] R. Di Felice, D. Cazzola, S. Cobror, L. Oriani, Oxygen permeation in PET bottles with passive and active walls, Packag. Technol. Sci. 21 (2008) 405–415. https://doi.org/10.1002/pts.820.

[82] M. Donora, I. Underwood, 70-4: Late-News Paper: Electronic Contact Lens for Senses beyond Sight, SID Symp. Dig. Tech. Pap. 50 (2019) 996–999. https://doi.org/10.1002/sdtp.13094.

[83] R.R. Richardson, J.A. Miller, W.M. Reichert, Polyimides as biomaterials: preliminary biocompatibility testing, Biomaterials. 14 (1993) 627–635. https://doi.org/10.1016/0142-9612(93)90183-3.

[84] P. Starr, C.M. Agrawal, S. Bailey, Biocompatibility of common polyimides with

human endothelial cells for a cardiovascular microsensor, J. Biomed. Mater. Res. Part A. 104 (2016) 406–412. https://doi.org/10.1002/jbm.a.35578.

[85] HD MicroSystems, PI-2600 Series – Low Stress Applications, (2009) 1–4. https://www.dupont.com/content/dam/dupont/products-and-services/electronic-and-electrical-materials/semiconductor-fabrication-and-packaging-materials/documents/PI-2600_ProcessGuide.pdf.

[86] S.R.I. Gabran, M.T. Salam, J. Dian, Y. El-Hayek, J.L. Perez Velazquez, R. Genov, P.L. Carlen, M.M.A. Salama, R.R. Mansour, 3-D Flexible Nano-Textured High-Density Microelectrode Arrays for High-Performance Neuro-Monitoring and Neuro-Stimulation, IEEE Trans. Neural Syst. Rehabil. Eng. 22 (2014) 1072–1082. https://doi.org/10.1109/TNSRE.2014.2322077.

[87] F. Waschkowski, S. Hesse, A. Rieck, T. Lohmann, C. Brockmann, T. Laube, N. Bornfeld, G. Thumann, P. Walter, W. Mokwa, S. Johnen, G. Roessler, Development of very large electrode arrays for epiretinal stimulation (VLARS), Biomed. Eng. Online. 13 (2014) 11. https://doi.org/10.1186/1475-925X-13-11.

[88] T. Li, B. Sun, K. Xia, Q. Zeng, T. Wu, M.S. Humayun, Design and fabrication of a high-density flexible microelectrode array, in: 2017 IEEE 12th Int. Conf. Nano/Micro Eng. Mol. Syst., IEEE, 2017: pp. 299–302. https://doi.org/10.1109/NEMS.2017.8017029.

[89] P. Alves, R. Cardoso, T.R. Correia, B.P. Antunes, I.J. Correia, P. Ferreira, Surface modification of polyurethane films by plasma and ultraviolet light to improve haemocompatibility for artificial heart valves, Colloids Surfaces B Biointerfaces. 113 (2014) 25–32. https://doi.org/10.1016/j.colsurfb.2013.08.039.

[90] A.V. Quintero, D. Briand, N.F. De Rooij, Flip-chip integration of Si bare dies on polymeric substrates at low temperature using ICA vias made in dry film photoresist, J. Micromechanics Microengineering. 25 (2015). https://doi.org/10.1088/0960-1317/25/4/045013.

[91] Q. Yu, J.M. Bauer, J.S. Moore, D.J. Beebe, Responsive biomimetic hydrogel valve for microfluidics, Appl. Phys. Lett. 78 (2001) 2589–2591. https://doi.org/10.1063/1.1367010.

[92] U.A. Aregueta-Robles, A.J. Woolley, L.A. Poole-Warren, N.H. Lovell, R.A. Green, Organic electrode coatings for next-generation neural interfaces, Front. Neuroeng. 7 (2014). https://doi.org/10.3389/fneng.2014.00015.

[93] R. Verplancke, F. Bossuyt, D. Cuypers, J. Vanfleteren, Thin-film stretchable electronics technology based on meandering interconnections: Fabrication and mechanical performance, J. Micromechanics Microengineering. 22 (2012). https://doi.org/10.1088/0960-1317/22/1/015002.

[94] P.N. Bartlett, S.L. Taylor, An accurate microdisc simulation model for recessed microdisc electrodes, J. Electroanal. Chem. 453 (1998) 49–60. https://doi.org/10.1016/S0022-0728(98)00242-3.

[95] Y. Saito, A Theoretical Study on the Diffusion Current at the Stationary Electrodes of Circular and Narrow Band Types, Rev. Polarogr. 15 (1968) 177–187. https://doi.org/10.5189/revpolarography.15.177.

[96] K.G. Shah, V.M. Tolosa, A.C. Tooker, S.H. Felix, S.S. Pannu, Improved chronic neural stimulation using high surface area platinum electrodes., Conf. Proc. IEEE Eng. Med. Biol. Soc. 2013 (2013) 1546–9. https://doi.org/10.1109/EMBC.2013.6609808.

[97] S. Trasatti, O.A. Petrii, Real surface area measurements in electrochemistry, J. Electroanal. Chem. 327 (1992) 353–376. https://doi.org/10.1016/0022-0728(92)80162-W.

[98] A.D. McNaught, A. Wilkinson, IUPAC, Compendium of Chemical Terminology, 2nd Editio, Blackwell Scientific Publications, 1997.

[99] Arduino Nano Guide, (n.d.). https://www.arduino.cc/en/Guide/ArduinoNano.

[100] M.L. Khraiche, W.B. Phillips, N. Jackson, J. Muthuswamy, Sustained elevation of activity of developing neurons grown on polyimide microelectrode arrays (MEA) in response to ultrasound exposure, Microsyst. Technol. 23 (2017) 3671–3683. https://doi.org/10.1007/s00542-016-3150-6.

[101] M.S. Nahvi, F.A. Boroumand, M.H. Maghami, A.M. Sodagar, A. Shojaei, J. Mirnajafi-Zadeh, Design, fabrication, and test of flexible thin-film microelectrode arrays for neural interfaces, Can. Conf. Electr. Comput. Eng. 2017-June (2017) 1–4. https://doi.org/10.1109/CCECE.2017.7970775.

[102] F. Barz, A. Livi, M. Lanzilotto, M. Maranesi, L. Bonini, O. Paul, P. Ruther, Versatile, modular 3D microelectrode arrays for neuronal ensemble recordings: from design to fabrication, assembly, and functional validation in non-human primates, J. Neural Eng. 14 (2017) 036010. https://doi.org/10.1088/1741-2552/aa5a90.

[103] Q. Yan, B. Peng, G. Su, B.E. Cohan, T.C. Major, M.E. Meyerhoff, Measurement of tear glucose levels with amperometric glucose biosensor/capillary tube configuration., Anal. Chem. 83 (2011) 8341–6. https://doi.org/10.1021/ac201700c.

[104] E.K. Adam, M. Kumari, Assessing salivary cortisol in large-scale, epidemiological research, Psychoneuroendocrinology. 34 (2009) 1423–1436. https://doi.org/10.1016/j.psyneuen.2009.06.011.

[105] O. Staal, H. Hansen, S. Christiansen, A. Fougner, S. Carlsen, Ø. Stavdahl, Differences Between Flash Glucose Monitor and Fingerprick Measurements, Biosensors. 8 (2018) 93. https://doi.org/10.3390/bios8040093.

[106] H. Takahashi, R. Nishimura, Y. Onda, K. Ando, D. Tsujino, K. Utsunomiya, Prediction of nocturnal hypoglycemia unawareness by fasting glucose levels or post-breakfast glucose fluctuations in patients with type 1 diabetes receiving insulin degludec: A pilot study, PLoS One. 12 (2017) e0177283. https://doi.org/10.1371/journal.pone.0177283.

[107] M. Schiavon, C. Dalla Man, S. Dube, M. Slama, Y.C. Kudva, T. Peyser, A. Basu, R. Basu, C. Cobelli, Modeling Plasma-to-Interstitium Glucose Kinetics from Multitracer Plasma and Microdialysis Data, Diabetes Technol. Ther. 17 (2015) 825–831. https://doi.org/10.1089/dia.2015.0119.

[108] M. Legler, G. Brandenberger, B. Hietter, M. Siméoni, B. Reinhardt, Diurnal Cortisol Peaks and Their Relationships to Meals, J. Clin. Endocrinol. Metab. 55 (1982) 757–761. https://doi.org/10.1210/jcem-55-4-757.

[109] M. Gordic, Theoretical modeling of cortisol sensor, (2008) 71. http://scholarcommons.usf.edu/etdhttp://scholarcommons.usf.edu/etd/267 (accessed May 23, 2019).

[110] J.I. Prydal, P. Artal, H. Woon, F.W. Campbell, Study of human precorneal tear film thickness and structure using laser interferometry., Invest.

Ophthalmol. Vis. Sci. 33 (1992) 2006–11. http://www.ncbi.nlm.nih.gov/pubmed/1582805 (accessed June 3, 2019).

[111] S. Mishima, A. Gasset, S.D. Klyce, J.L. Baum, Determination of tear volume and tear flow, Invest. Ophthalmol. 5 (1966) 264–76. https://iovs.arvojournals.org/article.aspx?articleid=2203634 (accessed June 3, 2019).

[112] A.B. Watson, J.I. Yellott, A unified formula for light-adapted pupil size, J. Vis. 12 (2012) 12–12. https://doi.org/10.1167/12.10.12.

[113] E.S. Bennett, How important are lens oxygen ratings? They are one of many performance factors., Cornea. 9 Suppl 1 (1990) S4-7; discussion S8. http://www.ncbi.nlm.nih.gov/pubmed/2189679.

[114] C.R. Taormina, J.T. Baca, S.A. Asher, J.J. Grabowski, D.N. Finegold, Analysis of tear glucose concentration with electrospray ionization mass spectrometry, J. Am. Soc. Mass Spectrom. 18 (2007) 332–336. https://doi.org/10.1016/j.jasms.2006.10.002.

[115] G.L. Ackerman, Serum Sodium, 1990. http://www.ncbi.nlm.nih.gov/pubmed/21250148.

[116] D. Harvey, N.W. Hayes, B. Tighe, Fibre optics sensors in tear electrolyte analysis: Towards a novel point of care potassium sensor, Contact Lens Anterior Eye. 35 (2012) 137–144. https://doi.org/10.1016/j.clae.2012.02.004.

[117] D.A. Goldstein, Serum Calcium, 1990. http://www.ncbi.nlm.nih.gov/pubmed/21250094.

[118] W.B. Weglicki, Hypomagnesemia and Inflammation: Clinical and Basic Aspects, Annu. Rev. Nutr. 32 (2012) 55–71. https://doi.org/10.1146/annurev-nutr-071811-150656.

[119] H.A. de Morais, A.L. Leisewitz, Mixed Acid-Base Disorders, in: Fluid, Electrolyte, Acid-Base Disord. Small Anim. Pract., Elsevier, 2012: pp. 302–315. https://doi.org/10.1016/B978-1-4377-0654-3.00019-6.

[120] Á. Farkas, R. Vámos, T. Bajor, N. Müllner, Á. Lázár, A. Hrabá, Utilization of lacrimal urea assay in the monitoring of hemodialysis: conditions, limitations and lacrimal arginase characterization, Exp. Eye Res. 76 (2003) 183–192.

https://doi.org/10.1016/S0014-4835(02)00276-2.

[121] W.-M. Zhang, M.R. Natowicz, Cerebrospinal fluid lactate and pyruvate concentrations and their ratio, Clin. Biochem. 46 (2013) 694–697. https://doi.org/10.1016/j.clinbiochem.2012.11.008.

[122] L. Stankova, M. Riddle, J. Larned, K. Burry, D. Menashe, J. Hart, R. Bigley, Plasma ascorbate concentrations and blood cell dehydroascorbate transport in patients with diabetes mellitus, Metabolism. 33 (1984) 347–353. https://doi.org/10.1016/0026-0495(84)90197-5.

[123] C.A. Paterson, M.C. O'Rourke, Vitamin C Levels in Human Tears, Arch. Ophthalmol. 105 (1987) 376–377. https://doi.org/10.1001/archopht.1987.01060030096034.

[124] Y. Ohashi, M. Dogru, K. Tsubota, Laboratory findings in tear fluid analysis, Clin. Chim. Acta. 369 (2006) 17–28. https://doi.org/10.1016/j.cca.2005.12.035.

[125] G. Runström, A. Mann, B. Tighe, The Fall and Rise of Tear Albumin Levels: A Multifactorial Phenomenon, Ocul. Surf. 11 (2013) 165–180. https://doi.org/10.1016/j.jtos.2013.03.001.

[126] J.R. Sempionatto, L.C. Brazaca, L. García-Carmona, G. Bolat, A.S. Campbell, A. Martin, G. Tang, R. Shah, R.K. Mishra, J. Kim, V. Zucolotto, A. Escarpa, J. Wang, Eyeglasses-based tear biosensing system: Non-invasive detection of alcohol, vitamins and glucose, Biosens. Bioelectron. 137 (2019) 161–170. https://doi.org/10.1016/j.bios.2019.04.058.

9 Appendices

9.1 Lag/Bias Corrected Test Sets (Chapter 5)

CGM Data: Lag/Bias Reconstruction

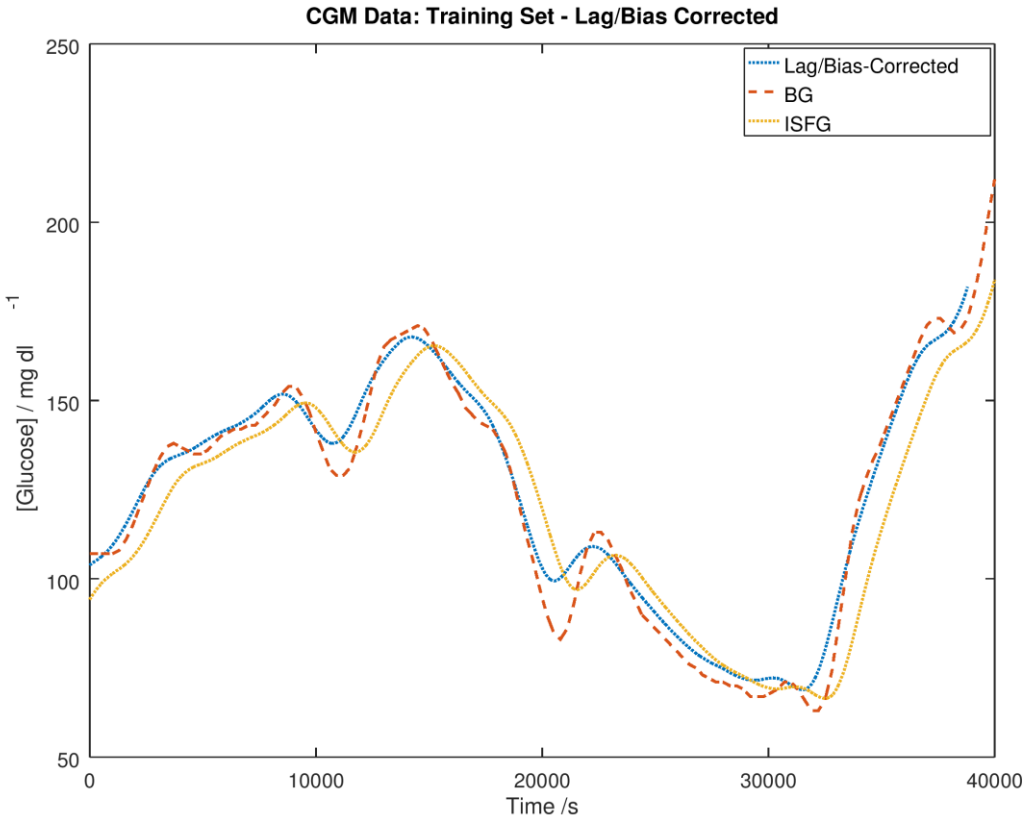

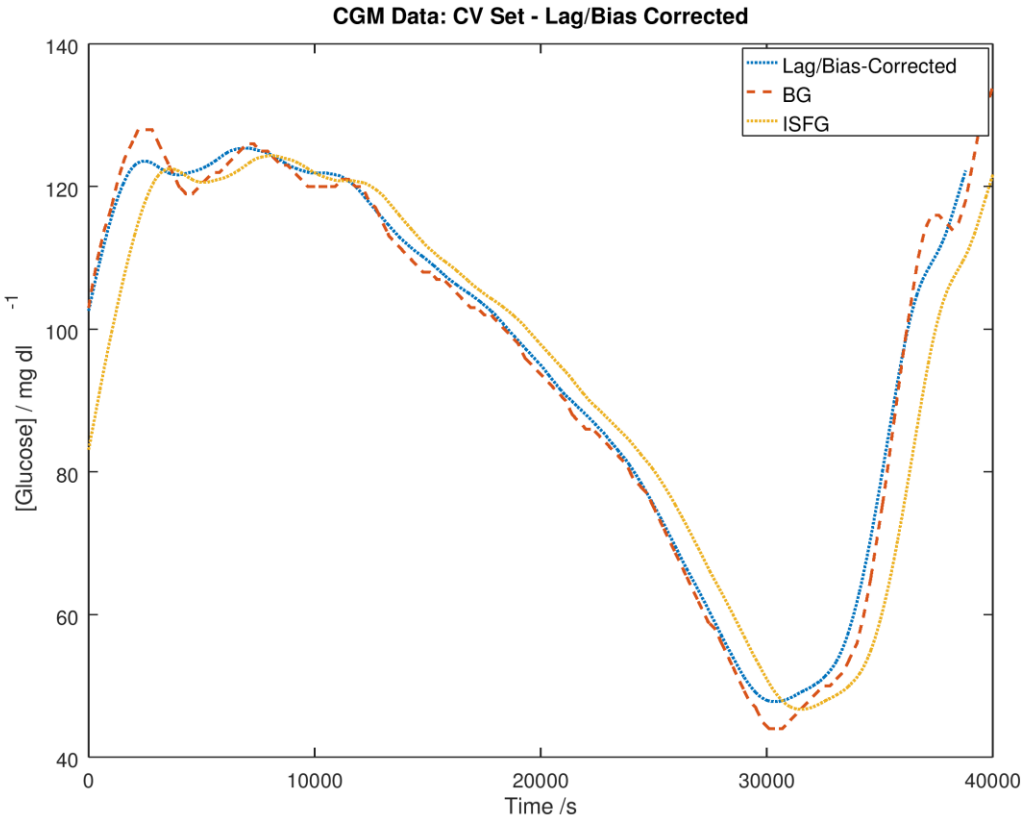
CGM Data: CV Set - Lag/Bias Corrected
Lag/Bias-Corrected
BG
ISFG
[Glucose] / mg dl -1
Time /s
140
120
100
80
60
40
0
10000
20000
30000
40000

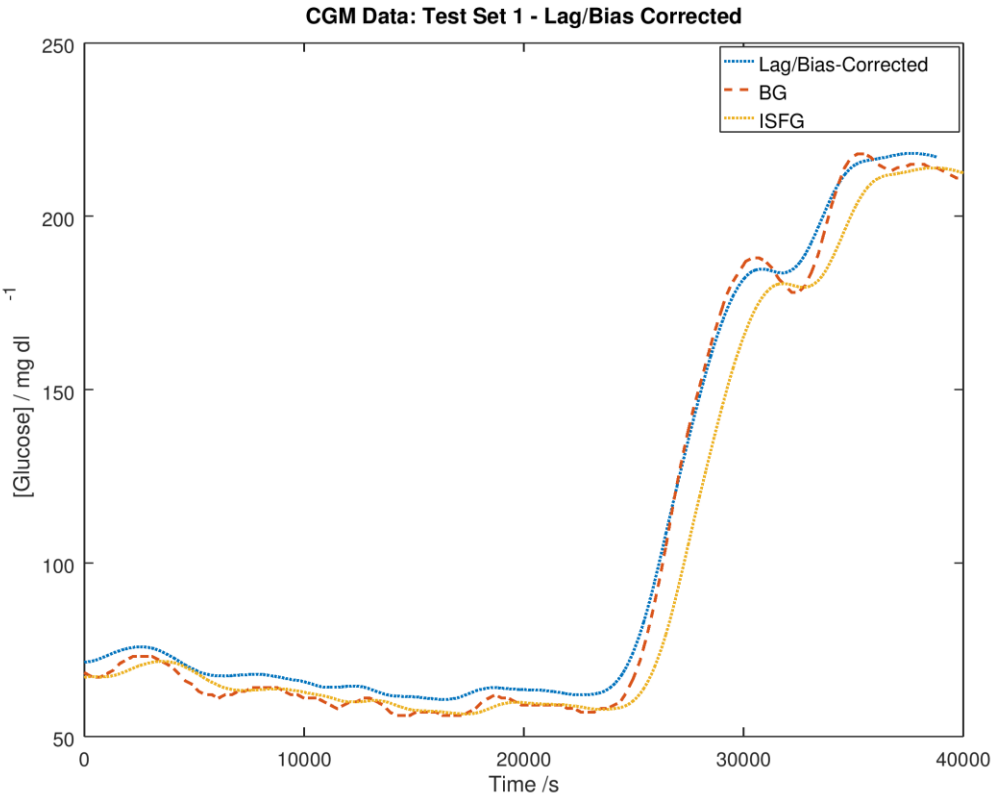
CGM Data: Test Set 1 - Lag/Bias Corrected
Lag/Bias-Corrected
BG
ISFG
[Glucose] / mg dl -1
Time /s
250
200
150
100
50
0
10000
20000
30000
40000

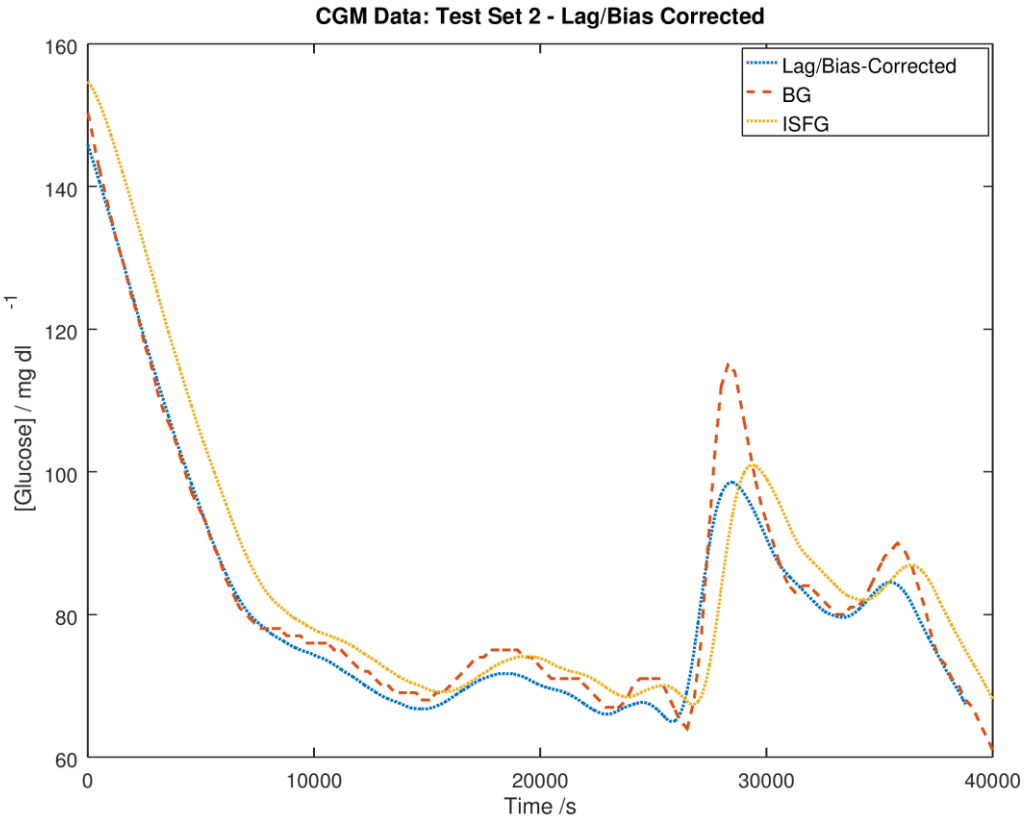
CGM Data: Test Set 2 - Lag/Bias Corrected
Lag/Bias-Corrected
BG
ISFG
[Glucose] / mg dl -1
Time /s
160
140
120
100
80
60
0
10000
20000
30000
40000

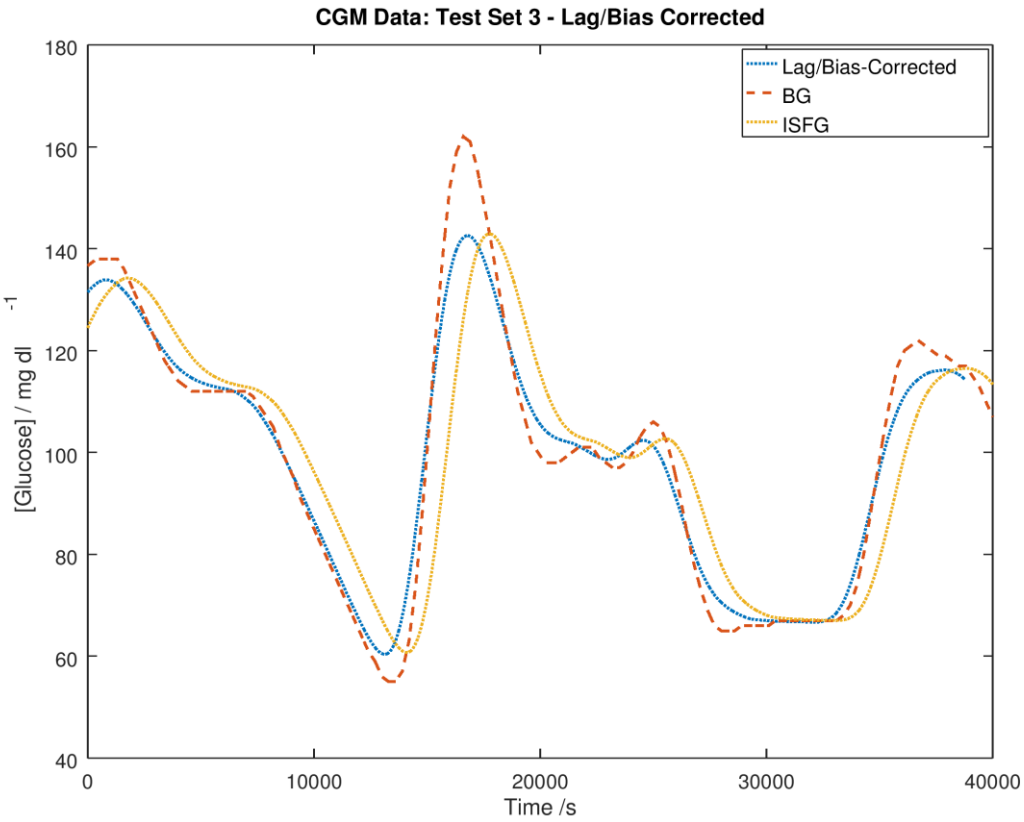
CGM Data: Test Set 3 - Lag/Bias Corrected
Lag/Bias-Corrected
BG
ISFG
[Glucose] / mg dl -1
Time /s
180
160
140
120
100
80
60
40
0
10000
20000
30000
40000

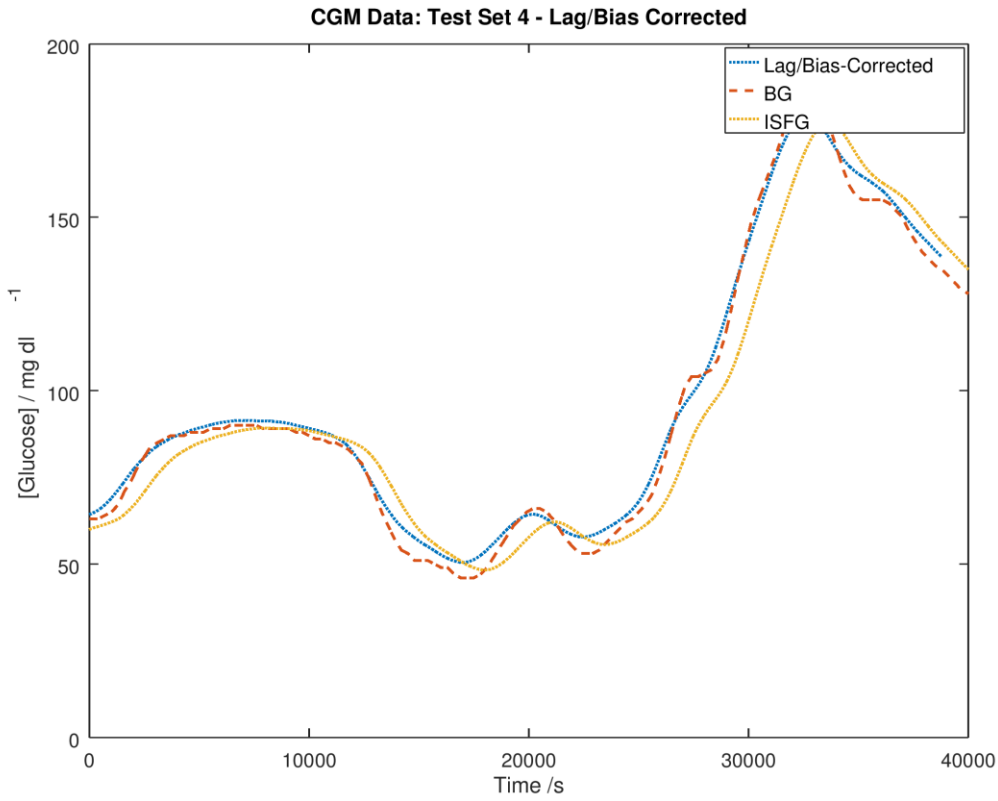
CGM Data: Test Set 4 - Lag/Bias Corrected
Lag/Bias-Corrected
BG
ISFG
[Glucose] / mg dl -1
Time /s
0
50
100
150
200
0
10000
20000
30000
40000

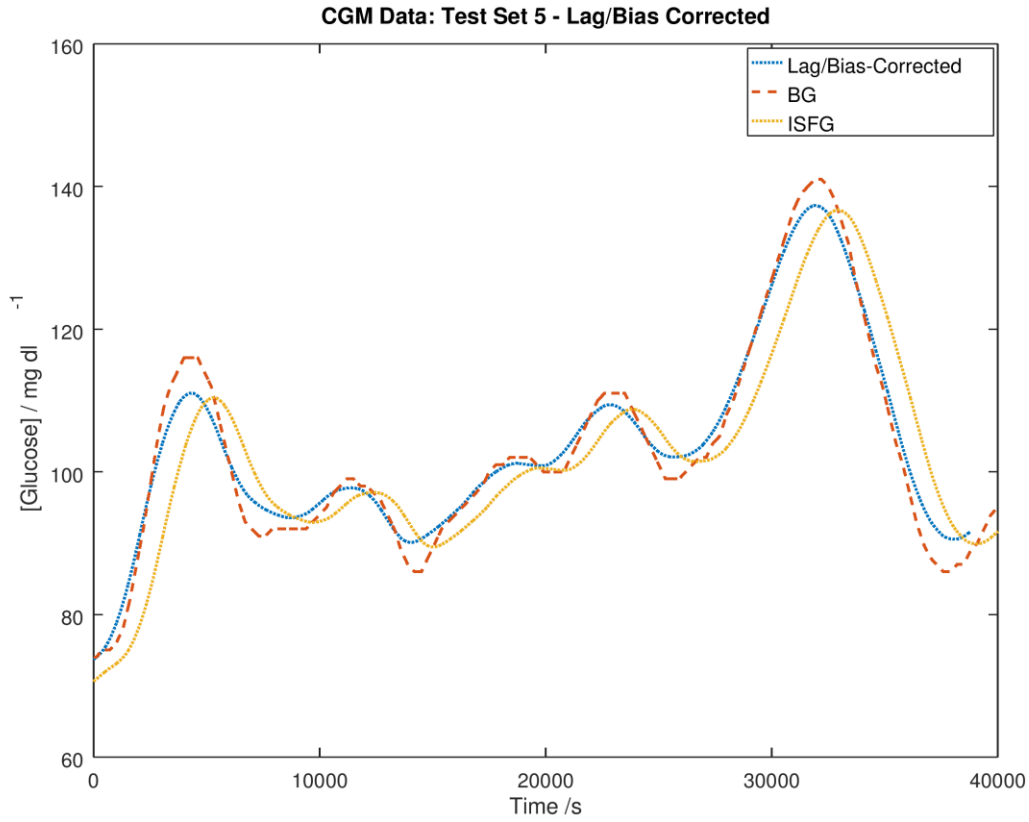
CGM Data: Test Set 5 - Lag/Bias Corrected
Lag/Bias-Corrected
BG
ISFG
[Glucose] / mg dl -1
Time /s
60
80
100
120
140
160
0
10000
20000
30000
40000

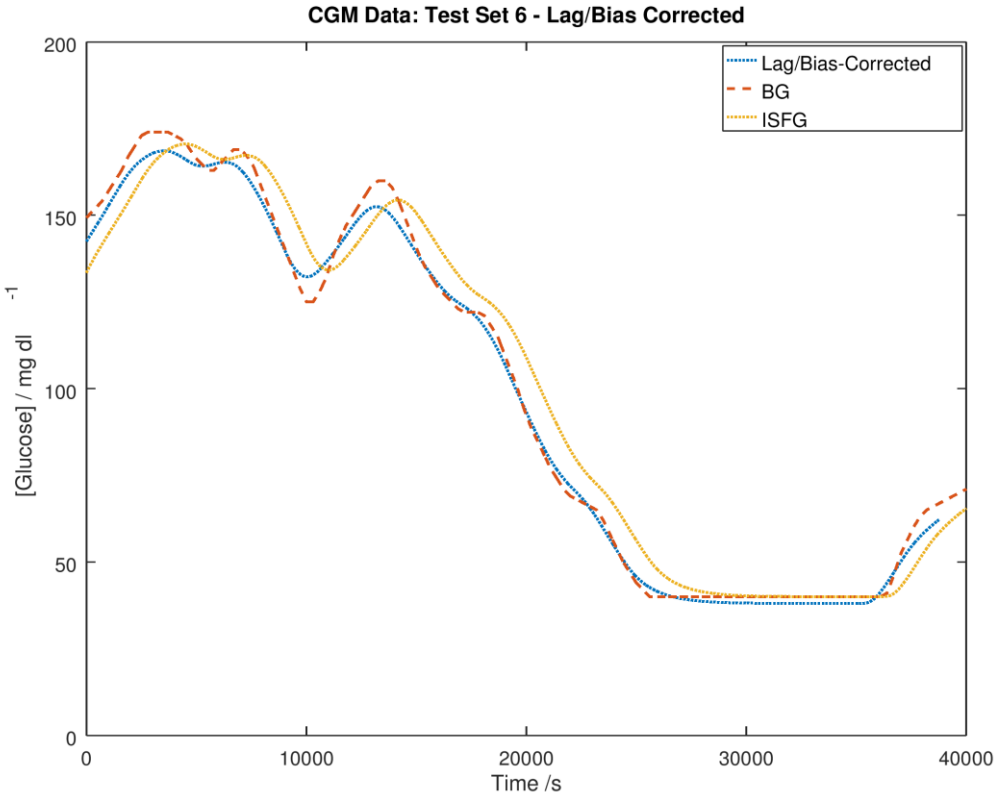
CGM Data: Test Set 6 - Lag/Bias Corrected
Lag/Bias-Corrected
BG
ISFG
[Glucose] / mg dl -1
Time /s
0
50
100
150
200
0
10000
20000
30000
40000

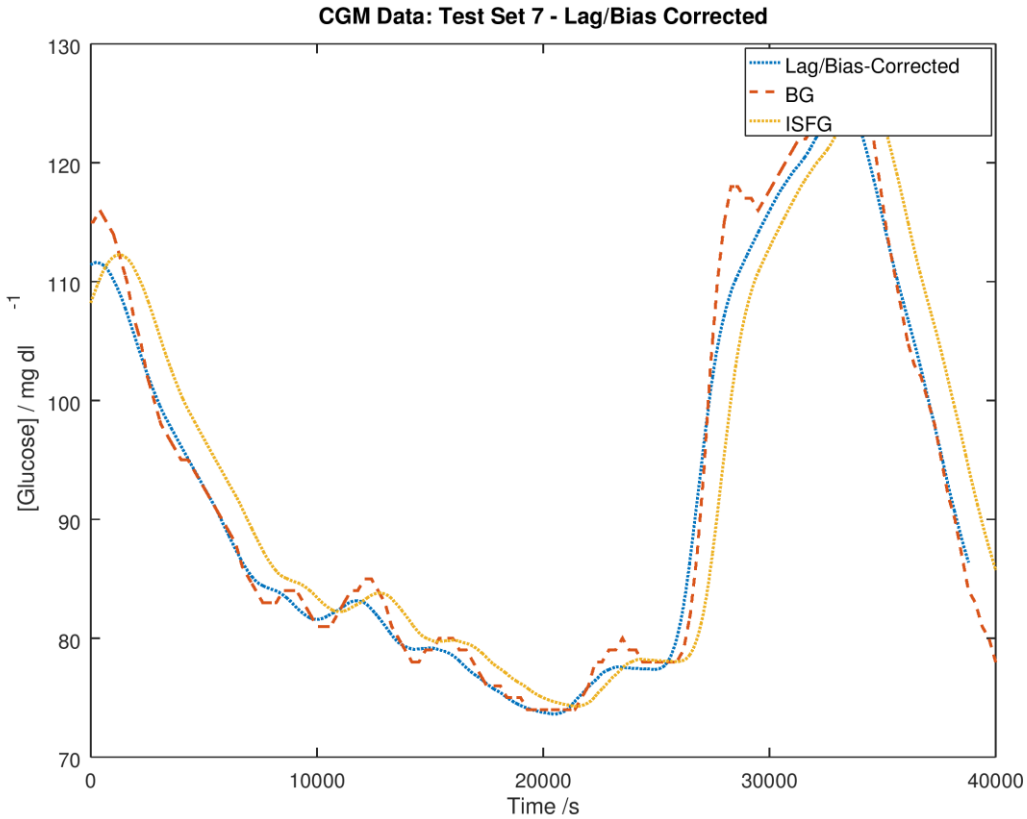
CGM Data: Test Set 7 - Lag/Bias Corrected
Lag/Bias-Corrected
BG
ISFG
[Glucose] / mg dl -1
Time /s
70
80
90
100
110
120
130
0
10000
20000
30000
40000

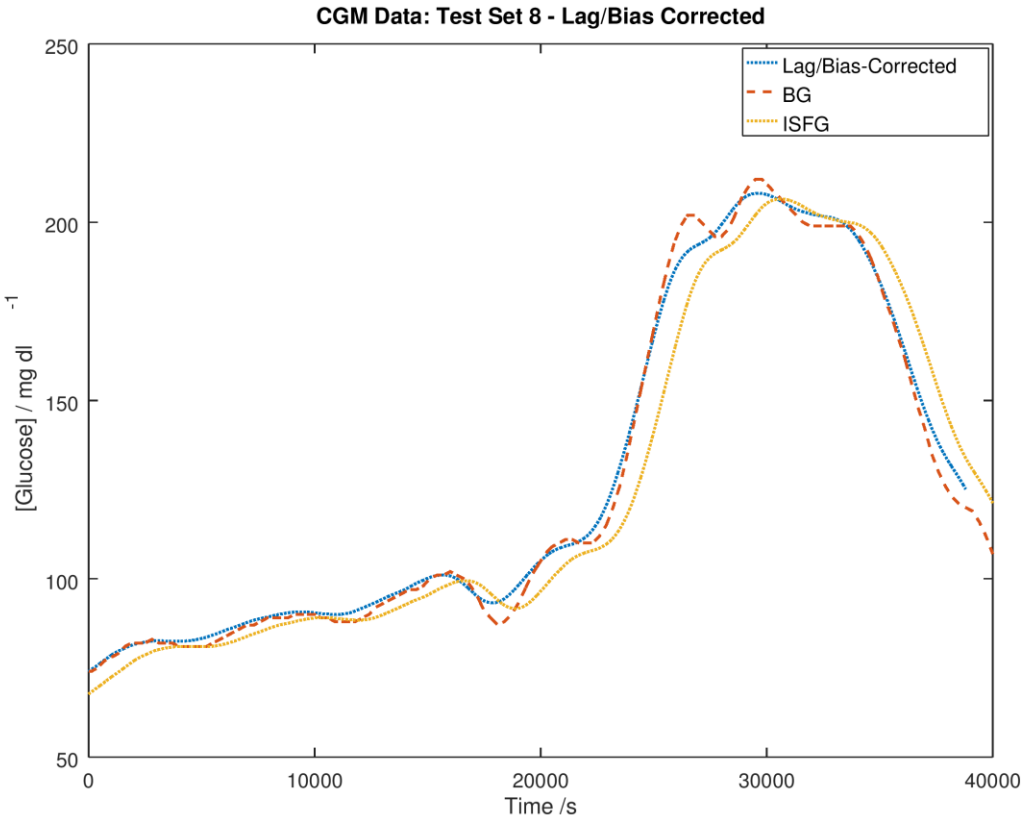
CGM Data: Test Set 8 - Lag/Bias Corrected
Lag/Bias-Corrected
BG
ISFG
[Glucose] / mg dl -1
Time /s
250
200
150
100
50
0
10000
20000
30000
40000

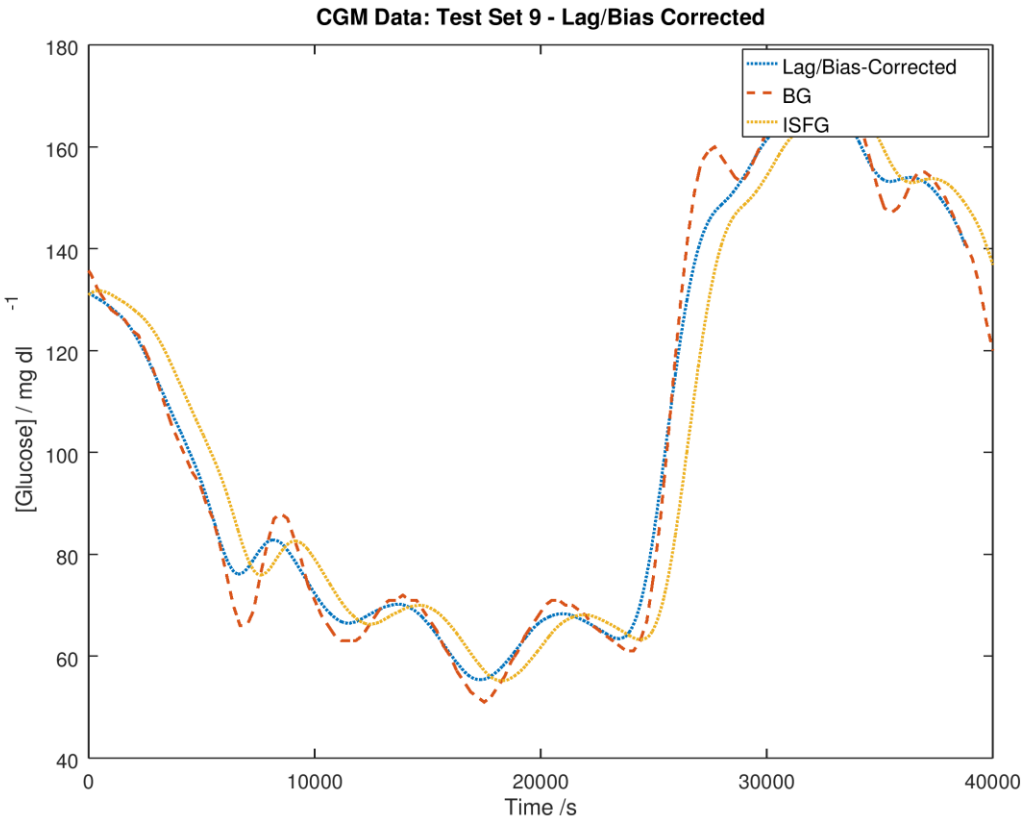
CGM Data: Test Set 9 - Lag/Bias Corrected
Lag/Bias-Corrected
BG
ISFG
[Glucose] / mg dl -1
Time /s
180
160
140
120
100
80
60
40
0
10000
20000
30000
40000

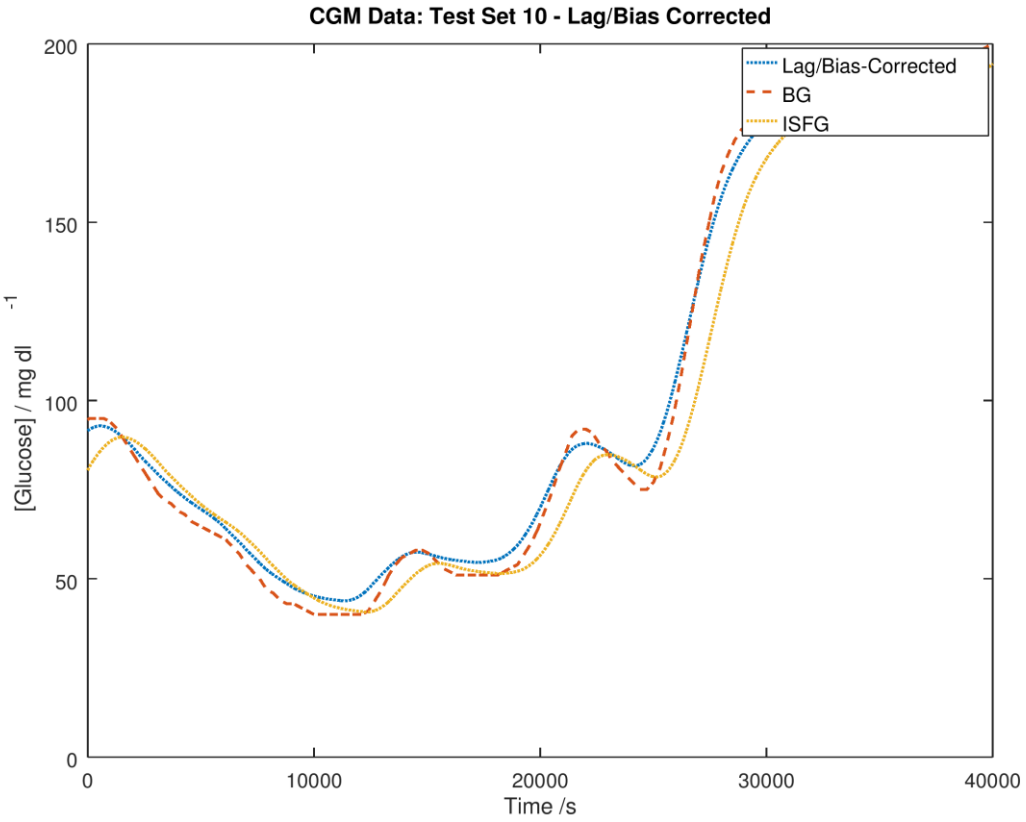
CGM Data: Test Set 10 - Lag/Bias Corrected
Lag/Bias-Corrected
BG
ISFG
[Glucose] / mg dl -1
Time /s
0
50
100
150
200
0
10000
20000
30000
40000

Simulated Data: Lag/Bias Reconstruction

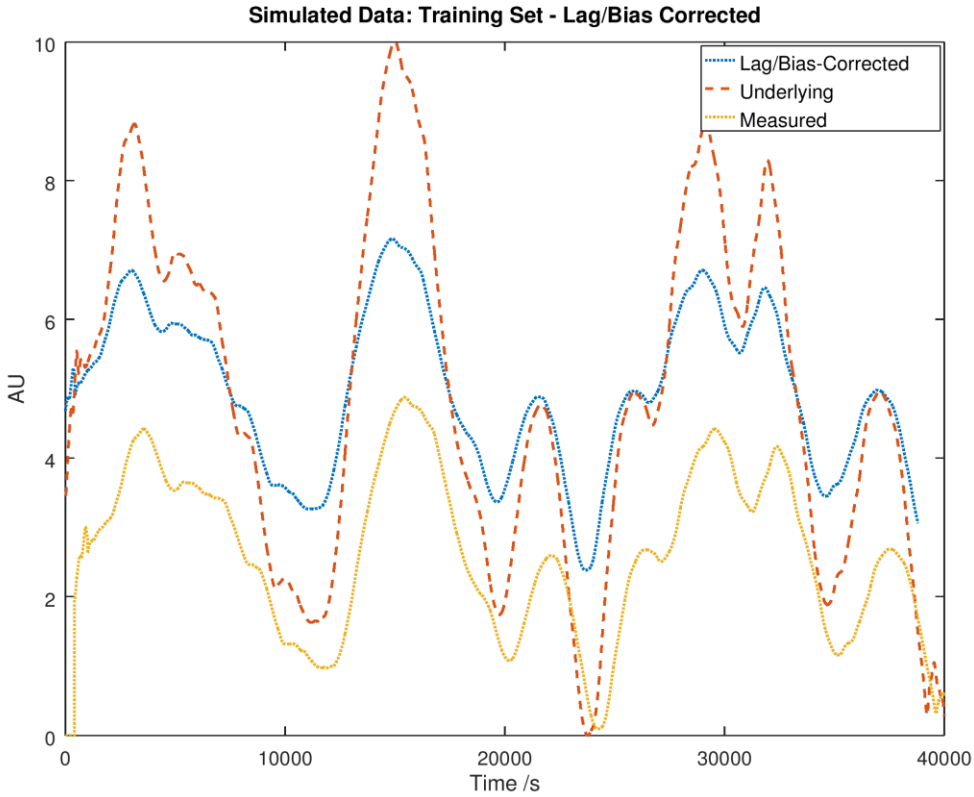

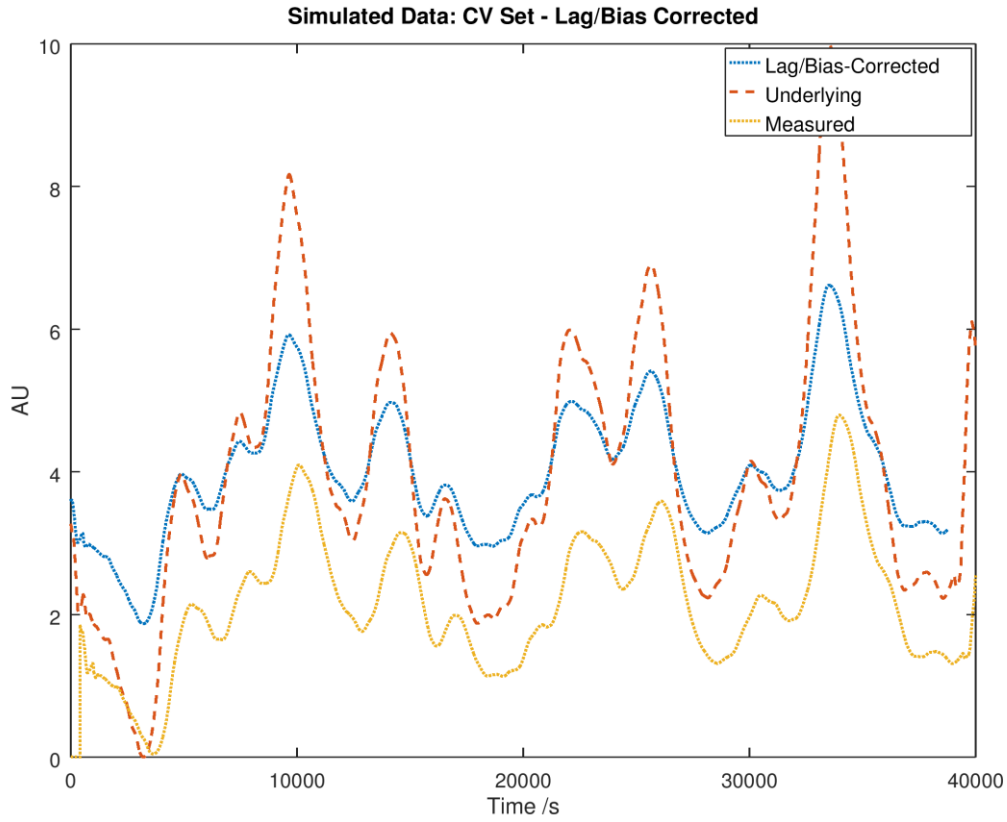
Simulated Data: CV Set - Lag/Bias Corrected
Lag/Bias-Corrected
Underlying
Measured
AU
Time /s
0
2
4
6
8
10
0
10000
20000
30000
40000

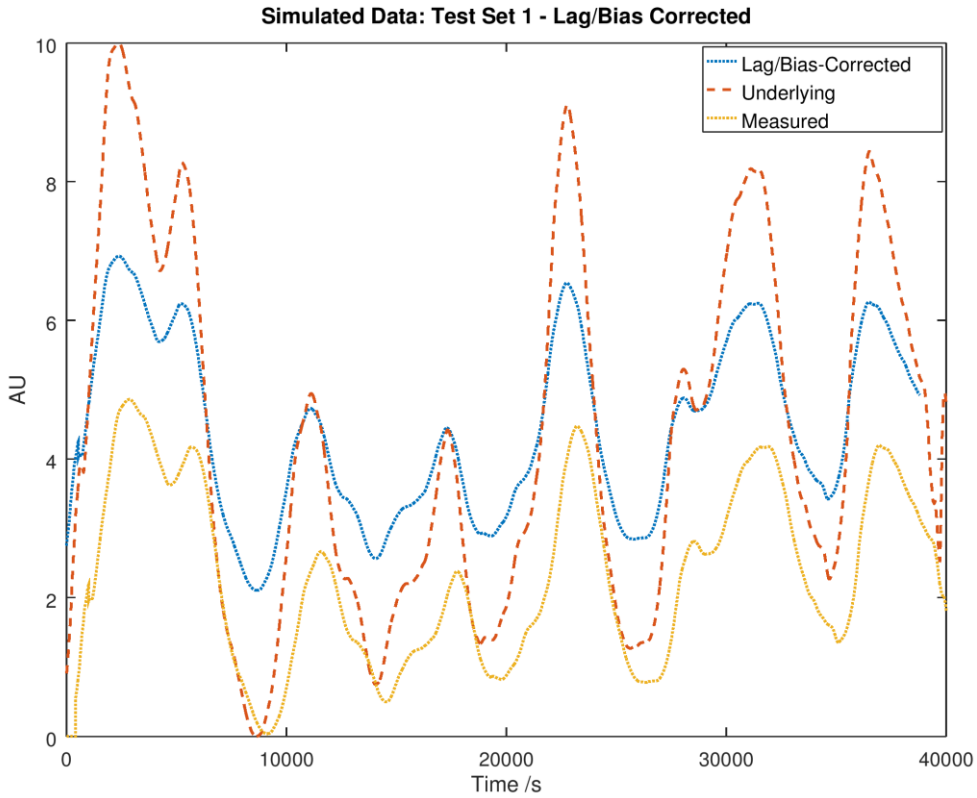
Simulated Data: Test Set 1 - Lag/Bias Corrected
Lag/Bias-Corrected
Underlying
Measured
AU
Time /s
0
2
4
6
8
10
0
10000
20000
30000
40000

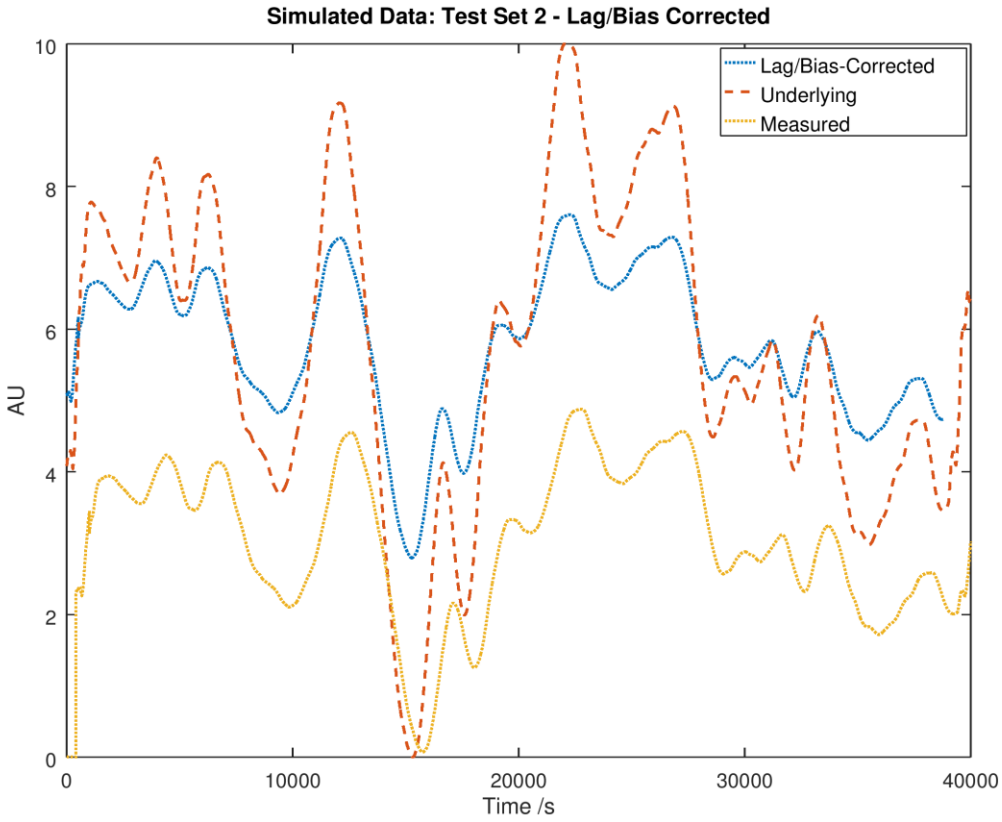
Simulated Data: Test Set 2 - Lag/Bias Corrected
Lag/Bias-Corrected
Underlying
Measured
AU
Time /s
0
2
4
6
8
10
0
10000
20000
30000
40000

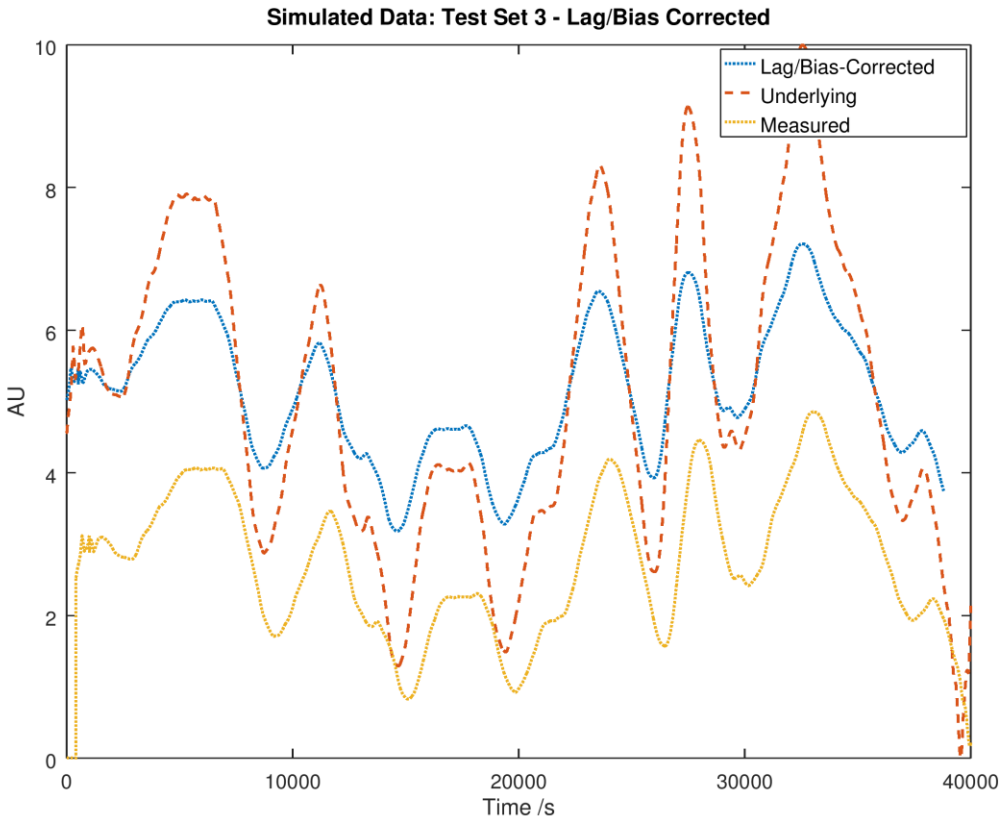
Simulated Data: Test Set 3 - Lag/Bias Corrected
Lag/Bias-Corrected
Underlying
Measured
AU
Time /s
0
2
4
6
8
10
0
10000
20000
30000
40000

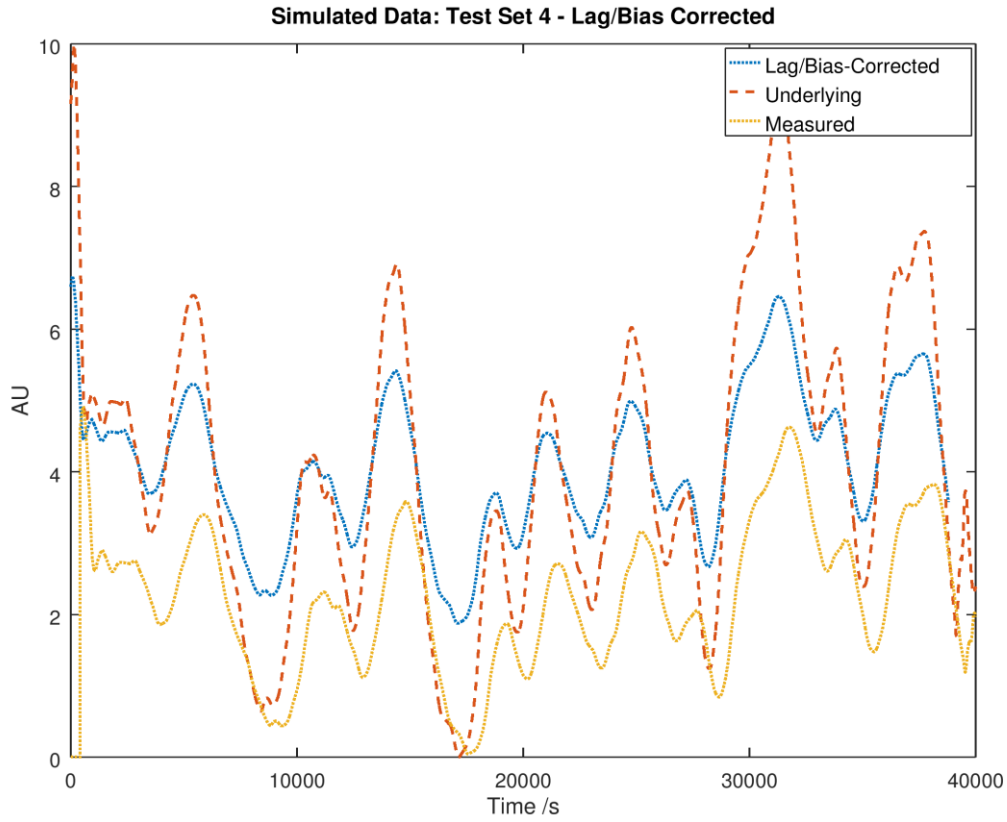
Simulated Data: Test Set 4 - Lag/Bias Corrected
Lag/Bias-Corrected
Underlying
Measured
AU
Time /s
0
2
4
6
8
10
0
10000
20000
30000
40000

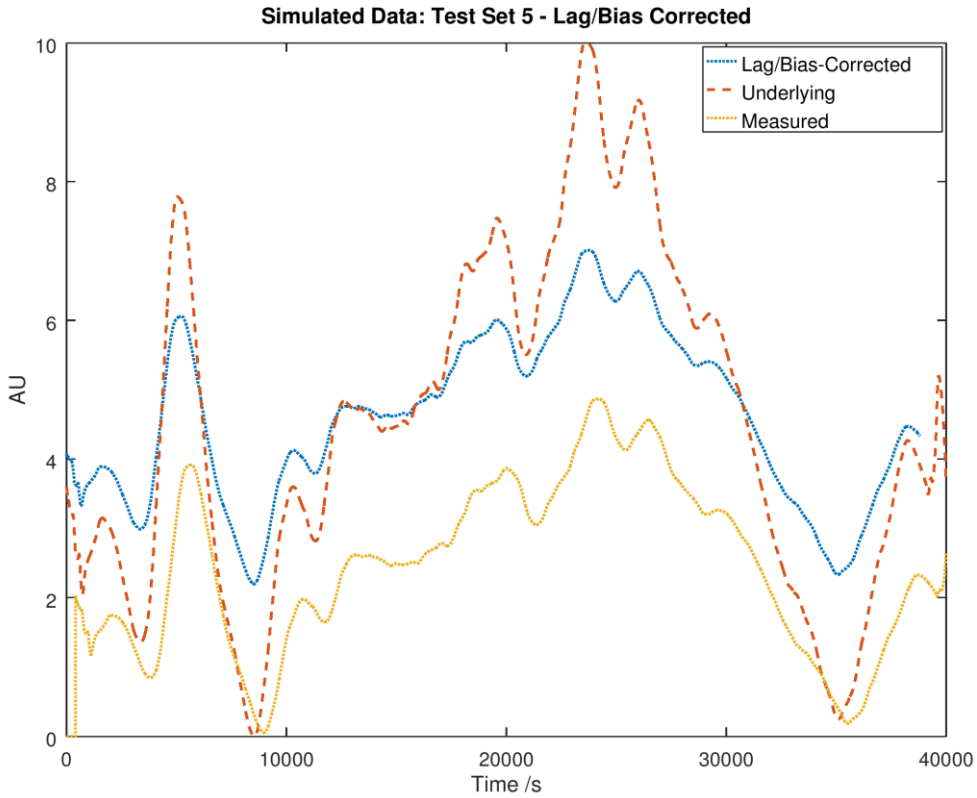
Simulated Data: Test Set 5 - Lag/Bias Corrected
Lag/Bias-Corrected
Underlying
Measured
AU
Time /s
0
2
4
6
8
10
0
10000
20000
30000
40000

9.2 Additional Test Sets (Chapter 5)

CGM Data: Neural Network Reconstruction

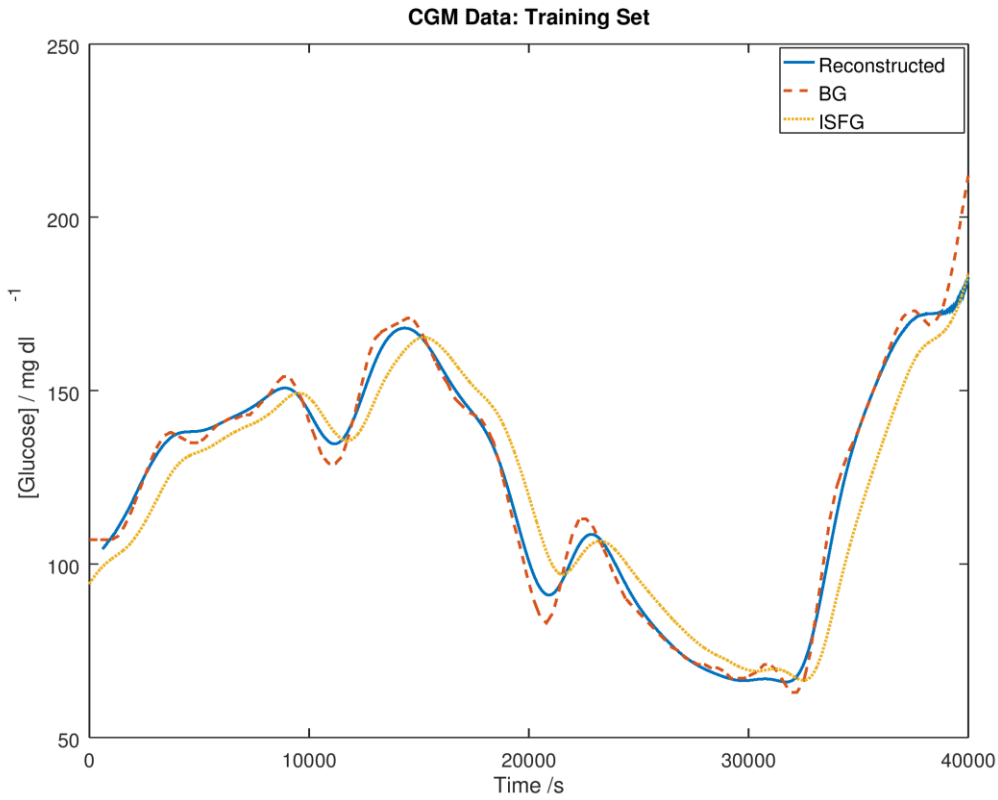

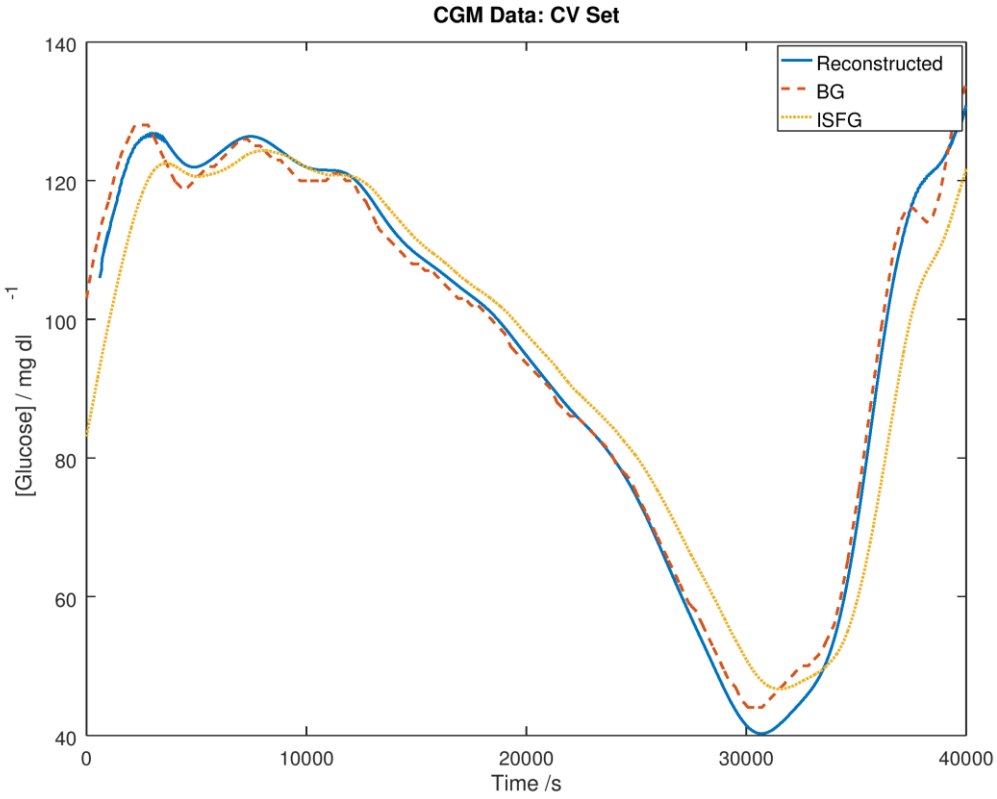
CGM Data: CV Set
Reconstructed
BG
ISFG
[Glucose] / mg dl -1
Time /s
140
120
100
80
60
40
0
10000
20000
30000
40000

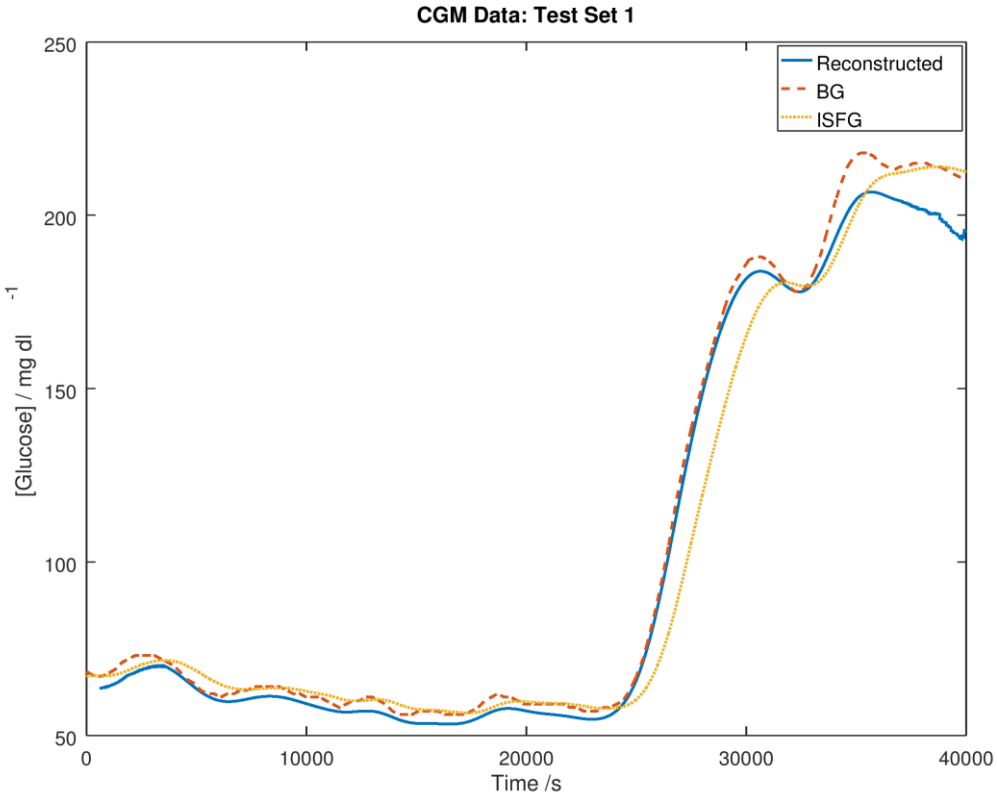
CGM Data: Test Set 1
Reconstructed
BG
ISFG
[Glucose] / mg dl -1
Time /s
250
200
150
100
50
0
10000
20000
30000
40000

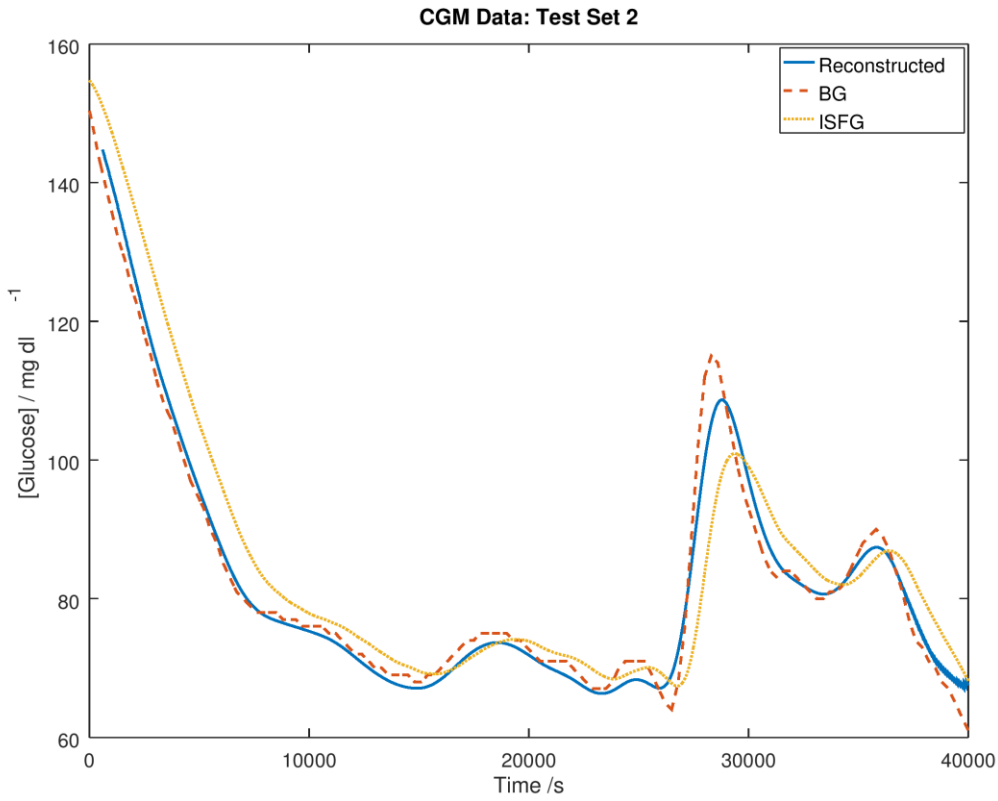
CGM Data: Test Set 2
Reconstructed
BG
ISFG
[Glucose] / mg dl -1
Time /s
160
140
120
100
80
60
0
10000
20000
30000
40000

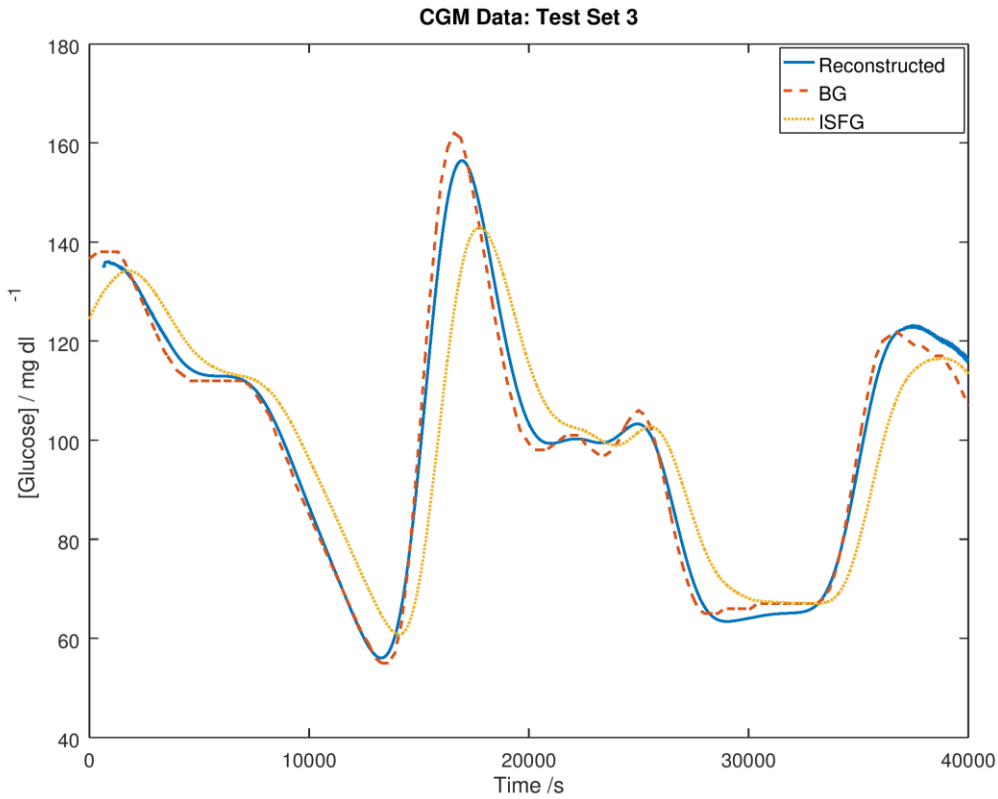
CGM Data: Test Set 3
Reconstructed
BG
ISFG
[Glucose] / mg dl -1
Time /s
180
160
140
120
100
80
60
40
0
10000
20000
30000
40000

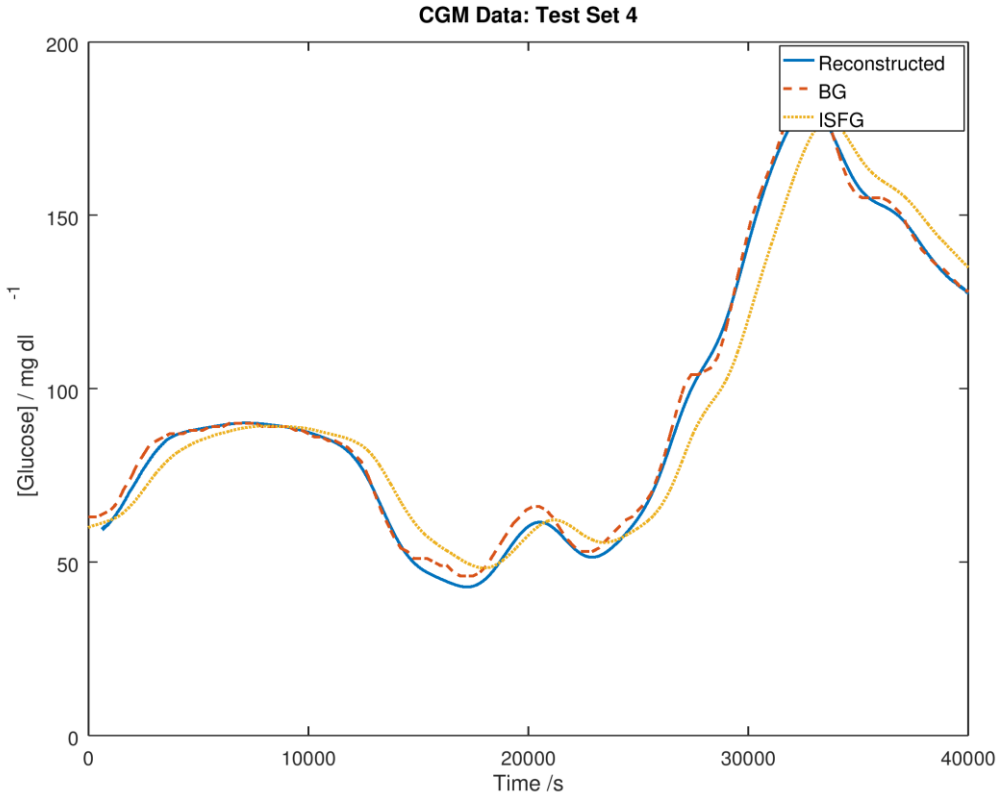
CGM Data: Test Set 4
Reconstructed
BG
ISFG
[Glucose] / mg dl -1
Time /s
0
50
100
150
200
0
10000
20000
30000
40000

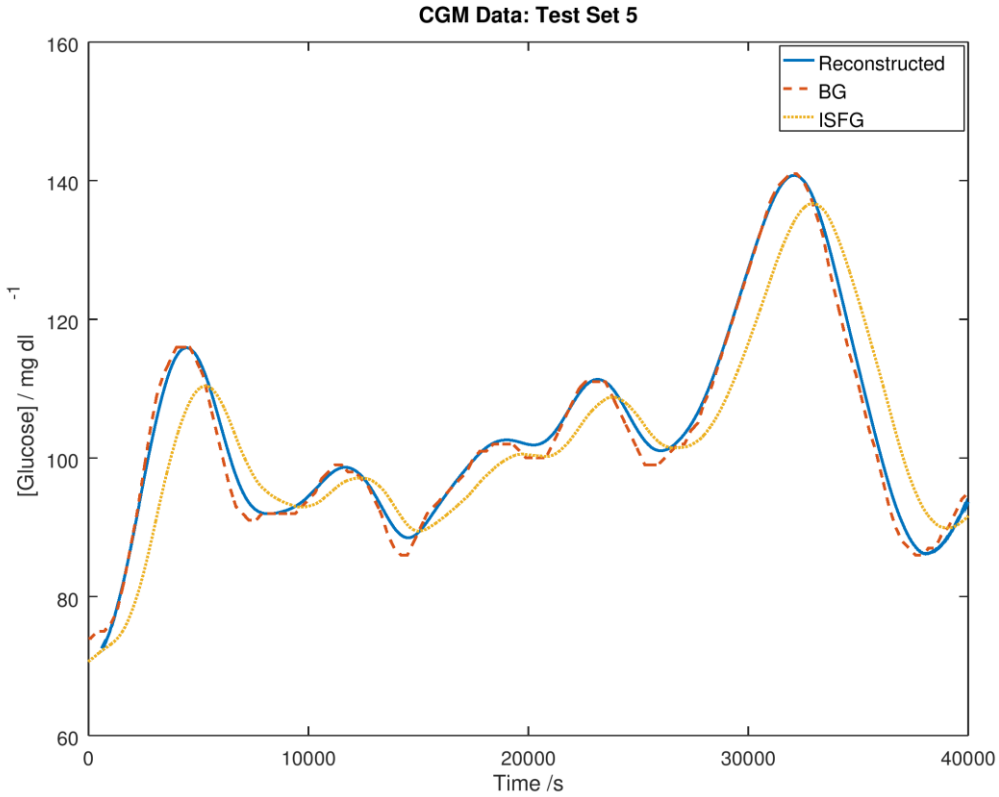
CGM Data: Test Set 5
Reconstructed
BG
ISFG
[Glucose] / mg dl -1
Time /s
60
80
100
120
140
160
0
10000
20000
30000
40000

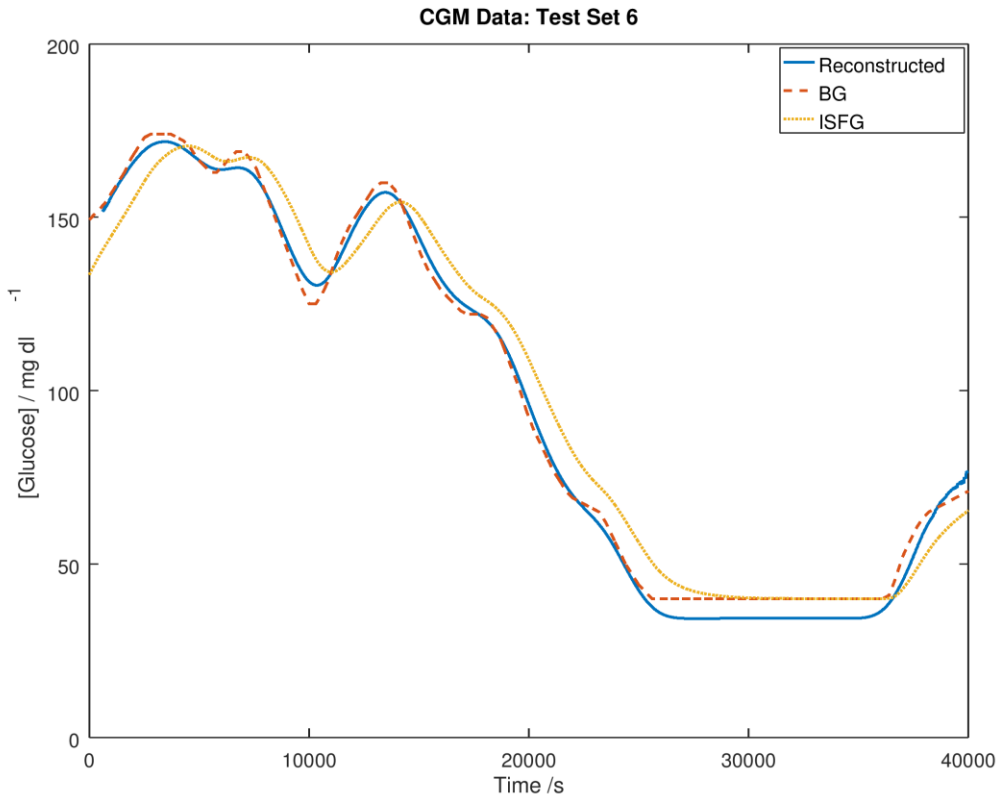
CGM Data: Test Set 6
Reconstructed
BG
ISFG
[Glucose] / mg dl -1
Time /s
0
50
100
150
200
0
10000
20000
30000
40000

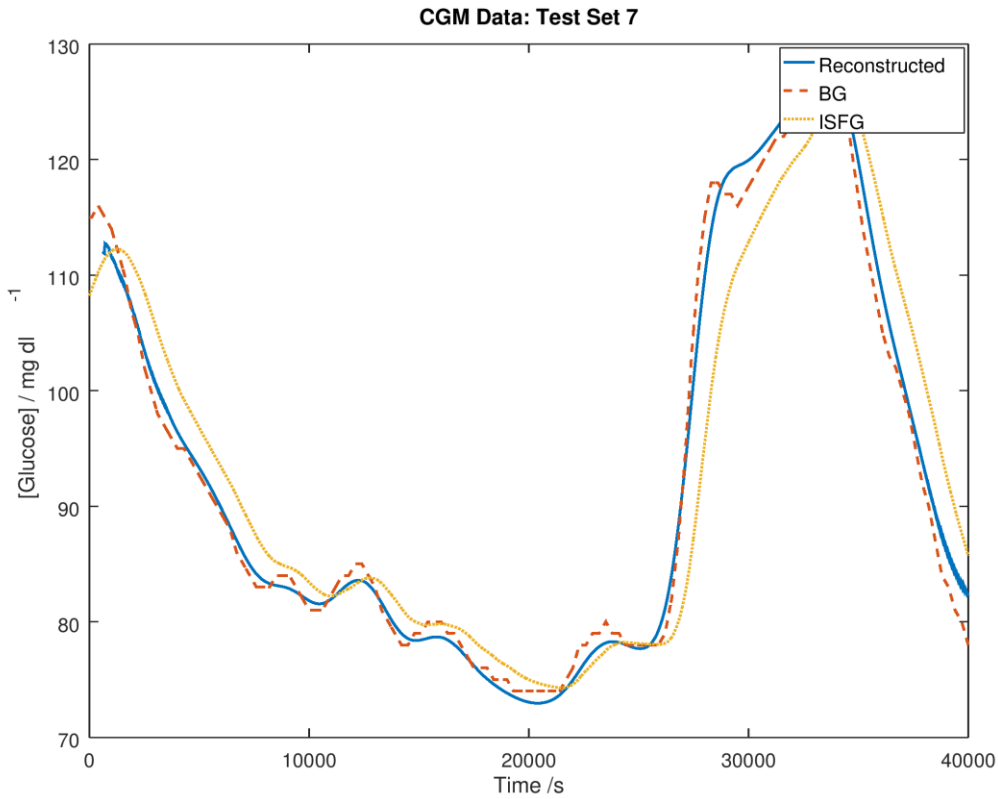
CGM Data: Test Set 7
Reconstructed
BG
ISFG
[Glucose] / mg dl -1
Time /s
70
80
90
100
110
120
130
0
10000
20000
30000
40000

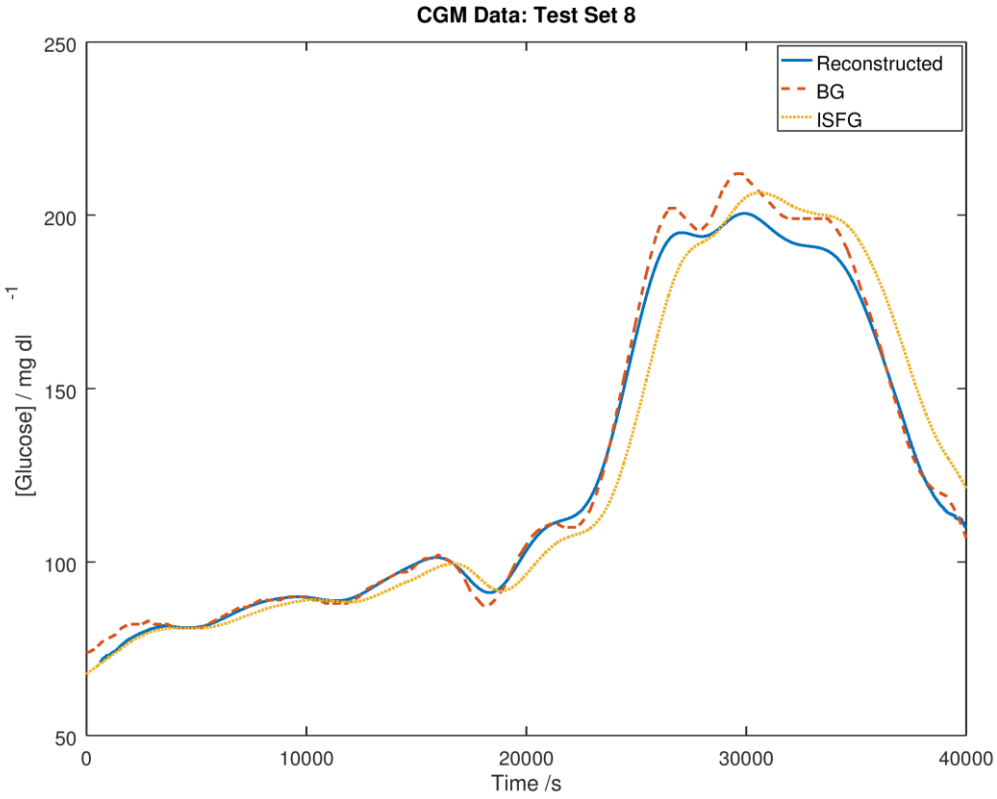
CGM Data: Test Set 8
Reconstructed
BG
ISFG
250
200
150
100
50
[Glucose] / mg dl -1
0
10000
20000
30000
40000
Time /s

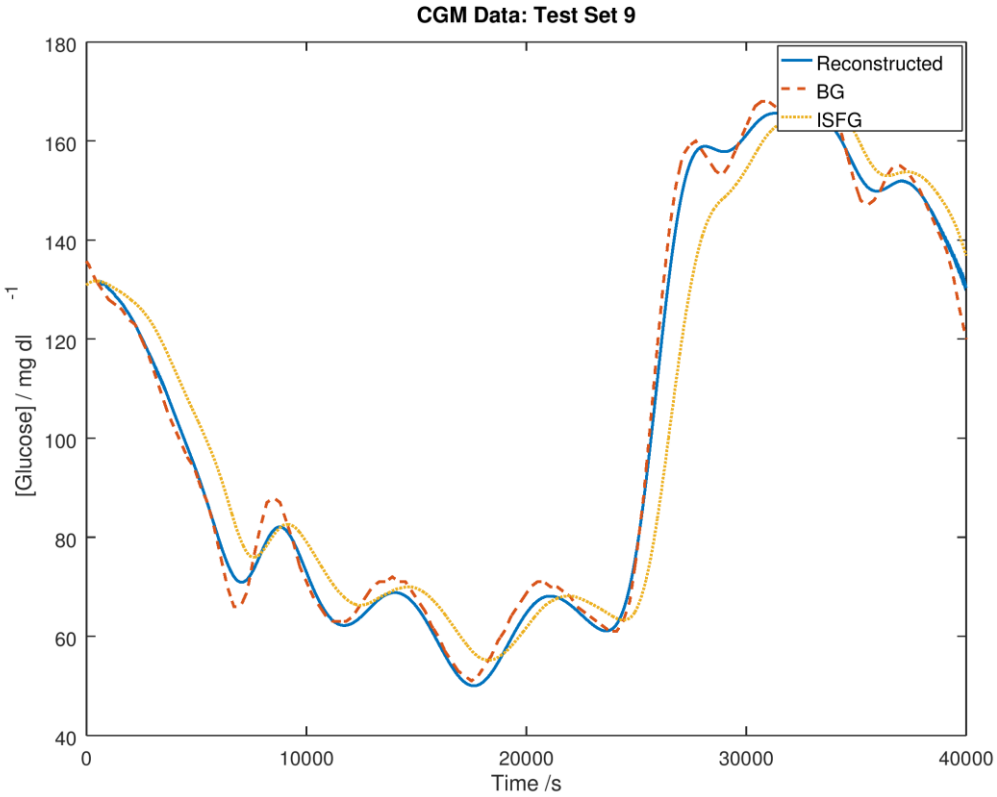
CGM Data: Test Set 9
Reconstructed
BG
ISFG
180
160
140
120
100
80
60
40
[Glucose] / mg dl -1
0
10000
20000
30000
40000
Time /s

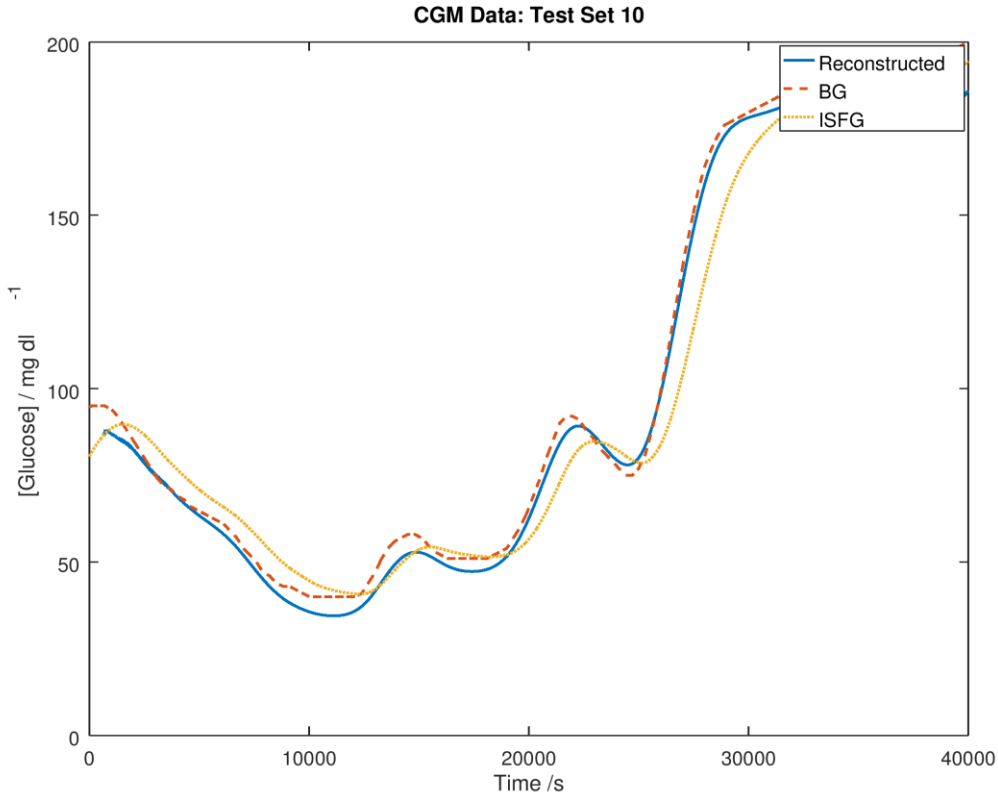
CGM Data: Test Set 10
Reconstructed
BG
ISFG
[Glucose] / mg dl -1
Time /s
0
50
100
150
200
0
10000
20000
30000
40000

Simulated Data: Neural Network Reconstruction

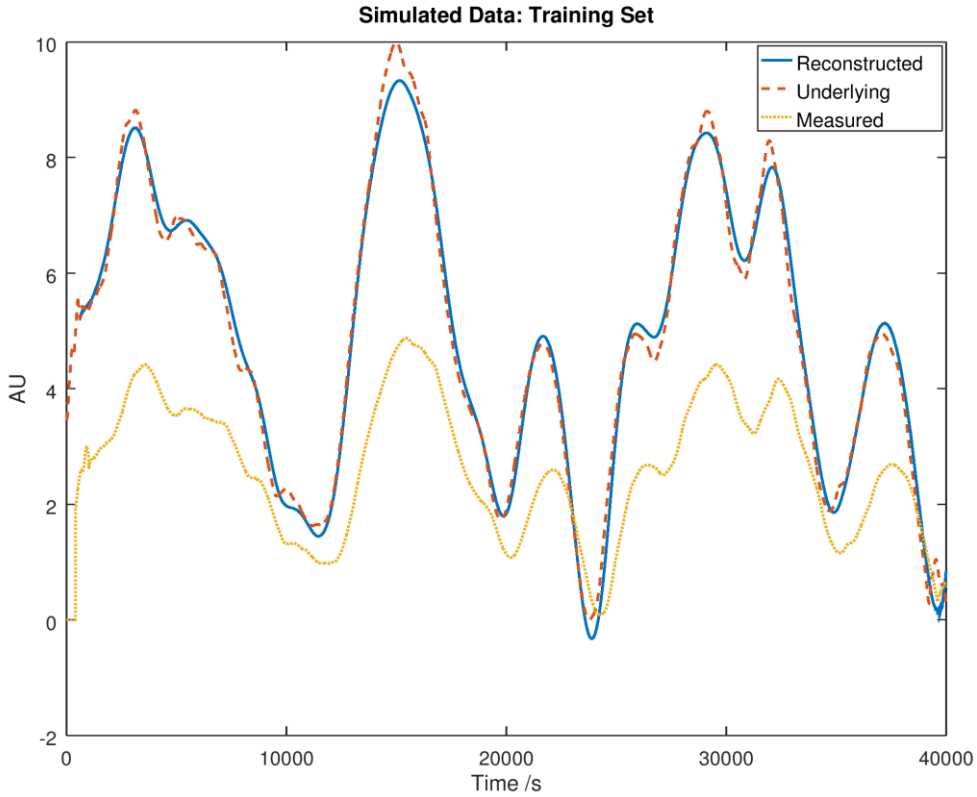

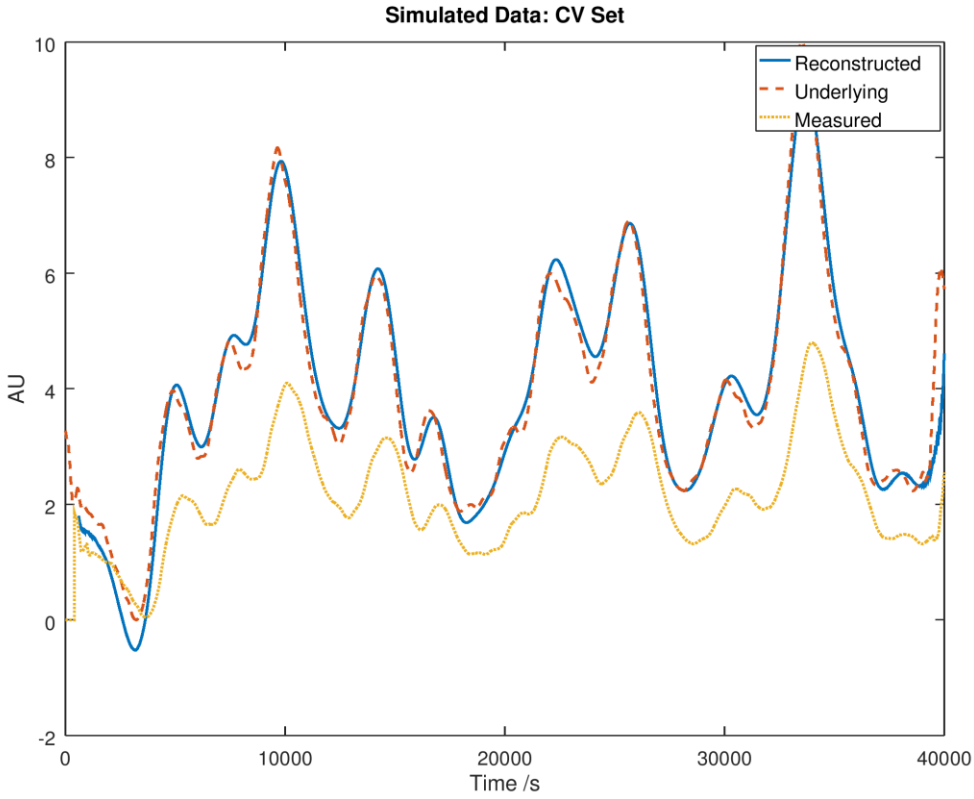
Simulated Data: CV Set
Reconstructed
Underlying
Measured
AU
Time /s
10
8
6
4
2
0
-2
0
10000
20000
30000
40000

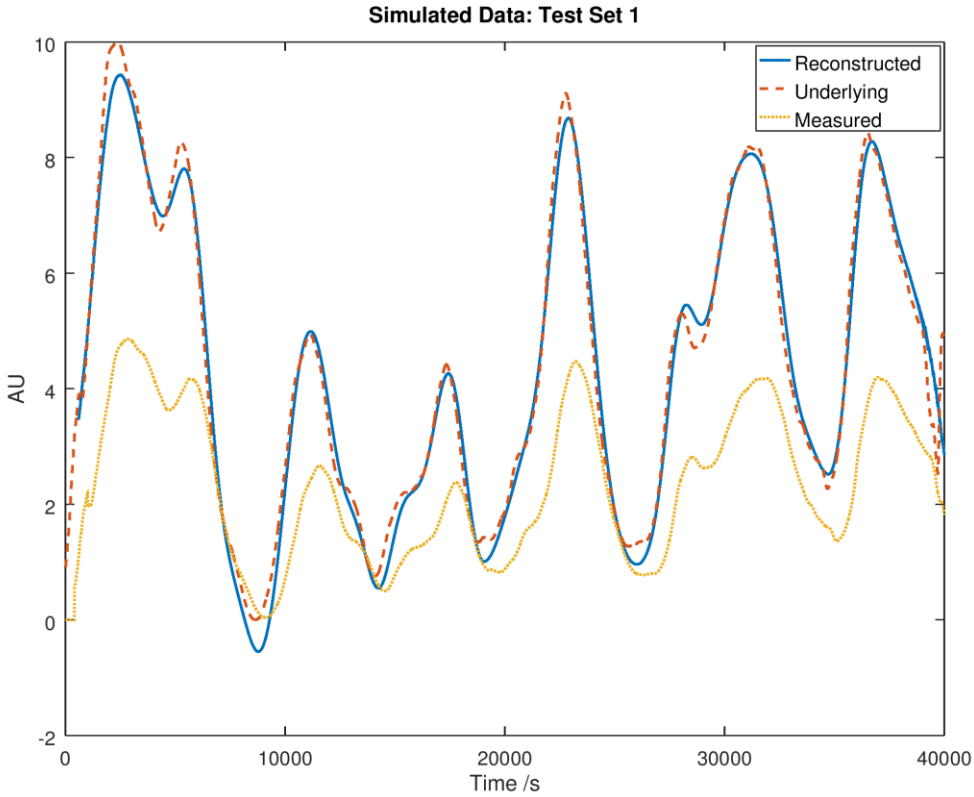
Simulated Data: Test Set 1
Reconstructed
Underlying
Measured
AU
Time /s
10
8
6
4
2
0
-2
0
10000
20000
30000
40000

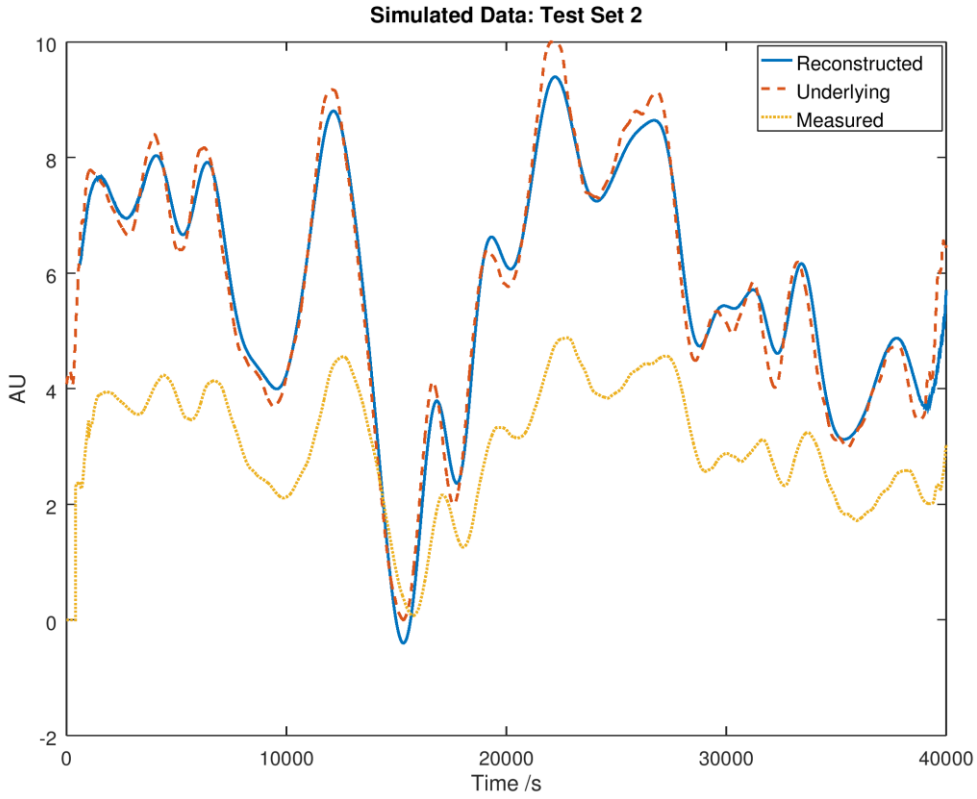
Simulated Data: Test Set 2
Reconstructed
Underlying
Measured
AU
Time /s
10
8
6
4
2
0
-2
0
10000
20000
30000
40000

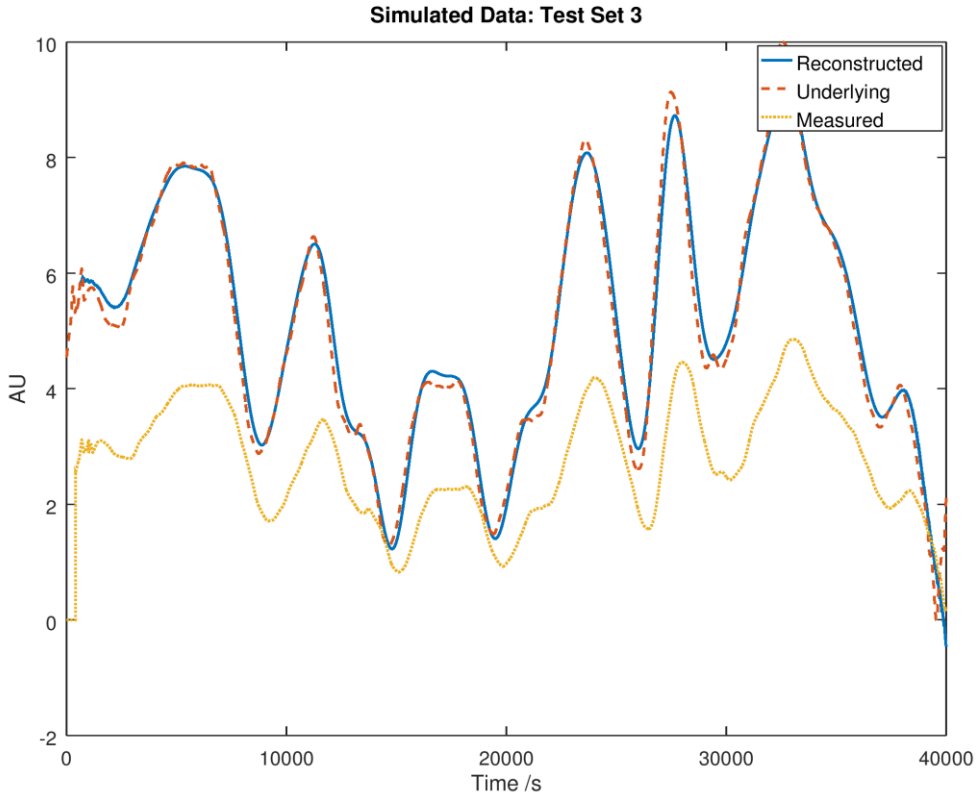
Simulated Data: Test Set 3
Reconstructed
Underlying
Measured
AU
Time /s
10
8
6
4
2
0
-2
0
10000
20000
30000
40000

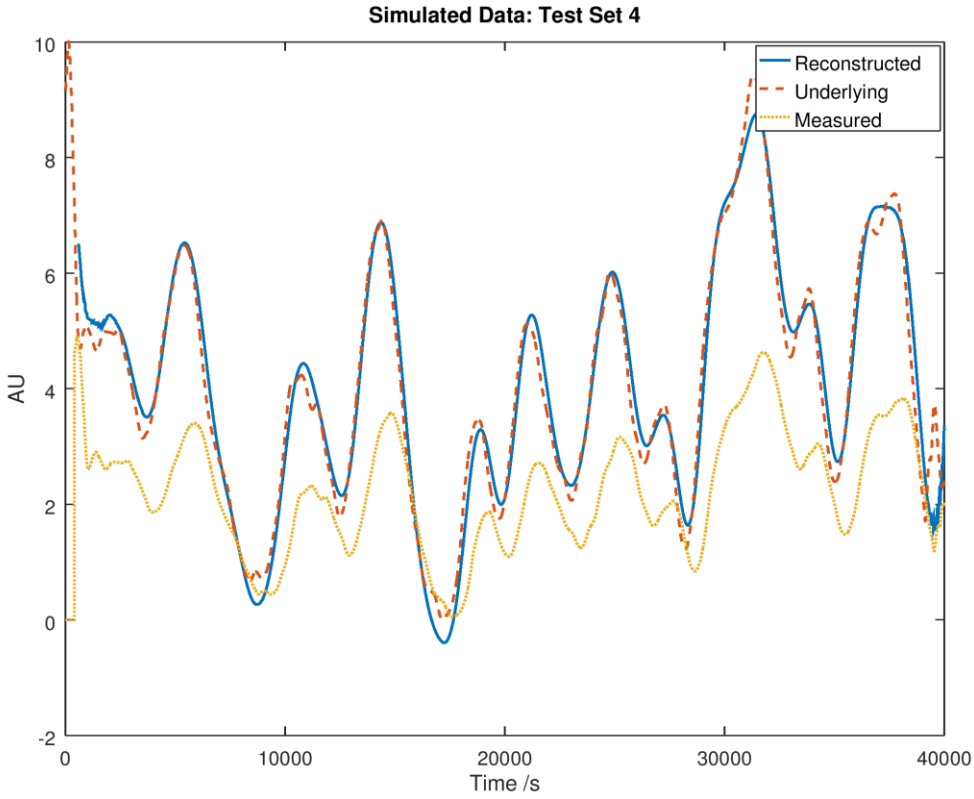
Simulated Data: Test Set 4
Reconstructed
Underlying
Measured
AU
Time /s
10
8
6
4
2
0
-2
0
10000
20000
30000
40000

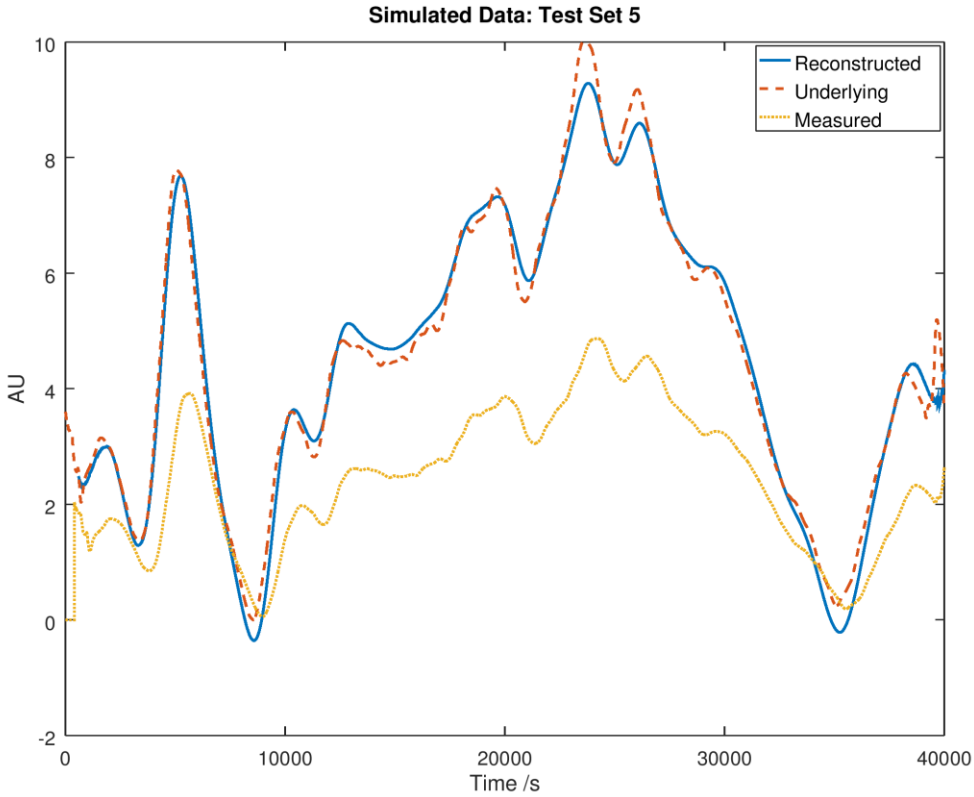
Simulated Data: Test Set 5
Reconstructed
Underlying
Measured
AU
Time /s
10
8
6
4
2
0
-2
0
10000
20000
30000
40000